FINAL TECHNICAL REPORT

AWARD NUMBER: G14AP00009

# Basin Amplification Factors for Cascadia from the 2011 Tohoku Earthquake

**Principal Investigator(s):**

Andreas Skarlatoudis, Mehrdad Hosseini, and Paul Somerville

URS Group, Inc.
915 Wilshire Boulevard
Los Angeles, CA 90017

October 7, 2015

Tel: 213.996.2200
Fax: 213.996.2290

Email: paul.somerville@aecom.com

"Research supported by the U.S. Geological Survey (USGS), Department of the Interior, under USGS award number G14AP00009. The views and conclusions contained in this document are those of the authors and should not be interpreted as necessarily representing the official policies, either expressed or implied, of the U.S. Government."

# Table of Contents

**Table of Contents** ..... **2**

**Abstract** ..... **3**

**Introduction** ..... **4**

**Selected Events** ..... **5**

**Seismic Stations** ..... **5**

**Japanese Basins** ..... **6**

**Seattle Basin** ..... **9**

**Soil Condition at Seismic Stations in Japan** ..... **10**

**Amplification in Japanese Basins** ..... **10**

Amplification Factors from Observations ..... 11

*Processing of the Observed Data* ..... *11*

*Response Spectra* ..... *13*

*Comparison to GMPEs and Residual Analysis* ..... *14*

*Distance Scaling* ..... *15*

*Estimation of Basin effects* ..... *25*

*Spatial distribution of basin amplification* ..... *36*

Amplification Factors from Long Period 3D simulations ..... 40

*Computational Method for 3D Simulations* ..... *40*

*Earth Structure Model* ..... *41*

*Depth to Shear-wave Velocity of 1.0 km/s ($z_{1.0}$)* ..... *42*

*Extended 1D Velocity Model* ..... *43*

*Accuracy of Simulations at High Frequency* ..... *44*

*Tohoku M9.0 Simulation* ..... *45*

*Tohoku Aftershock M7.4 Simulation* ..... *45*

*Amplification from 3D Simulations* ..... *46*

Application to the Seattle Basin ..... 59

**Conclusions** ..... **60**

**Data and Resources** ..... **64**

**Acknowledgments** ..... **65**

**References** ..... **65**

## Abstract

There is currently a boom in the design and construction of very tall buildings in Seattle and Bellevue. These buildings have fundamental natural periods as long as 7 seconds, and so their seismic responses are controlled by the response of the Seattle Basin to crustal, slab and subduction earthquakes. The design response spectrum in the ASCE 7-10 seismic provisions includes the parameter $T_L$, which defines the period at which the response spectrum changes from constant spectral velocity at intermediate periods to constant spectral displacement at the longer periods, as described by Crouse et al. (2006). The objective of the proposed work is to develop an improved representation of the long period spectrum for use in building codes.

No subduction earthquake recordings are available to validate ongoing USGS simulations of basin response to subduction earthquakes, as was possible for crustal and slab earthquakes. To fill this gap in knowledge, we performed a validation of simulation-based methods for estimating basin amplification effects using data and simulations of the largest events of the 2011 Tohoku earthquake sequence. The availability of recordings of multiple events allowed us to assess the event-to-event variability in basin response, and thereby estimate the median basin response and its variability. We used two approaches to develop basin amplification models using motions recorded during the largest events of the Tohoku earthquake sequence. The first approach was to measure basin amplification factors in recorded strong ground motions at basin sites with respect to published Next Generation Attenuation (NGA) ground motion prediction equations (GMPEs) for subduction events without considering potential basin effect terms in these models. The second approach was to measure basin amplification factors in simulated strong ground motions at basin sites using a 3D model with respect to simulations for a reference 1D non-basin model, following the approach that was used by Day et al. (2008) in the Los Angeles basin and applied in the GMPEs.

The amplification in the Seattle basin for two events: the Mw 6.8 Nisqually and Mw 6.4 Vancouver Island earthquakes, was studied by Frankel and Stephenson (2015). They found that the spectral amplification ratio in Seattle can be as high as 4, comparable to the results from the finite difference simulations for the Kanto and Niigata basins performed in this study. In addition, Frankel and Stephenson (2015) performed 3D finite difference simulations and calculated spectral response at basin, non-basin and rock sites for Mw 9 megathrust earthquakes on the Cascadia subduction zone.

We used the response spectra from the Frankel and Stephenson (2015) simulations to estimate their amplification factors. The amplifications that we obtained from observations and 3D simulations in the Kanto and Niigata basins follow the trend of the lower bound amplification for station QAW located in the Seattle basin as estimated by Frankel and Stephenson (2015). The fairly good agreement between our measured and simulation-based amplifications in the Kanto and Niigata basins demonstrates the viability of Frankel and Stephenson's (2015) use of simulation methods to estimate amplification in the Seattle Basin from large subduction

earthquakes in the absence of recorded data. The measured and simulated amplifications in the Kanto and Niigata basins for periods up to 5 seconds are similar to the lower bound amplification for station QAW located in the Seattle basin as estimated by Frankel and Stephenson (2015), but are smaller at longer periods.

## Introduction

Seismic waves are trapped and amplified in deep sedimentary basins and can increase the damage induced by a smaller fault. The presence of basins in earthquake prone areas such as the Seattle region requires an understanding of basin amplification effects on structures. The response of tall buildings, which have fundamental natural periods as long as 7 s econds, is controlled by the response of the Seattle Basin to crustal, slab and subduction earthquakes. For this reason, extensive empirical and modeling studies of the response at the Seattle basin have been conducted. Frankel and Stephenson (2000) and Frankel et al. (2002, 2009) measured basin response during several crustal and slab earthquakes including the 2001 Mw 6.8 Nisqually earthquake, and simulated the basin response for several of these earthquakes, including the Nisqually earthquake and scenario crustal earthquakes on the Seattle fault. Recently, Frankel (personal communications) simulated the Seattle basin response to large interface Cascadia subduction earthquakes. However, in the absence of subduction earthquake recordings, it is not possible to validate those simulations.

In this study, we perform a validation of simulation-based methods for estimating basin amplification effects using data and simulations of the largest events of the 2011 Tohoku earthquake sequence. We use two approaches to develop basin amplification models. The first approach is to use recorded strong ground motions at basin sites and calculate their residuals with respect to published GMPEs for subduction events without considering the basin effect terms of these model. The second approach is to measure basin amplification factors in simulated strong ground motions at basin sites using a 3D model with respect to simulations for a reference 1D no-basin model, following the approach that was used by Day et al. (2008) in the Los Angeles basin and applied in the NGA GMPEs. Finally, we study the possibility of applying the findings of this research to the Seattle basin considering the similarity with the basins in Japan.

## Selected Events

Three events are considered for this study including the Tohoku M9.0 mainshock and the two largest aftershocks. Table 1 provides a summary of the selected events.

**Table 1**. List of events used in this study.

| ID | Japan local time | Lon | Lat | Depth (km) | Mw | Strike° | Dip° | Rake° | Velocity Model† |
|---|---|---|---|---|---|---|---|---|---|
| **1** | 2011/03/11,05:46 | 142.86 | 38.10 | 24 | 9 | 200 | 27 | 88 | 1 |
| **2** | 2011/03/11,06:09 | 142.78 | 39.84 | 32 | 7.4 | 179 | 23 | 60 | 3 |
| **3** | 2011/03/11,06:15 | 141.26 | 36.11 | 43 | 7.7 | 209 | 31 | 92 | 2 |

†Depending on the location of the fault, velocity models in this column are extracted from Koketsu et al. (2008) Japan Integrated Velocity Structure Model (JIVSM) covering slightly different geographical areas to efficiently synthesize ground motions. Figure 19 shows the coverage area of each velocity model.

## Seismic Stations

Recorded data from more than 1600 stations were collected and those falling in the vicinity of five major basins in Japan, described in the next section, were processed. The data were downloaded from the National Research Institute for Earth Science and Disaster Prevention (NEID) Strong-motion Seismograph Network (K-NET and KiK-net). Figure 1 shows the location of seismic stations and events used in this study.

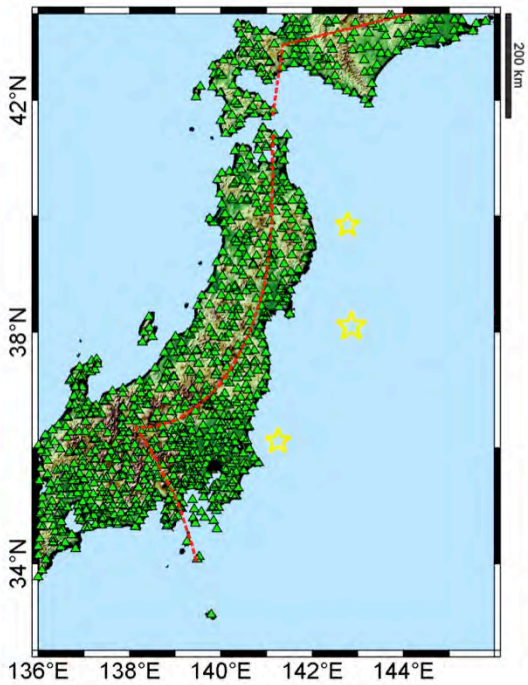


**Figure 1.** Geographical locations of K-NET and KiK-net seismic stations and events listed in Table 1. The volcanic front is shown as a dashed red line.

## Japanese Basins

We initially studied the structure of five basins in Japan including the Kanto, Niigata, Ashigara, Osaka, and Sendai basins. Figure 2 shows the geographical locations of these basins. The goal is to find amplification factors for each of these five basins and use those that are most similar to the Seattle basin to provide guidance on the magnitude of amplification.

**Figure 2.** Five basins in Japan initially considered in this study.

Basin boundaries are identified using the 1.0, 1.5, and 2.5 km/s shear-wave velocity iso-surfaces. We used the Koketsu et al. (2008) velocity model to define the iso-surfaces of the different basins. We excluded the Ashigara, Osaka, and Sendai Basins due to their small size, and, for the Ashigara and Osaka basins, their remoteness from the plate boundaries (Figure 3). The focus of this study is therefore on the Kanto and Niigata basins as shown in Figure 2.

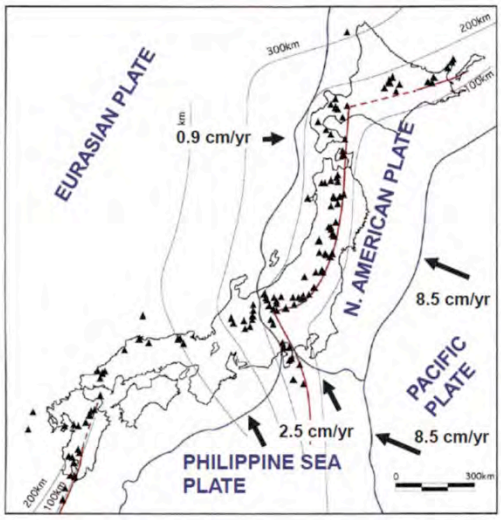


**Figure 3.** A map of Japan showing tectonic plates. (from James et al. 2013)

Figures 4 through 6 show these iso-surfaces for the Kanto and Niigata basins for 1.0, 1.5, and 2.5 km/s S-wave velocity. We refer to these iso-surfaces as $z_{1.0}$, $z_{1.5}$, and $z_{2.5}$. We used a combination of three iso-surface maps to define the boundaries of each basin as shown in Figure 7. Using the basins boundaries we divided k-NET and KiK-net stations into two groups: inside and outside each basin. We used a tolerance of 5 km to define stations 'on the boundaries'. Figure 7 presents the stations inside the boundaries of these basins. As shown by Cox et al. (2013) there are 22 strong motion sites for which there is evidence of soil liquefaction. These sites are mostly located at the southern end of the fault rupture plane in the Tokyo Bay and Kanto Plain regions (Figure 7, red triangles). We excluded the recordings of these strong motion sites from any further analysis .

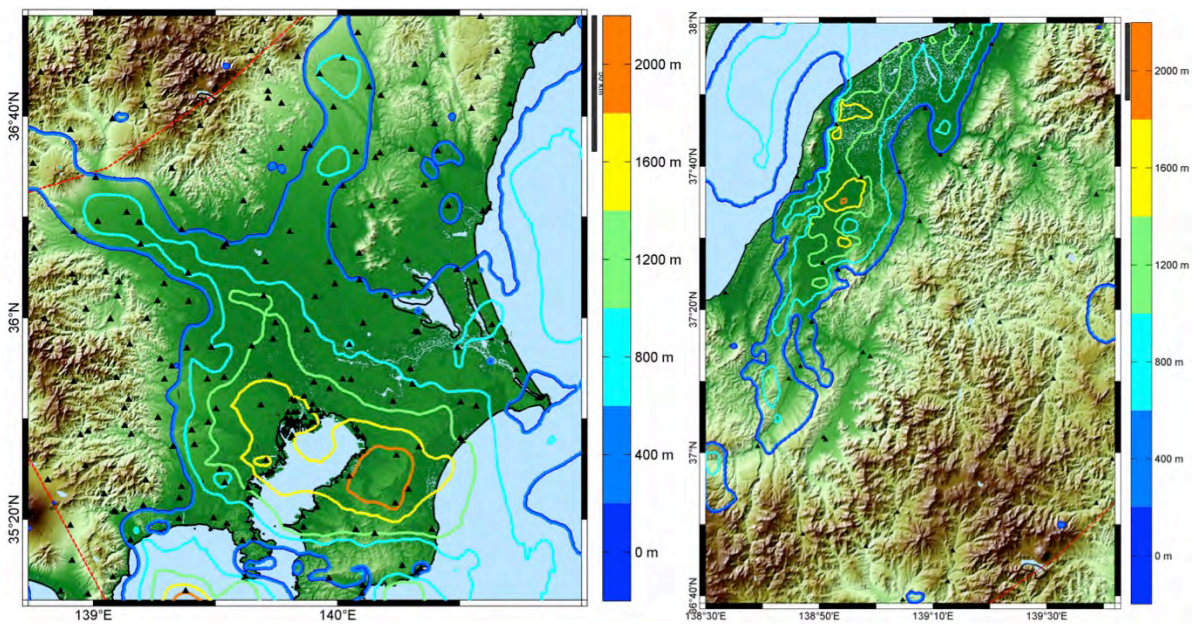


**Figure 4.** Isosurface maps to 1.0 km/s S-wave velocity for Kanto (right) and Niigata (right) basins.

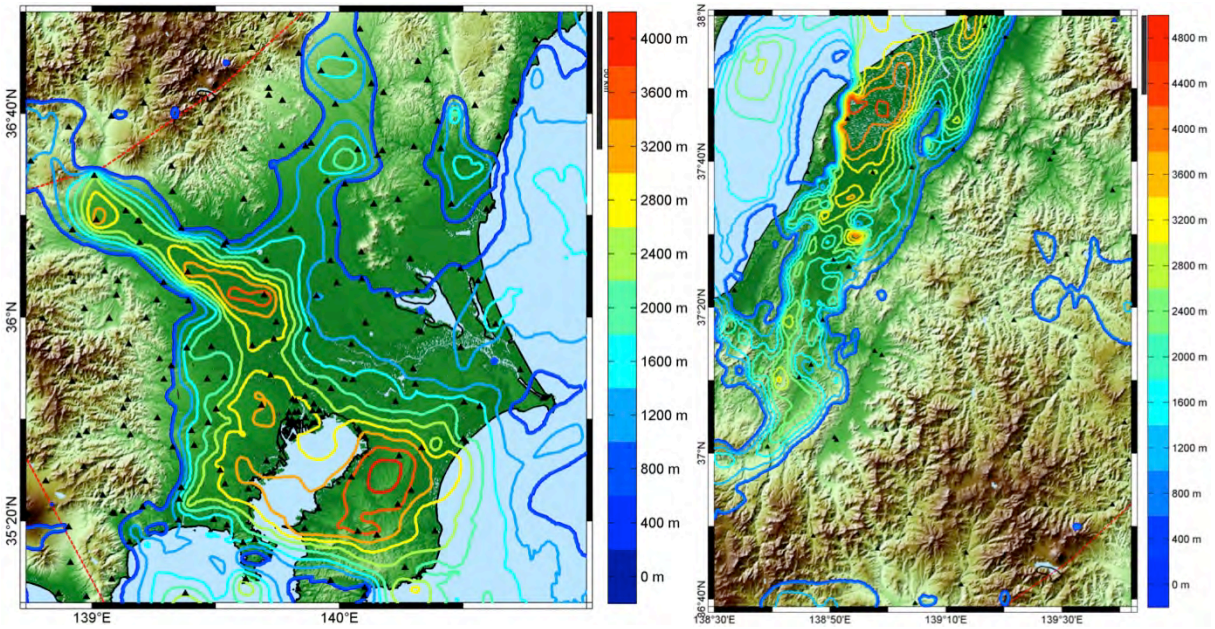


**Figure 5.** Isosurface maps to 1.5 km/s S-wave velocity for Kanto (right) and Niigata (right) basins.

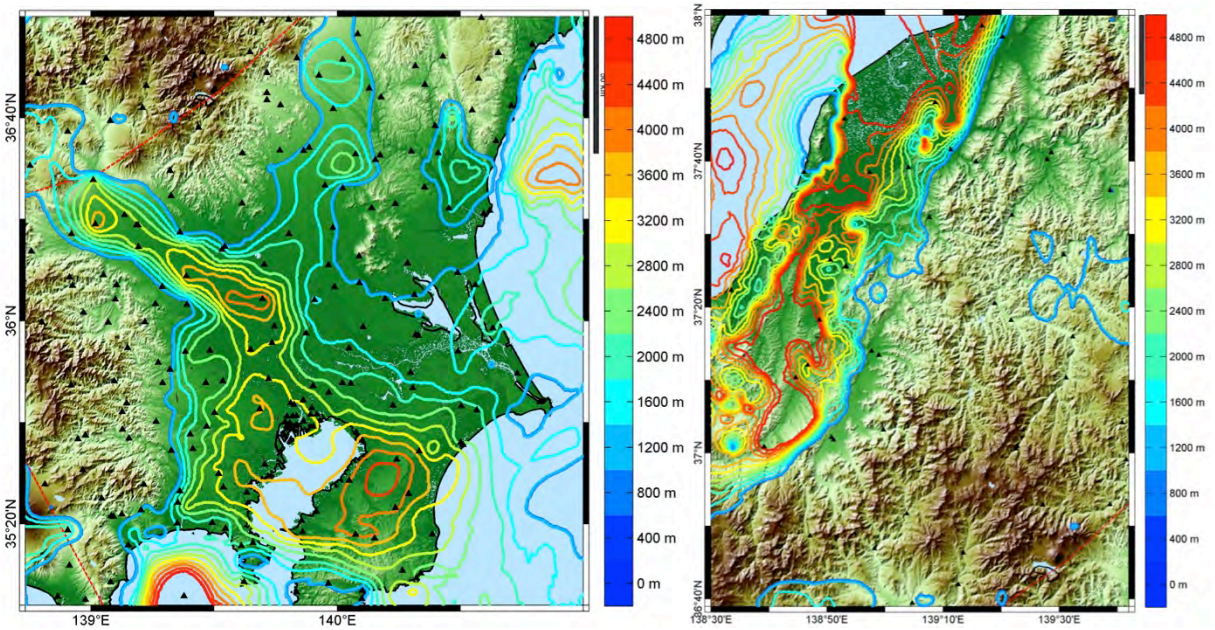


**Figure 6.** Isosurface maps to 2.5 km/s S-wave velocity for Kanto (right) and Niigata (right) basins.

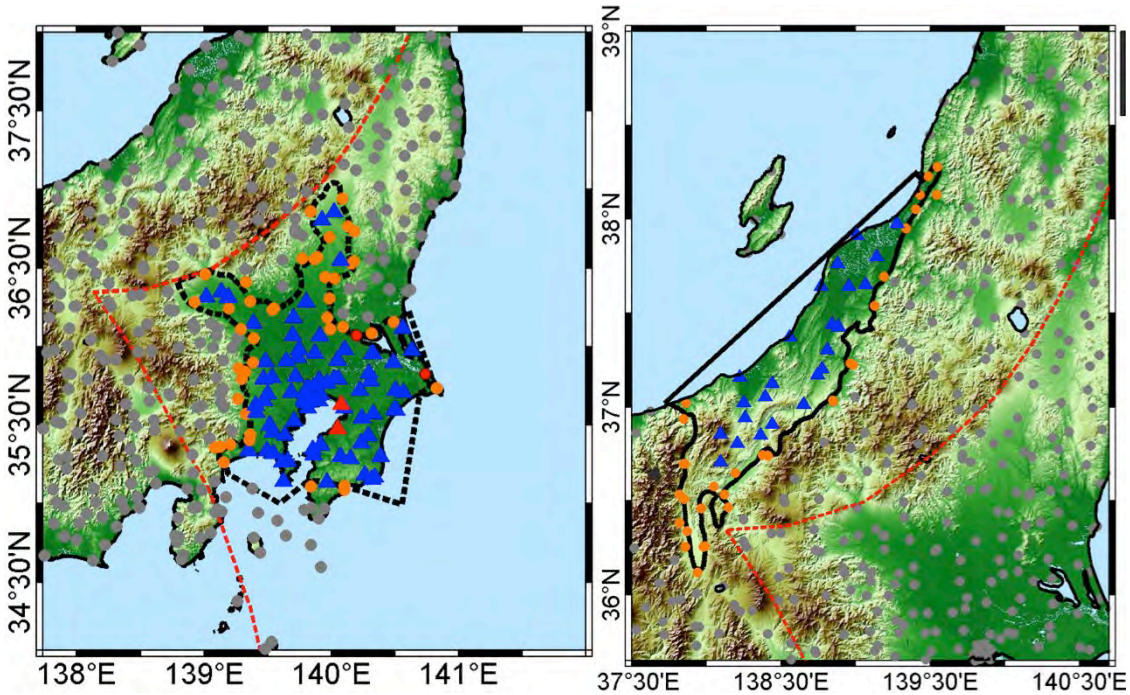


**Figure 7.** Boundary of Kanto (left) and Niigata (right) basins is determined from $z_{1.0}$, $z_{1.5}$, and $z_{2.5}$ iso-surfaces. Stations inside the basin are shown with triangles and those on the boundary of the basins are shown with circles. Recordings from the stations denoted with the red triangles are excluded from the analysis because of evidence for soil liquefaction at these recording sites (Cox et al. 2013).

## Seattle Basin

The Seattle basin is defined using the map for 2.5 km/s shear wave velocity as presented in Figure 8. We used the iso-surface of about 2.2 km to define the boundary of this basin.

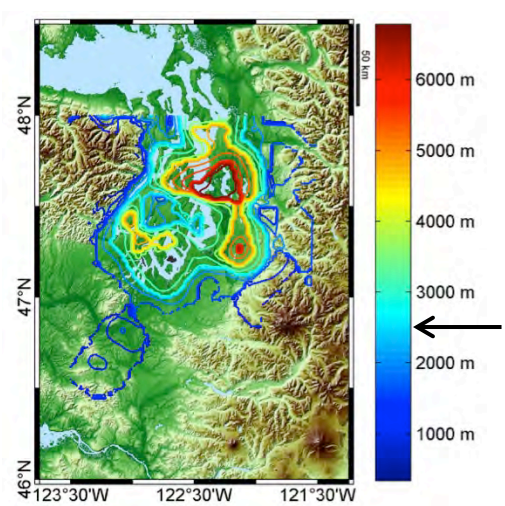


**Figure 8.** $z_{2.5}$ Iso-surface maps for Seattle basin. The arrow shows the depth (2200 m) at which the extent of the Seattle basin is defined.

## Soil Condition at Seismic Stations in Japan

Soil conditions at K-NET and KiK-net stations are evaluated using borehole tests and are reported separately for each station. We used these reports to estimate the upper 30 meter shear wave velocity ($V_{S30}$). $V_{S30}$ values are plotted in Figure 9.

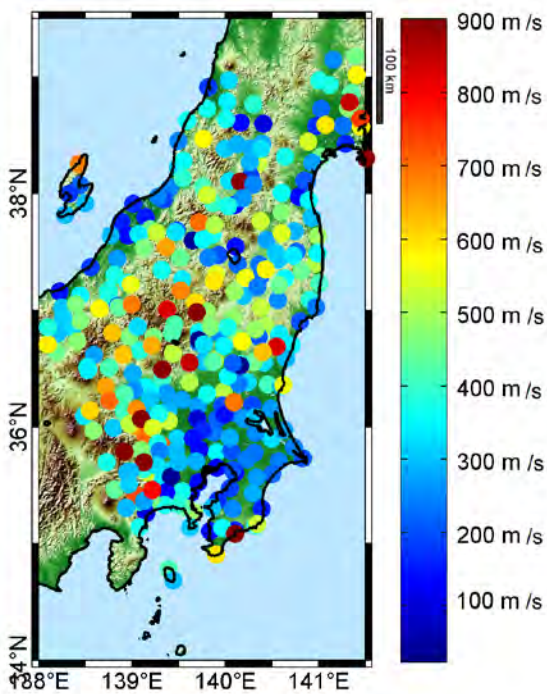


**Figure 9.** $V_{S30}$ values acquired from field tests, color coded to a maximum of 900 m/s. Values are calculated from velocity profiles reported at the locations of KiK-net and K-NET stations by NEID.

## Amplification in Japanese Basins

Two methods are used to estimate the amplification in Japanese basins. The first method investigates the deviation of observed ground motions from GMPEs for subduction earthquakes without considering potential basin terms in the models. This can be used to reveal the extent to which current GMPEs are applicable to basin sites, and to estimate corrections of GMPEs for basin effect (Boore et al. 2014). The second method uses a completely theoretical technique using 3D simulations where time series synthesized in a r ealistic 3D model of Japan are compared with those from a flat layered model that does not include basin effects. The following paragraphs give more details regarding each method used to quantify the amplification.

1. Amplification Factors from Observations

In order to provide a reference for the measurement of basin amplification for the 2011 Tohoku mainshock and largest aftershocks at basin sites, we used published GMPEs that do not include basin amplification terms. Several investigators have developed ground motion prediction equations that embody the 2011 Tohoku earthquake. These include Abrahamson et al. (2012), who developed event terms for the Tohoku earthquake with respect to their GMPE model based on pre-Tohoku data, and adjusted their model for those event terms; Ghofrani and Atkinson (2013) who developed a model for the 2011 Tohoku earthquake; and Si (2012) who modified his GMPE to include the Tohoku earthquake.

2. Amplification Factors from Long Period 3D Simulations

Amplification effects in a basin are three-dimensional and are therefore difficult to quantify empirically from observations. Here we address basin amplification for periods longer than 1 second and deep basins exceeding 3km or more (Day et al. 2008; Campbell and Bozorgnia, 2008). We followed the method used by Day et al. (2008) who developed basin amplification factors using large suites of long period ground motion simulations for sets of earthquake sources. The amplification factors depend on the depth of the basin, as expressed by the depth of 1.0 km/sec shear-wave iso-velocity surfaces, and they are a function of period.

We used kinematic rupture models of the Tohoku mainshock and largest aftershock to simulate the source rupture models of these events and simulated the ground motions using representative 3D velocity models. To model the amplification from 3D simulations, simulations from realistic 3D velocity models are compared against a 3D velocity model that does not contain basin structures. The latter 3D velocity models are derived from 1D velocity models, representing rock (non-basin) sites. Details of these models are presented in upcoming sections.

The following sections describe the details of each of the techniques presented above for amplification estimation.

## Amplification Factors from Observations

### Processing of the Observed Data

Processing of observations is an important step since amplification is measured by comparing the observations against GMPE predictions. Processing includes visual inspection of every recording from all the events to remove inappropriate data and to select a corner frequency with which to high pass filter the data. During the processing procedure we high-pass filtered each component of the recordings using ten different corner frequencies and visually inspected each one of them to find the best matching corner frequency; truncated the time series if required; and removed noisy and bad recordings.

An example of uncorrected and filtered time series from a station that recorded the **M** 7.7 3-11-2011 aftershock is provided in Figure 10. An example of data excluded during processing is shown in Figure 11. More details are provided further below.

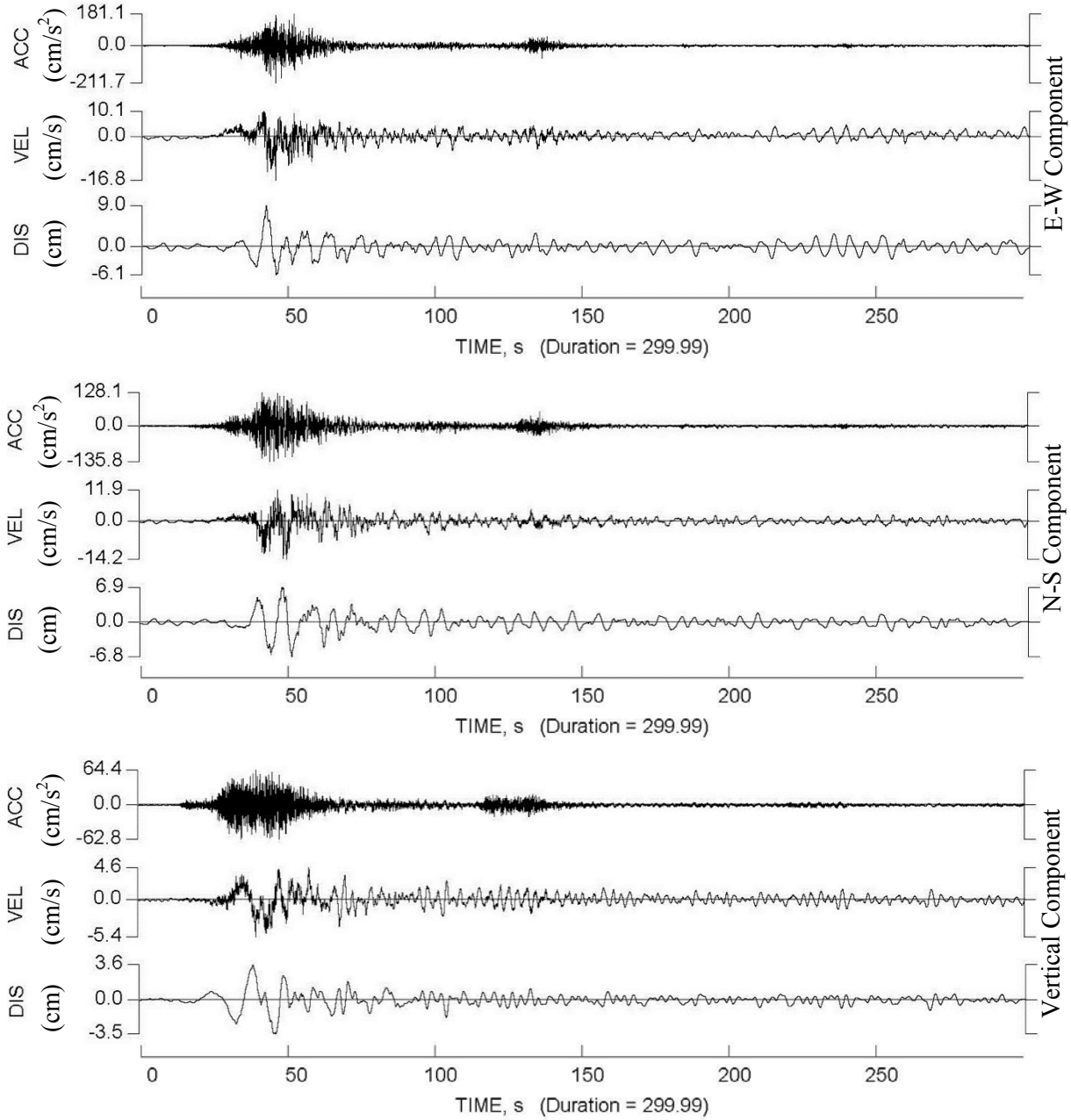


**Figure 10.** Acceleration, velocity and filtered displacement of M 7.7 3-11-2011 event recorded at station CHB001. Displacements are associated with a high-pass filtered accelerogram with corner frequency of 0.06 Hz. East-west, north-south, and vertical components are shown from top to bottom, respectively. Time series for this station are cut in [0 110] s window and bandpass filtered in [0.06 30] Hz frequency range.

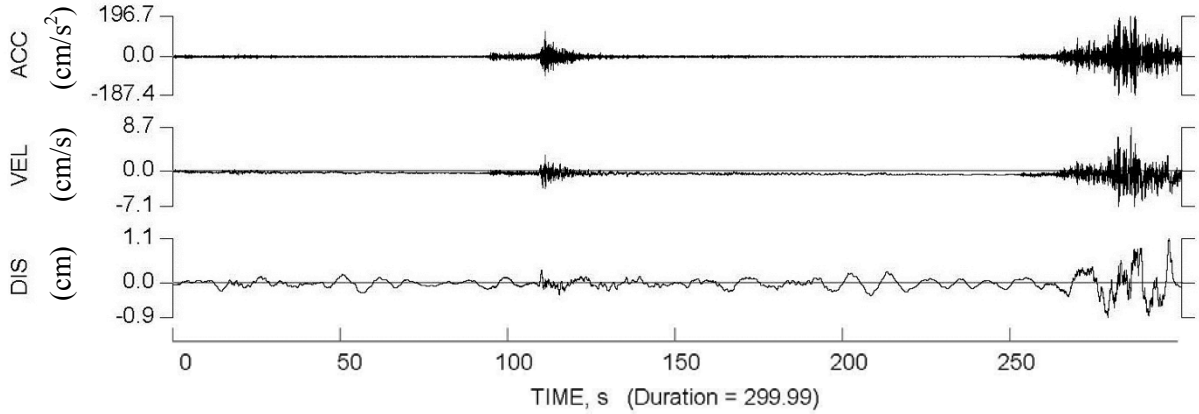


**Figure 11.** Acceleration, velocity, and displacement from FKSH10 station that has recorded a pre-event prior to the main event. This recording was excluded during the processing.

**Response Spectra**

The RotD50 (Boore 2010) values computed for the NGA West 2 period set (111 spectral periods) and 5% damping are used as the intensity measure (IM) in this report. The maximum usable period for which the IM are used in the analysis is a function of the corner frequency used in the high-pass filtering process. Figure 12 presents the spectral responses at 0.1 and 1.0 second spectral period for three events listed in Table 1.

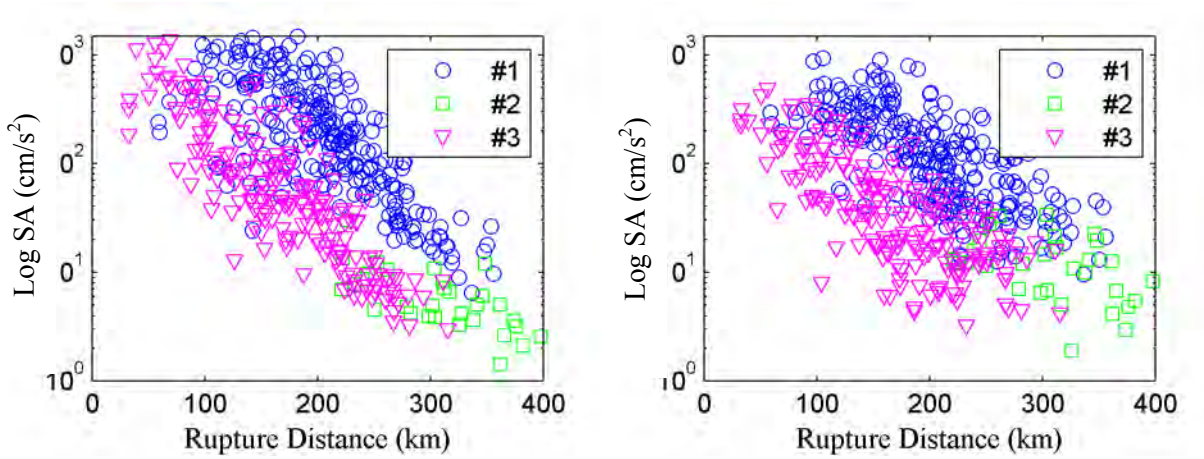


**Figure 12.** Spectral response at 0.1 (left) and 1.0 (right) second from observations of the three events in Table 1.

**Comparison to GMPEs and Residual Analysis**

We evaluated residuals between the data and a set of ground motion prediction equation (GMPE) models to calculate empirical basin amplification factors. Residuals are calculated as:

$$R_{ij} = ln(\mathrm{IM}_{ij})_{\mathrm{data}} - ln(\mathrm{IM}_{ij}) \tag{1}$$

Index $i$ refers to the earthquake event and index $j$ refers to the recording within event $i$. Hence, $R_{ij}$ is the residual of data from recording $j$ in event $i$ as calculated using a particular GMPE. The term $ln(\mathrm{IM}_{ij})_{\mathrm{data}}$ represents the RotD50 parameter (Boore, 2010) computed from recording $j$. Term $ln(\mathrm{IM}_{ij})$ represents the median calculated using the particular GMPE in natural log units.

Residuals are calculated using equation (1) for two GMPEs for intermediate depth earthquakes: Abrahamson et al (2012) and Zhao et al., (2006). These GMPEs do not implicitly include a basin amplification term and they parameterize site effects using the $V_{S30}$ parameter. The analysis of residuals with respect to different predictor variables requires that event-to-event variations be separated from variations of residuals within events. This is accomplished by performing a mixed effects regression (e.g. Abrahamson and Youngs, 1992) of residuals according to the following function:

$$R_{ij} = c_k + \eta_i + \varepsilon_{ij} \tag{2}$$

where $c_k$ represents a mean offset (or bias) of the data relative to the particular GMPE, $\eta_i$ represents the event term for event $i$, and $\varepsilon_{ij}$ represents the intra-event residual for recording $j$ in event $i$. Event term $\eta_i$ represents approximately the mean offset of the data for event $i$ from the predictions provided by the GMPE median (after adjusting for mean offset $c_k$, which is based on all events). Event and intra-event terms are assumed to be normally distributed with zero mean and have standard deviation, ($\tau$), and ($\varphi$) in natural log units.

The basic scope of this analysis is to quantify the basin amplification effects with respect to the specific ground motion models. Magnitude, distance and site effects are typically the predictor variables against which residuals are studied for a particular GMPE in this type of analysis. Due to the limited number of earthquakes in the dataset, a statistical analysis of the magnitude scaling was not possible. The basin amplification is strongly correlated with $V_{S30}$ so we did not perform any adjustment to the site effect coefficients of the selected GMPEs either. We performed adjustments to the selected GMPE models for the distance scaling for the two data categories (basin and non-basin). If necessary, we performed adjustments to the non-basin data for any trends they might exhibit with respect to the basin amplification predictor we selected in this study.

**Distance Scaling**

Distance scaling is tested by examining trends of intra-event residuals, $\varepsilon_{ij}$, as a function of rupture distance. The standard deviation of the intra-event and inter-event residuals as well as total standard deviation ($\sigma$) are shown in Tables 2 and 3 for each GMPE for the various IMs studied. In Figures 13 and 14, $\varepsilon_{ij}$ for the various IMs for Abrahamson et al. (2012) and Zhao et al. (2006) GMPEs are shown, respectively, for a suite of ground motion periods ranging from 0 to 10 seconds.

To help illustrate trends, we also plot a fit line and its 95% confidence intervals. We consider that the observed distance trends are attributable to the anelastic attenuation terms of the GMPEs so we chose for the fit the following functional form:

$$\varepsilon_{ij} = a_R - b_R R_{ij} \tag{3}$$

with $a_R$ and $b_R$ being regression parameters. The fit was performed to the data with $R_{rup} \geq 60$km, where the bulk of the data set lies. Slope parameter $b_R$ represents approximately the misfit of the distance scaling in the dataset relative to the selected GMPE's. Also shown in Figures 13 and 14 are median residuals (black circles) within overlapping distance bins.

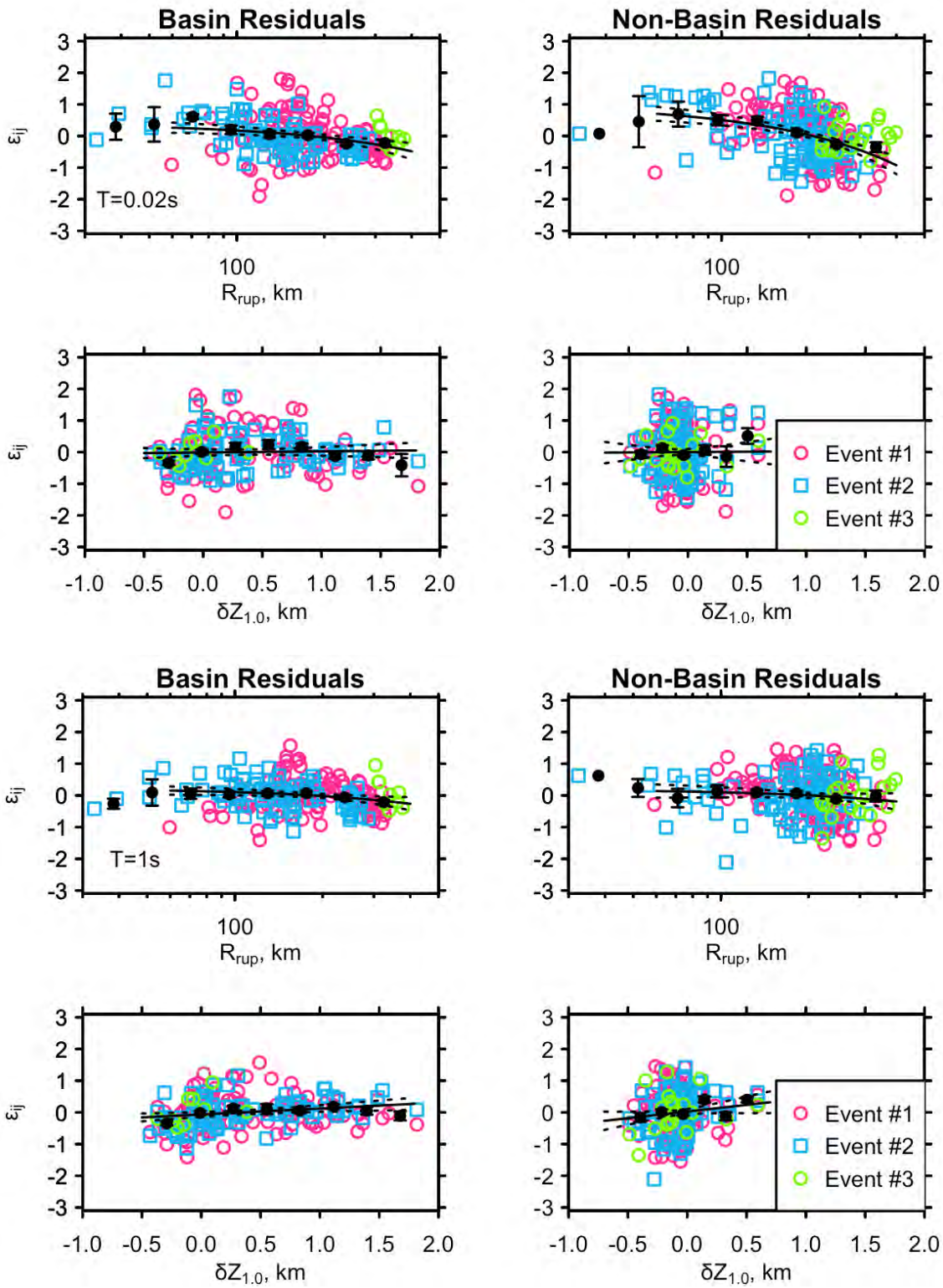


**Figure 13.** Variation of intra-event residuals with distance for various IMs for the Abrahamson et al. (2012) GMPE. The red circles correspond to residuals from Event #1, the green circles from Event #2 and the blue squares from Event #3 of Table 1.

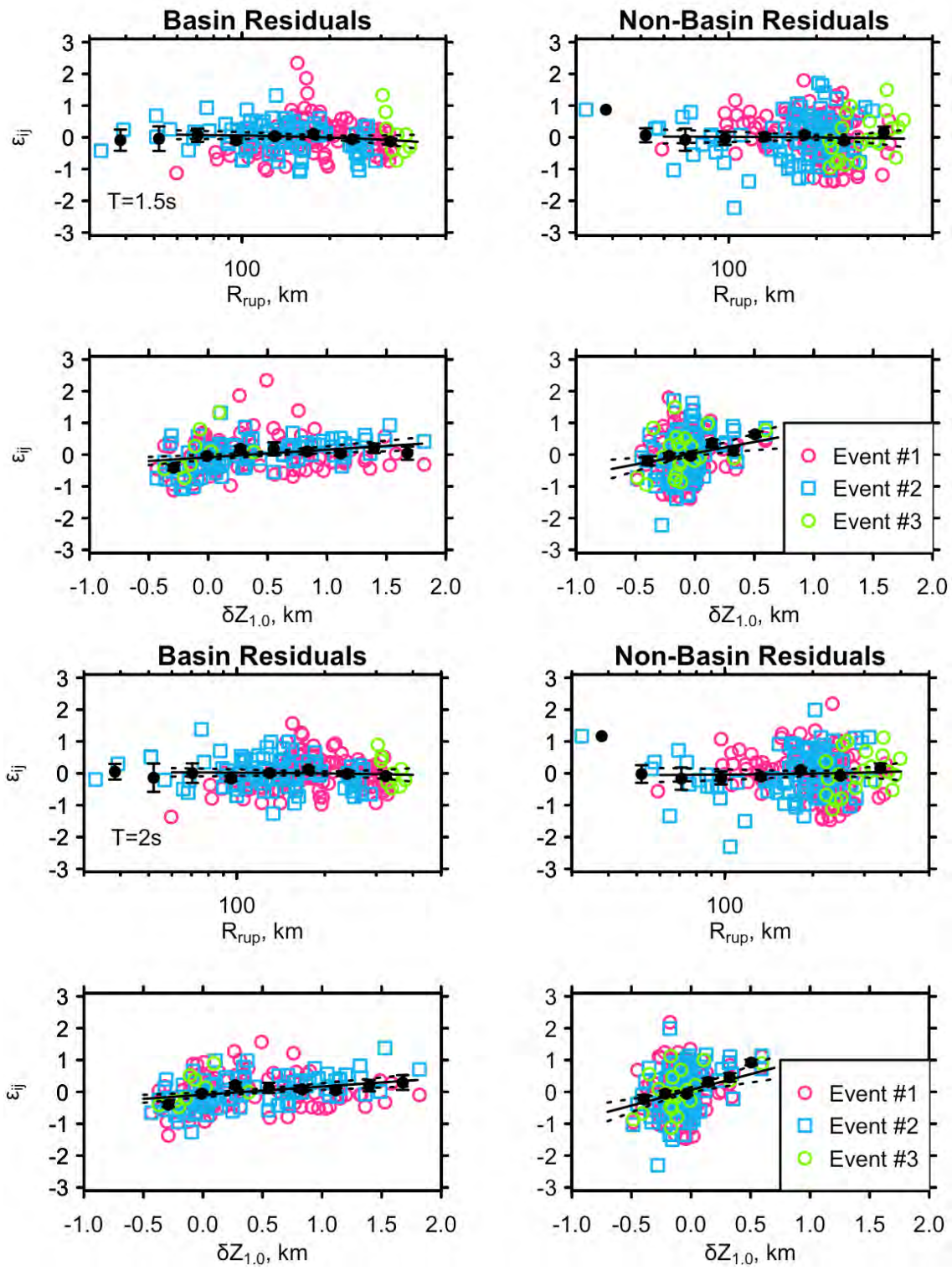


**Figure 13**. Continued.

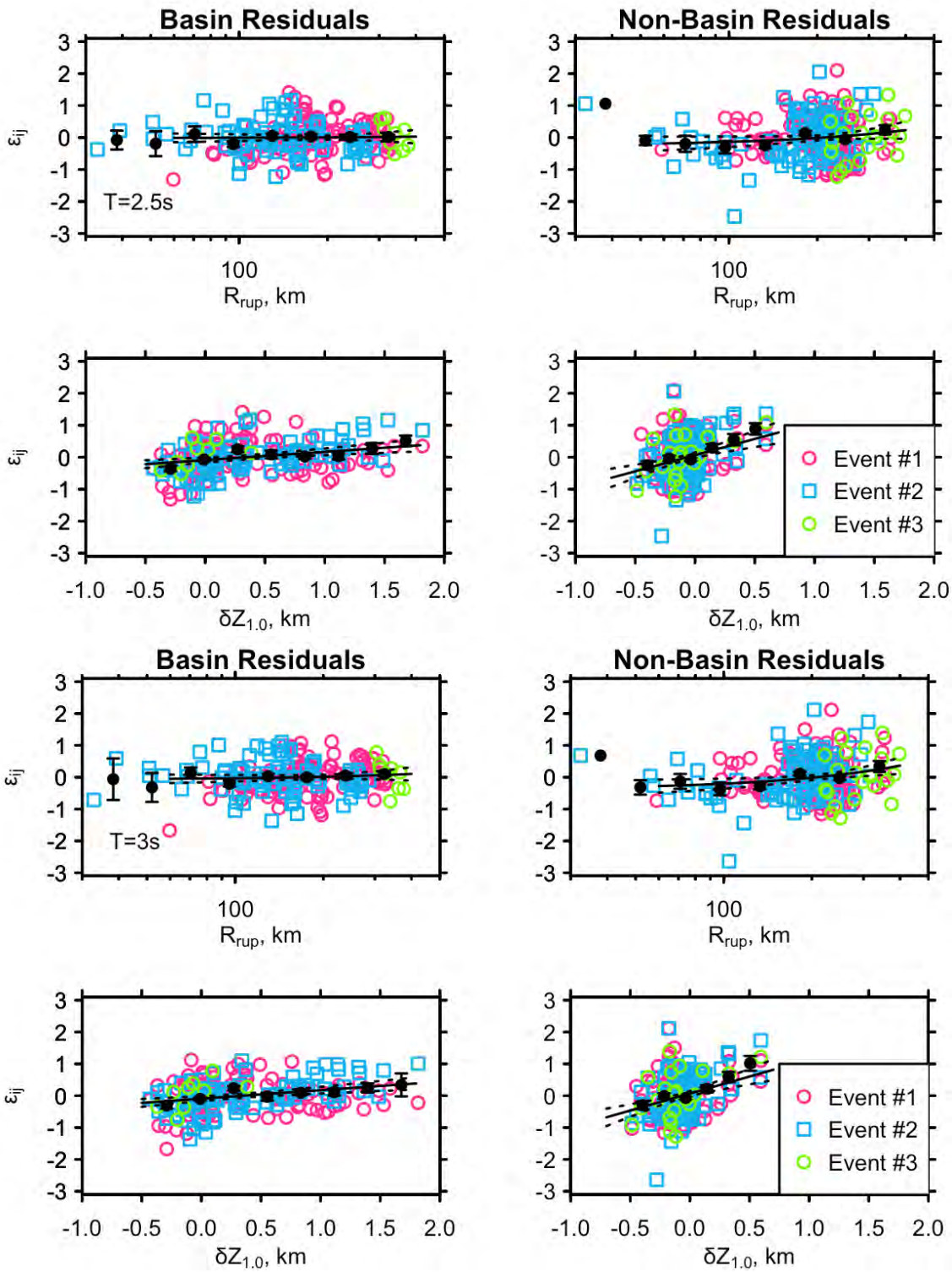


**Figure 13**. Continued.

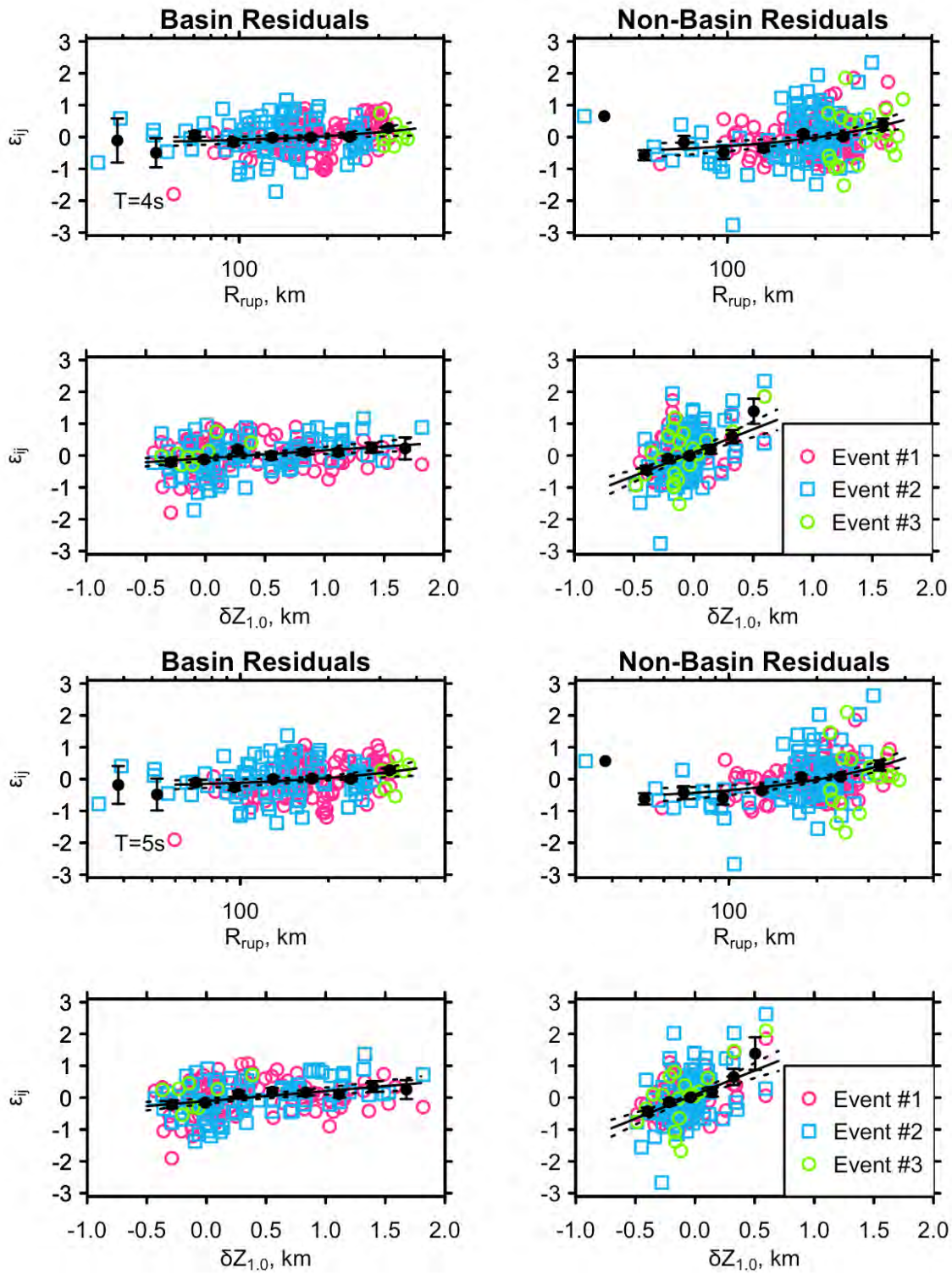


**Figure 13**. Continued.

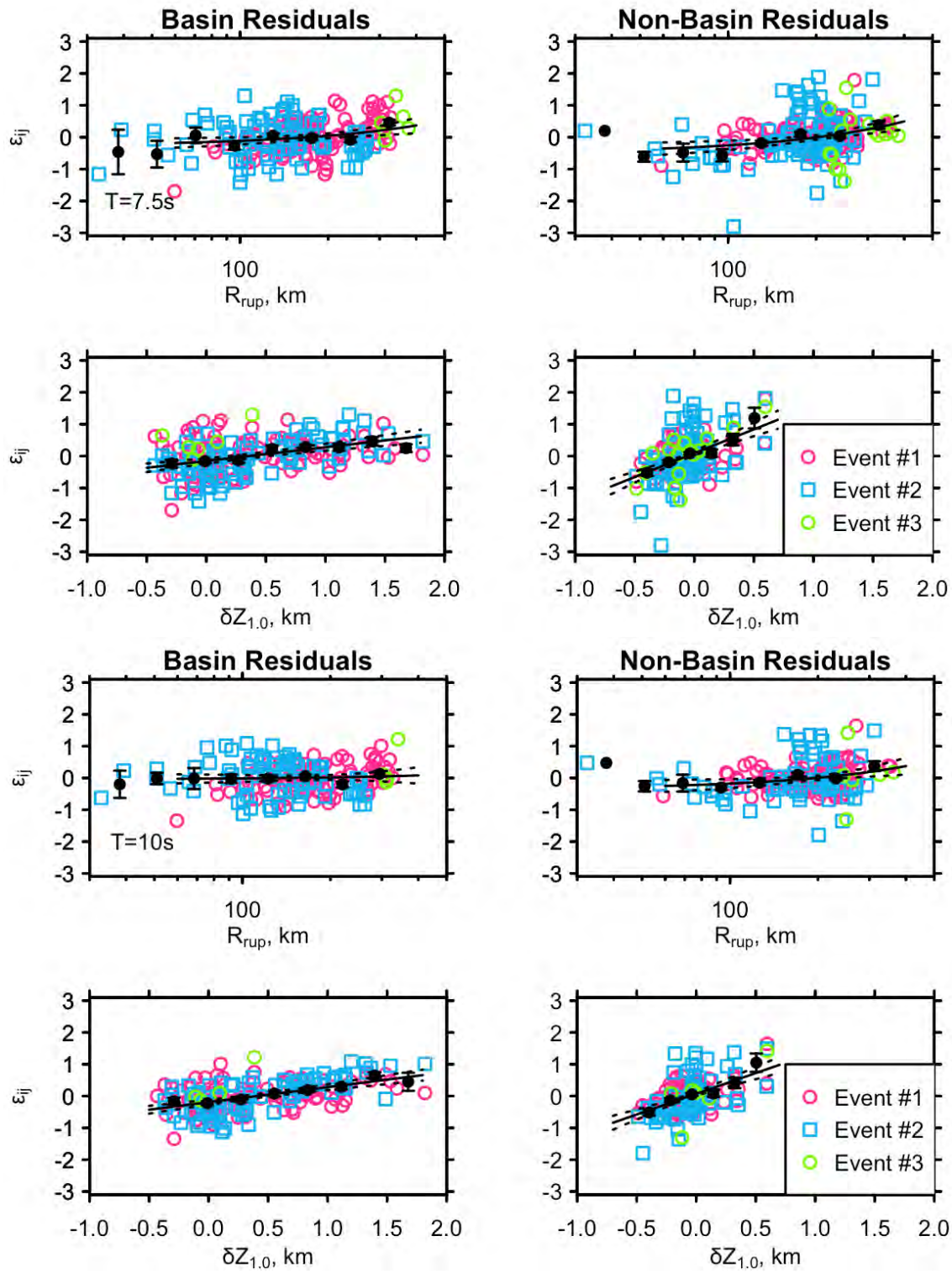


**Figure 13**. Continued.

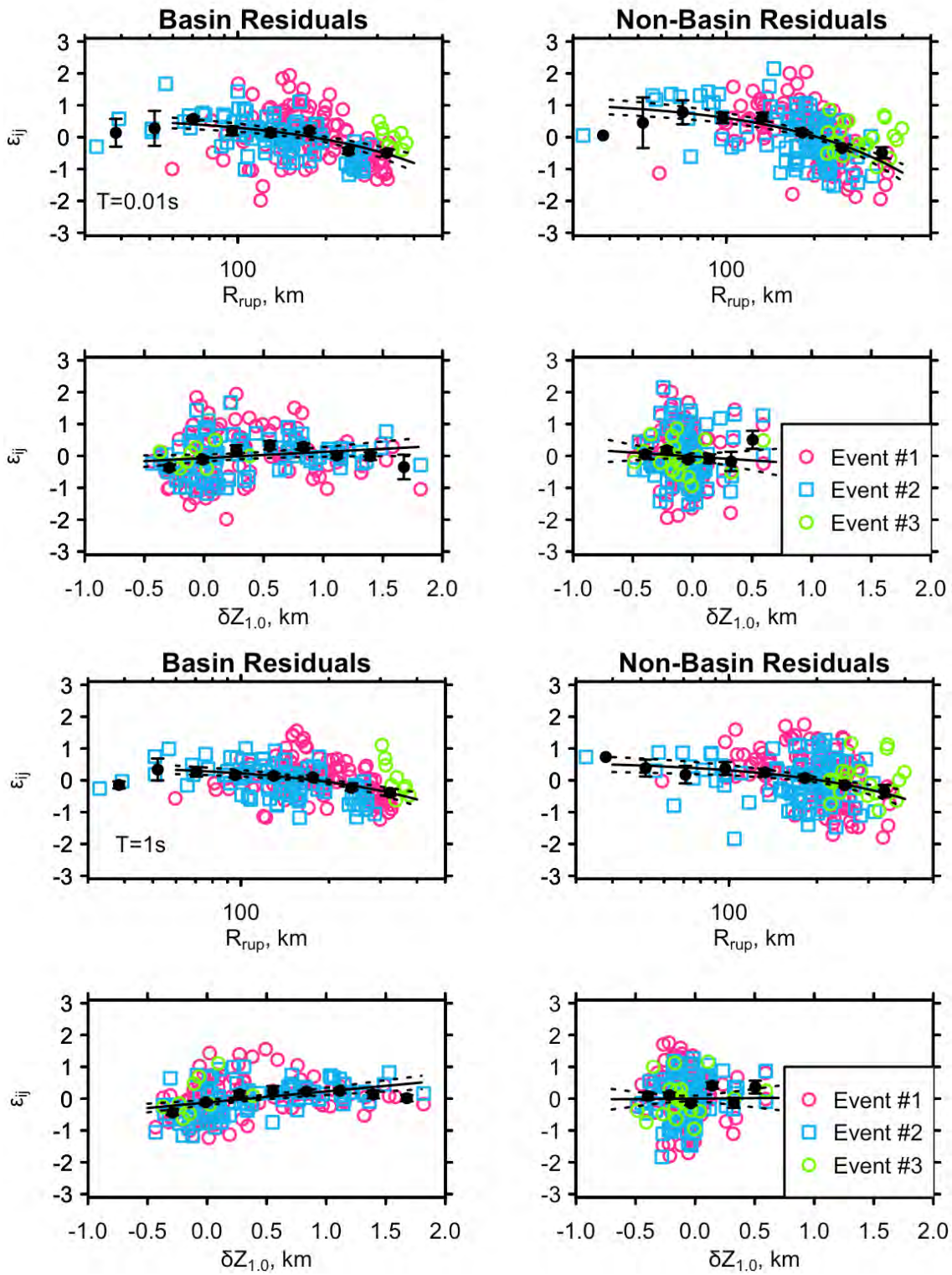


**Figure 14.** Variation of intraevent residuals with distance for various IMs for Zhao et al. (2006) GMPE. Colors and symbols are the same as in Figure 13.

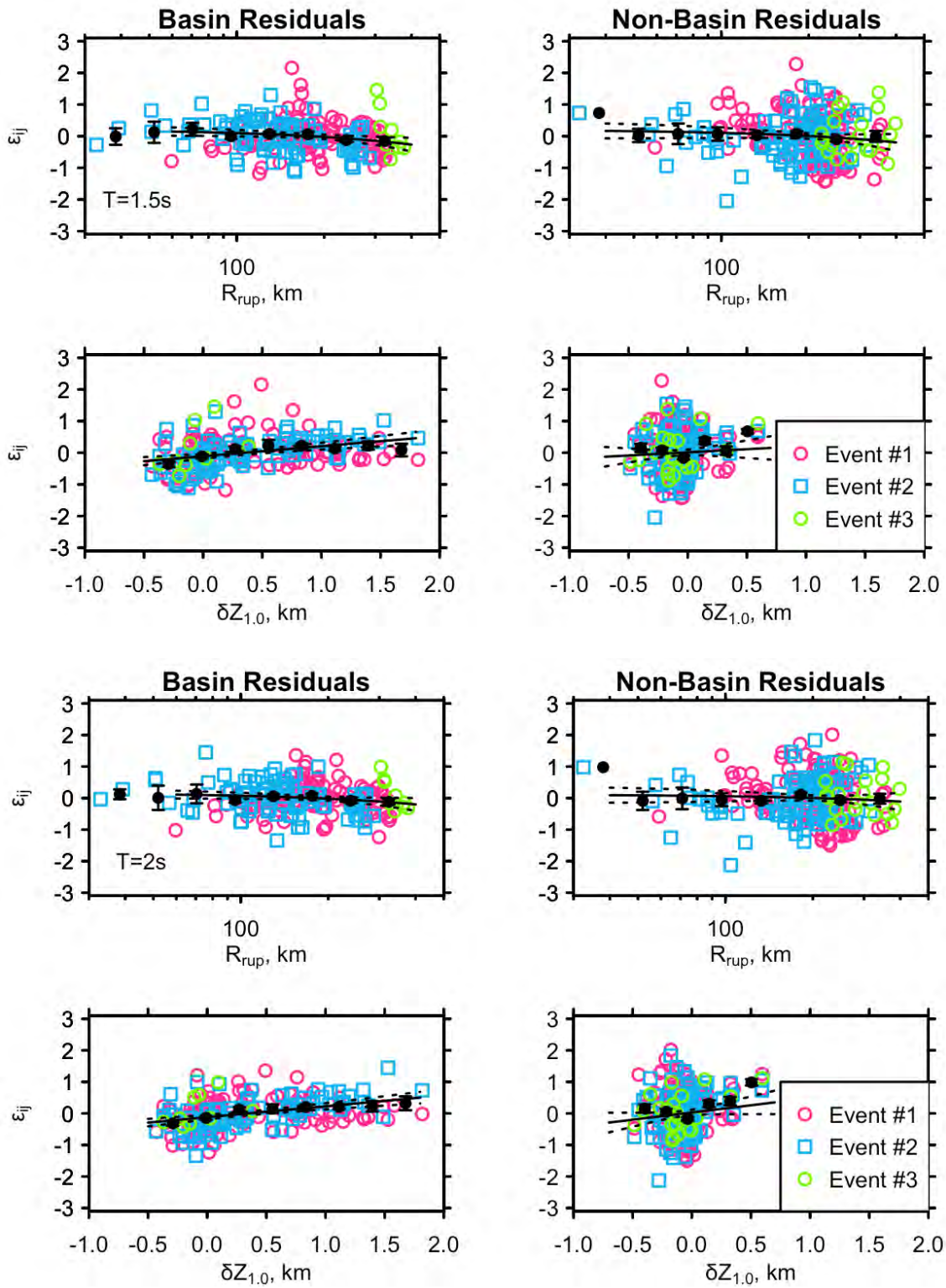


**Figure 14**. Continued.

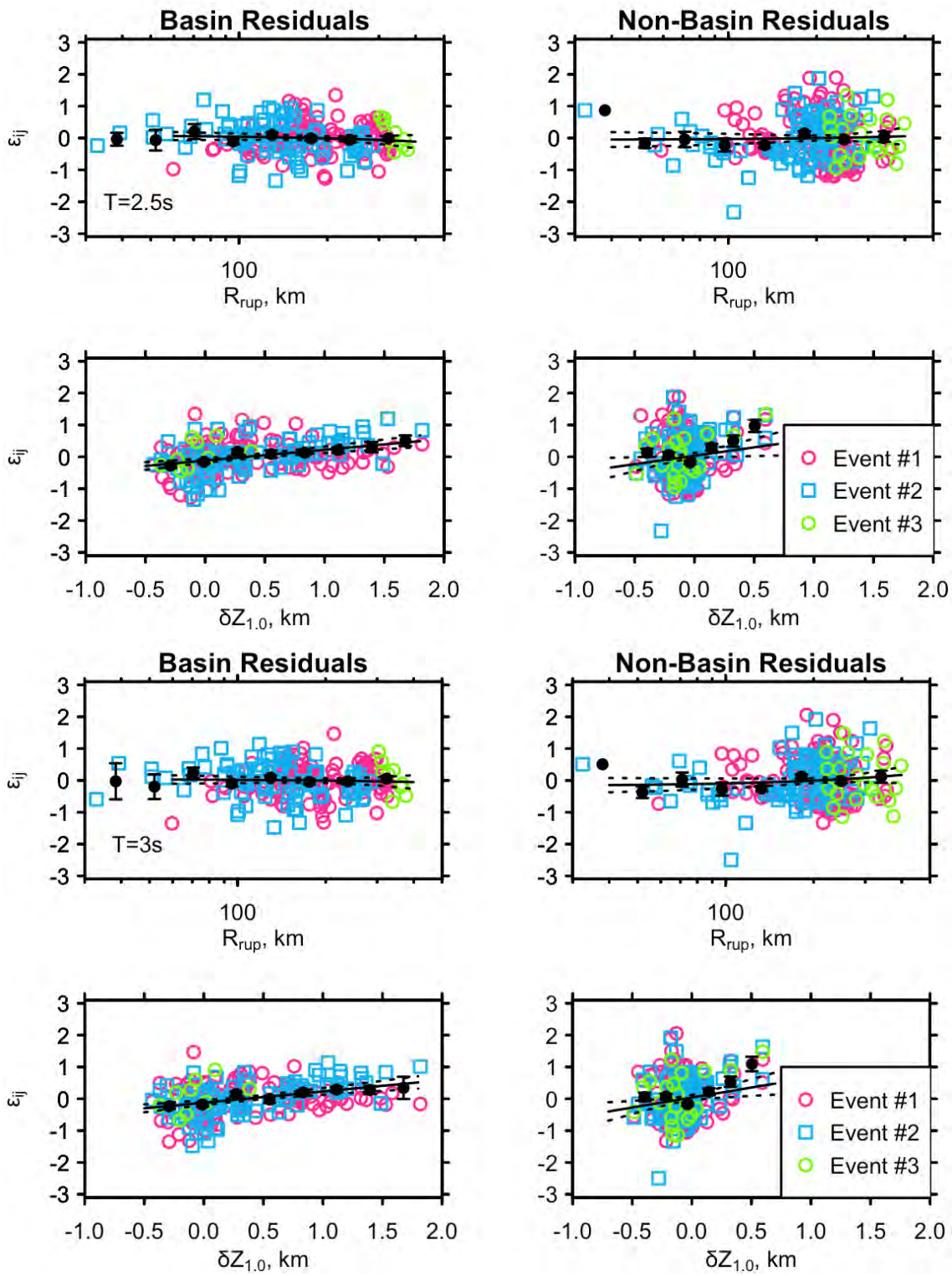


**Figure 14**. Continued.

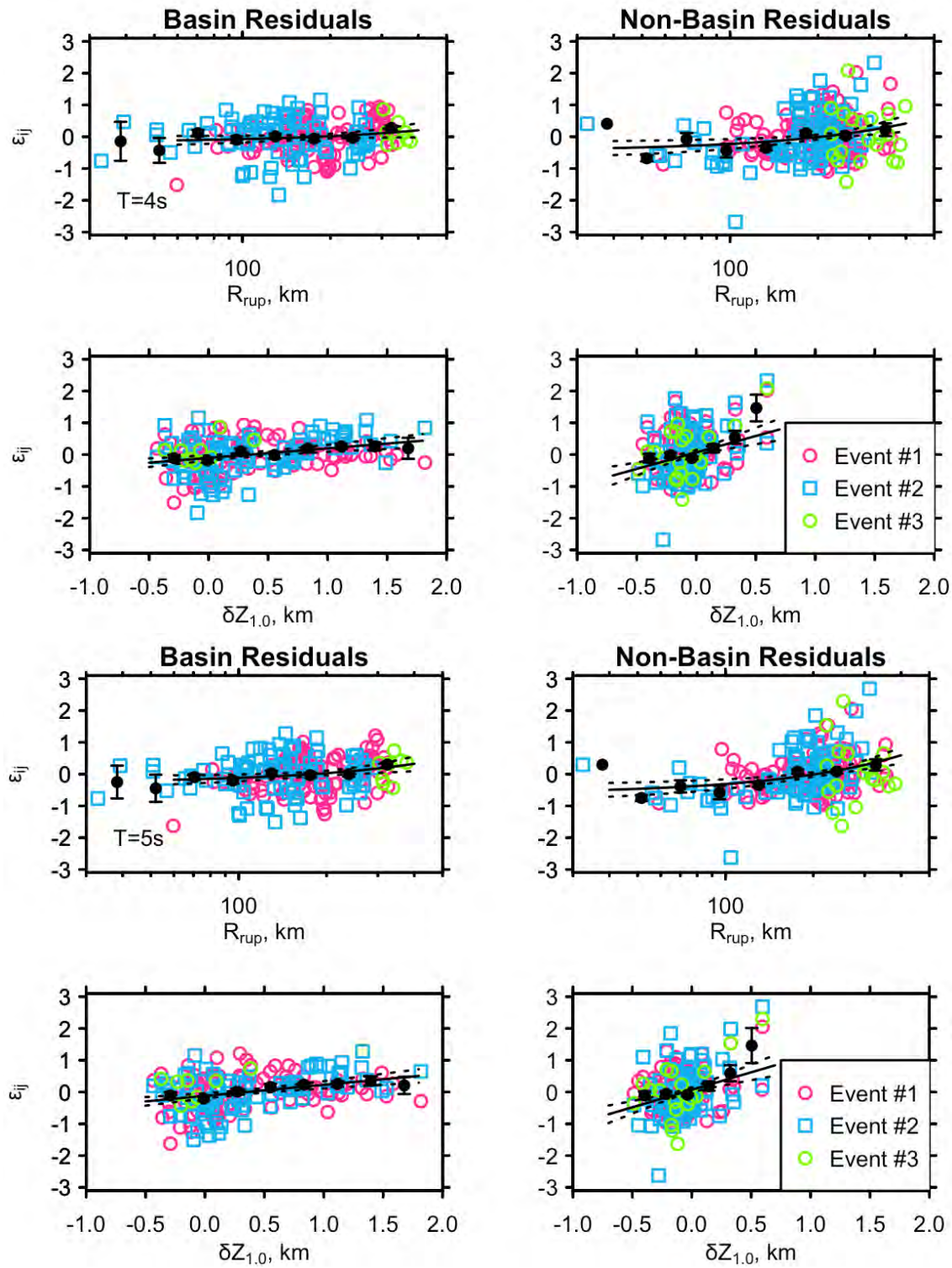


**Figure 14**. Continued.

**Estimation of Basin effects**

To study basin effects we typically consider the basin-depth parameter $z_{1.0}$, which is the depth to which $V_s$ becomes equal to 1.0 km/s. Similar to what was found in Boore et al (2014) we also observed stronger trends of residuals ($\varepsilon_{ij}$) against depth differential $\delta z_1$ (Equation 4) than basin depth itself ($z_{1.0}$), so $\delta z_1$ was adopted in the analysis.

$$\delta z_1 = z_{1.0} - \mu_{z1.0}(V_{S30}) \tag{4}$$

where $\mu_{z1.0}(V_{S30})$ is the prediction of an empirical model relating $z_1$ to $V_{S30}$. In the present study we used Equation 5 (proposed by Chiou and Youngs, 2014) to compute this quantity:

$$\ln(\mu_{z1.0}) = \frac{-5.23}{2}\ln\left(\frac{V_{S30}^4+412.39^2}{1360^2+412.39^2}\right) - \ln(1000) \tag{5}$$

where $\mu_{z1.0}$ and $V_{S30}$ have units of km and m/s, respectively.

In Figure 15, the top panel plots show the residuals $\varepsilon_{ij}$ against $R_{rup}$ after correcting for the distance trends that were estimated in the previous stage of processing. The bottom panels show the residuals $\varepsilon_{ij}$ against $\delta z_1$ for both basin and non-basin data. These results are shown for a suite of ground motion periods ranging from 0 to 10 seconds. Residual trends were observed in non-basin data when plotted against $\delta z_1$ so we additionally adjusted the residuals for these trends. These trends are shown in Figures 13 and 14 and the corresponding adjustments are given in Tables 2 and 3 for the two different GMPE models used.

The different symbols in the plots represent residuals from the three earthquakes of our dataset. During the previous stages of the residual analysis we did not identify systematic trends for any of the three events studied. In general, all the events are of similar type (interface subduction events) and they have similar travel paths for both basins studied so we would not expect to see statistically significant differences between them in the resulting basin effects.

Following these adjustments, the results shown at the bottom left figures represent the basin amplification effect with respect to the particular GMPE. We show the results for only one IM at short periods (0.01s and 0.02s), for which as expected there are no significant basin effects present. At longer periods, $T \geq 1$s, we find negative residuals for negative $\delta z_1$, a positive gradient for $\delta z_1 < 0.5$ km, and relatively flat trends thereafter consistent with the findings in Boore et al (2014). We applied a fit to the residuals with a functional form appropriate to describe these observations:

$$F_{\delta z_1}(\delta z_1) = \begin{Bmatrix} 0 & T < 1 \\ a(\delta z_1 - 0.5) + b & \delta z_1 < 0.5 \\ b & \delta z_1 \geq 0.5 \end{Bmatrix} \quad (6)$$

where $a$ represents the slope of the $\varepsilon_{ij}$ - $\delta z_1$ relation and $b$ the limiting value of $\varepsilon_{ij}$ for $\delta z_1 > 0.5$ km in the equation. The $a$ and $b$ values for the basin data are shown in Tables 4 and 5 for Abrahamson et al. (2012) and Zhao et al (2006) GMPEs, respectively.

**Table 2.** Modified GMPE Parameters for Constant and Distance-Scaling Terms for Abrahamson et al. (2012) GMPE.

| Per (s) | $\varphi$ | $\tau$ | $\sigma$ | *Distance Slope Basin* | *Distance Intercept Basin* | *Distance Slope Non-basin* | *Distance Intercept Non-basin* | *Basin Effect Slope Non-basin* | *Basin Effect Intercept Non-basin* |
|---|---|---|---|---|---|---|---|---|---|
| **0.02** | 0.58774 | 0.50133 | 0.77251 | -0.00220 | 0.39410 | -0.00478 | 0.98707 | -0.03743 | -0.00242 |
| **1.00** | 0.47343 | 0.44439 | 0.64932 | -0.00123 | 0.22740 | -0.00096 | 0.19482 | 0.40743 | 0.02637 |
| **1.50** | 0.50993 | 0.45105 | 0.68079 | -0.00065 | 0.12097 | -0.00019 | 0.03585 | 0.70738 | 0.04579 |
| **2.00** | 0.49185 | 0.47056 | 0.68069 | -0.00024 | 0.04558 | 0.00033 | -0.07175 | 0.99048 | 0.06412 |
| **2.50** | 0.49668 | 0.51167 | 0.71309 | 0.00011 | -0.01528 | 0.00123 | -0.25784 | 1.02927 | 0.06663 |
| **3.00** | 0.49436 | 0.48599 | 0.69324 | 0.00045 | -0.07612 | 0.00189 | -0.39038 | 1.09036 | 0.07058 |
| **4.00** | 0.50912 | 0.33310 | 0.60840 | 0.00119 | -0.20781 | 0.00272 | -0.55969 | 1.49443 | 0.09674 |
| **5.00** | 0.52316 | 0.20742 | 0.56278 | 0.00151 | -0.26510 | 0.00336 | -0.68639 | 1.54815 | 0.09877 |
| **7.50** | 0.53258 | 0.00002 | 0.53258 | 0.00161 | 0.54832 | 0.00251 | -0.50558 | 1.51091 | 0.09239 |
| **10.0** | 0.48107 | 0.00002 | 0.48107 | 0.00031 | 0.48219 | 0.00184 | -0.35972 | 1.31386 | 0.07253 |

**Table 3.** Modified GMPE Parameters for Constant and Distance-Scaling Terms for Zhao et al. (2006) GMPE.

| Per (s) | $\varphi$ | $\tau$ | $\sigma$ | *Distance Slope Basin* | *Distance Intercept Basin* | *Distance Slope Non-basin* | *Distance Intercept Non-basin* | *Basin Effect Slope Non-basin* | *Basin Effect Intercept Non-basin* |
|---|---|---|---|---|---|---|---|---|---|
| **0.01** | 0.62355 | 0.46587 | 0.77836 | -0.00370 | 0.66671 | -0.00572 | 1.17237 | -0.24641 | -0.01595 |
| **1.00** | 0.49451 | 0.29180 | 0.57419 | -0.00273 | 0.49250 | -0.00300 | 0.61538 | 0.02941 | 0.00190 |
| **1.50** | 0.50500 | 0.39575 | 0.64159 | -0.00121 | 0.21885 | -0.00101 | 0.20728 | 0.19865 | 0.01286 |
| **2.00** | 0.47674 | 0.40654 | 0.62654 | -0.00091 | 0.16439 | -0.00056 | 0.11470 | 0.45681 | 0.02957 |
| **2.50** | 0.49078 | 0.43386 | 0.65505 | -0.00051 | 0.09167 | 0.00029 | -0.05980 | 0.52698 | 0.03411 |
| **3.00** | 0.50963 | 0.36519 | 0.62697 | -0.00024 | 0.04237 | 0.00089 | -0.18214 | 0.62659 | 0.04056 |
| **4.00** | 0.53315 | 0.18140 | 0.56316 | 0.00093 | -0.16757 | 0.00216 | -0.44207 | 1.03537 | 0.06702 |
| **5.00** | 0.53761 | 0.00002 | 0.53761 | 0.00148 | -0.26565 | 0.00302 | -0.61417 | 1.09946 | 0.07015 |

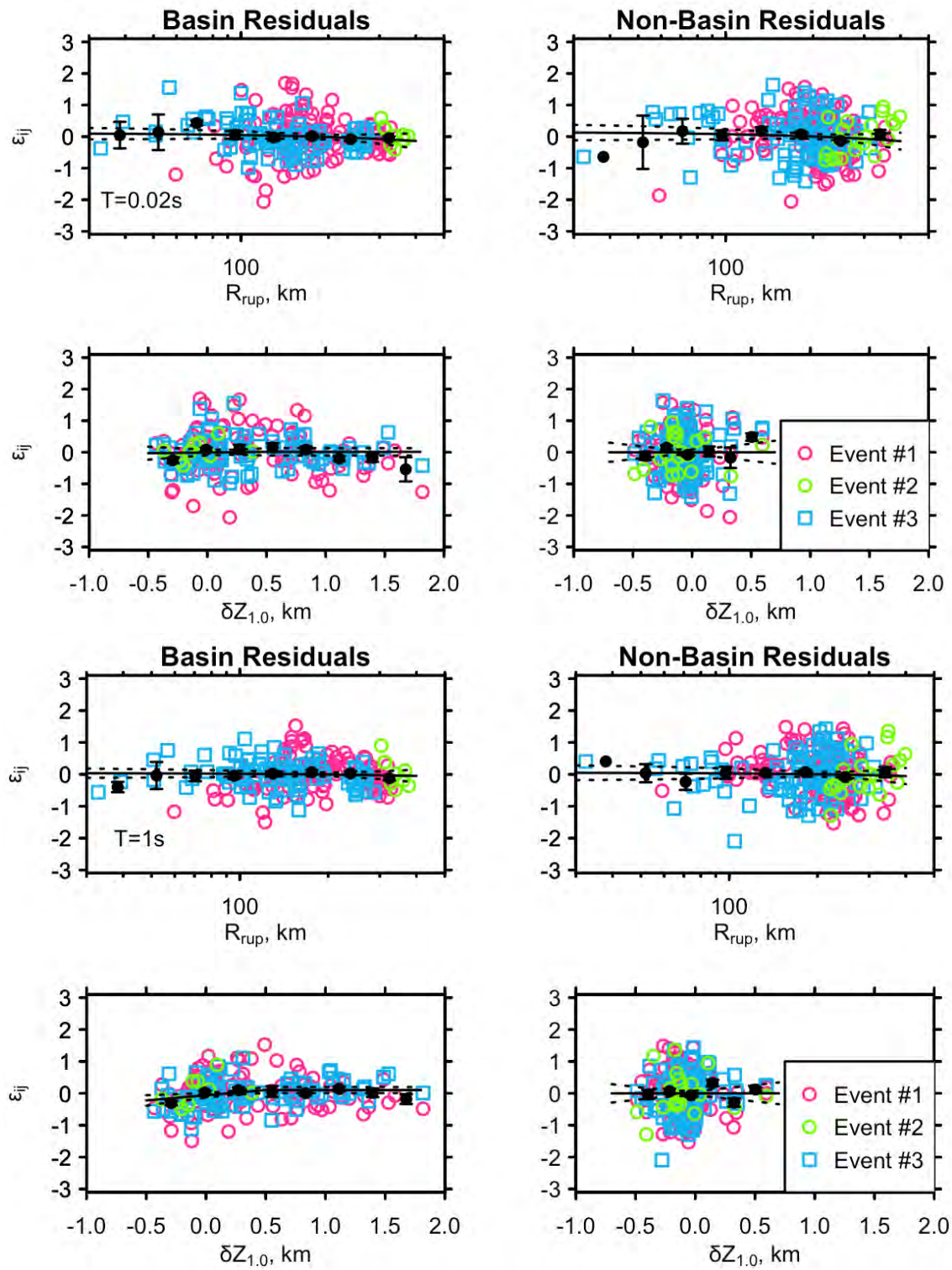


**Figure 15**. Intra-event residuals against sediment depth differential $\delta z_1$ plotted together with a proposed basin model for basin data (bottom-left plot) for the Abrahamson et al. (2012) GMPE. Colors and symbols are the same as in the previous figures.

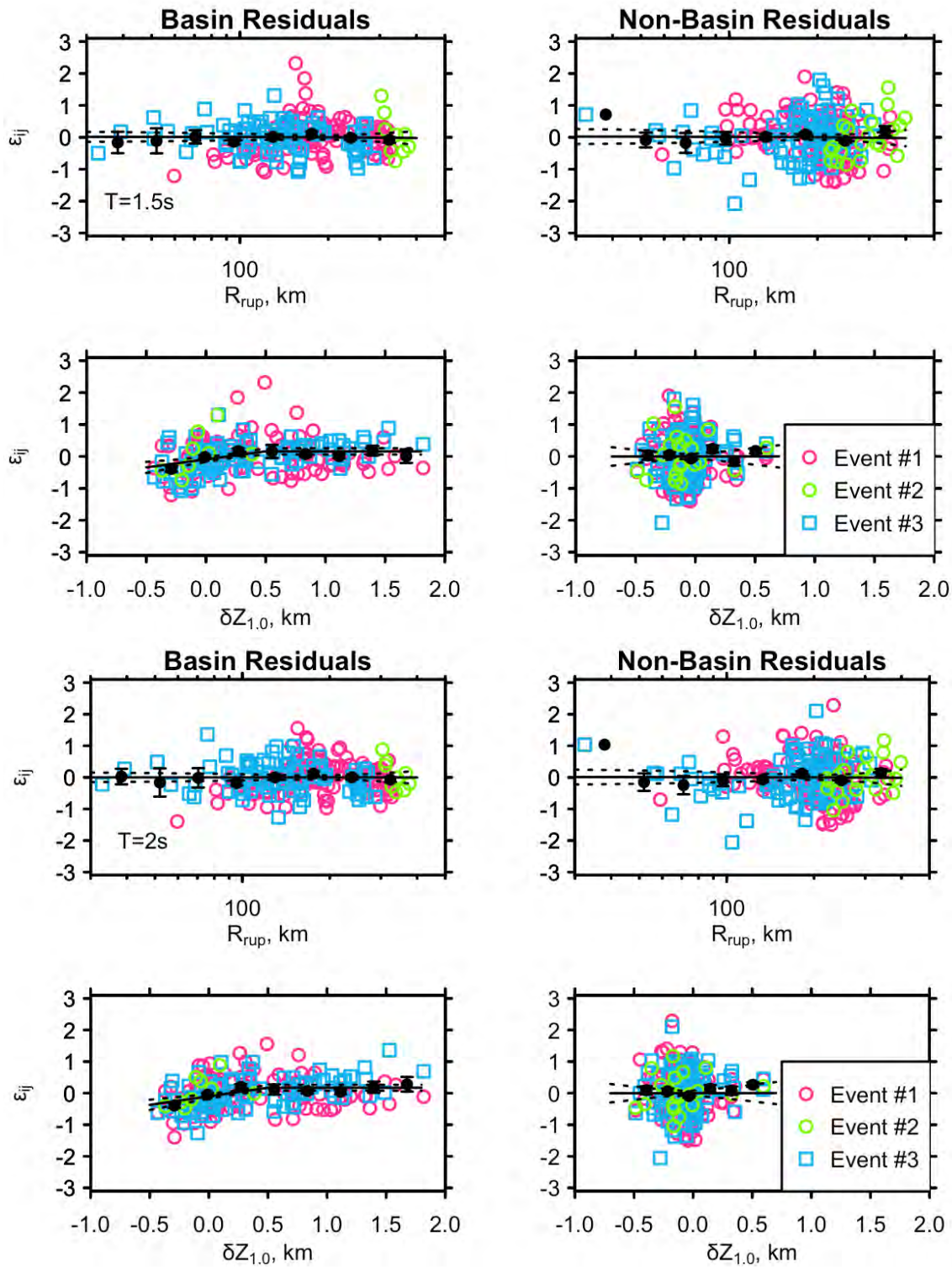


**Figure 15**. Continued.

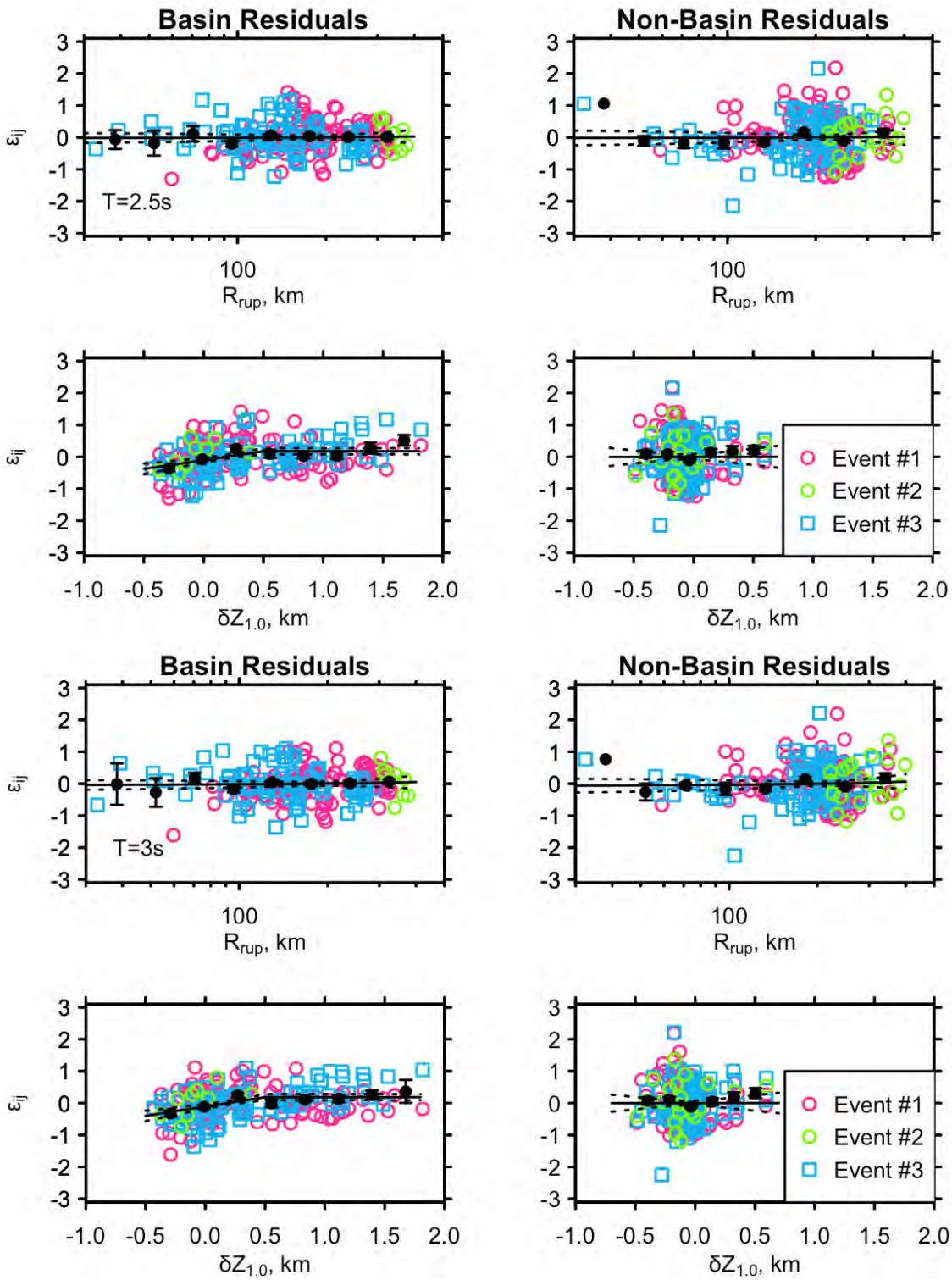


**Figure 15**. Continued.

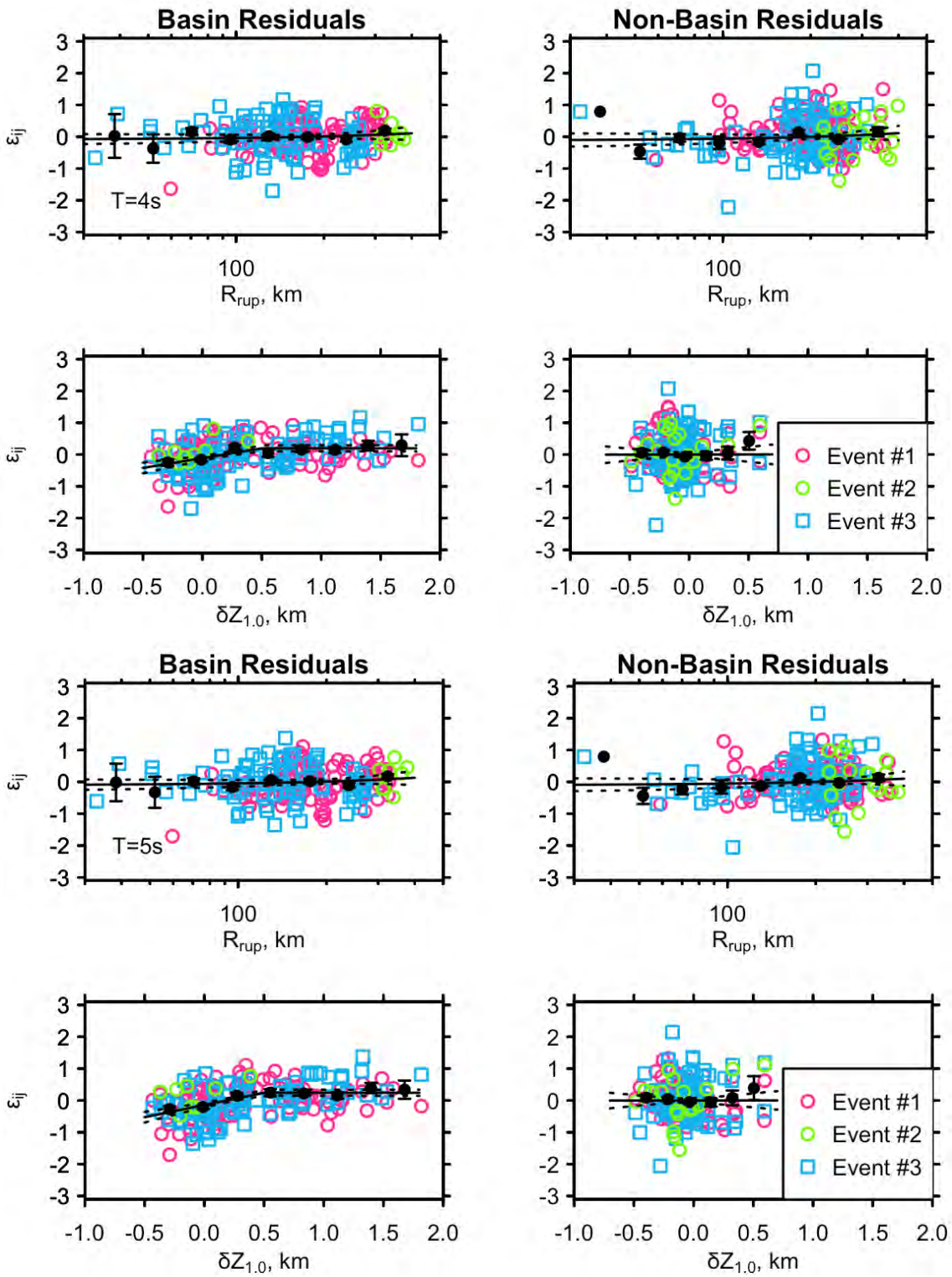


**Figure 15**. Continued.

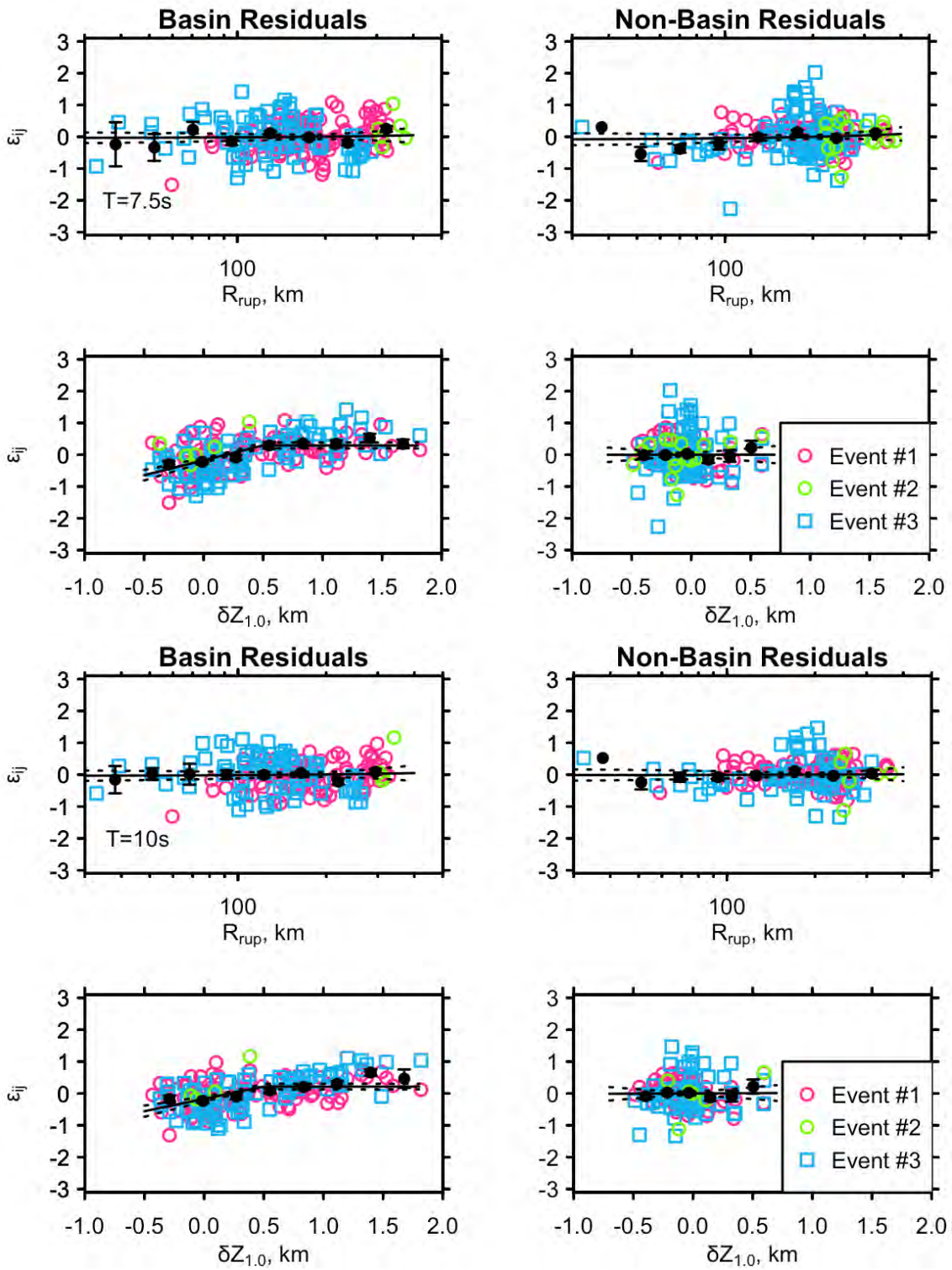


**Figure 15**. Continued.

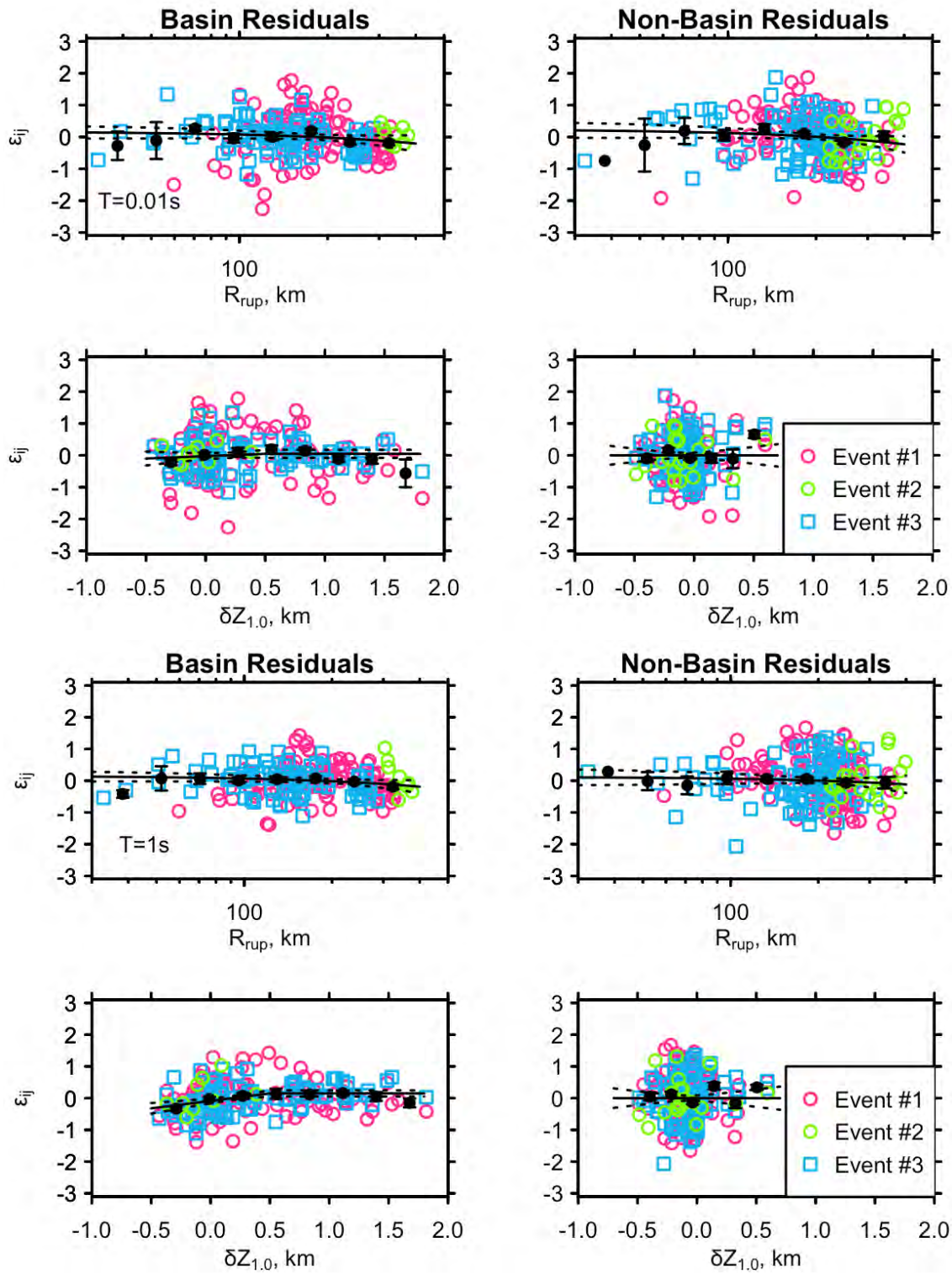


**Figure 16**. Intra-event residuals against sediment depth differential $\delta z_1$ plotted together with a proposed basin model for basin data (bottom-left plot) and for the Zhao et al. (2006) GMPE. Colors and symbols are the same as in the previous Figures.

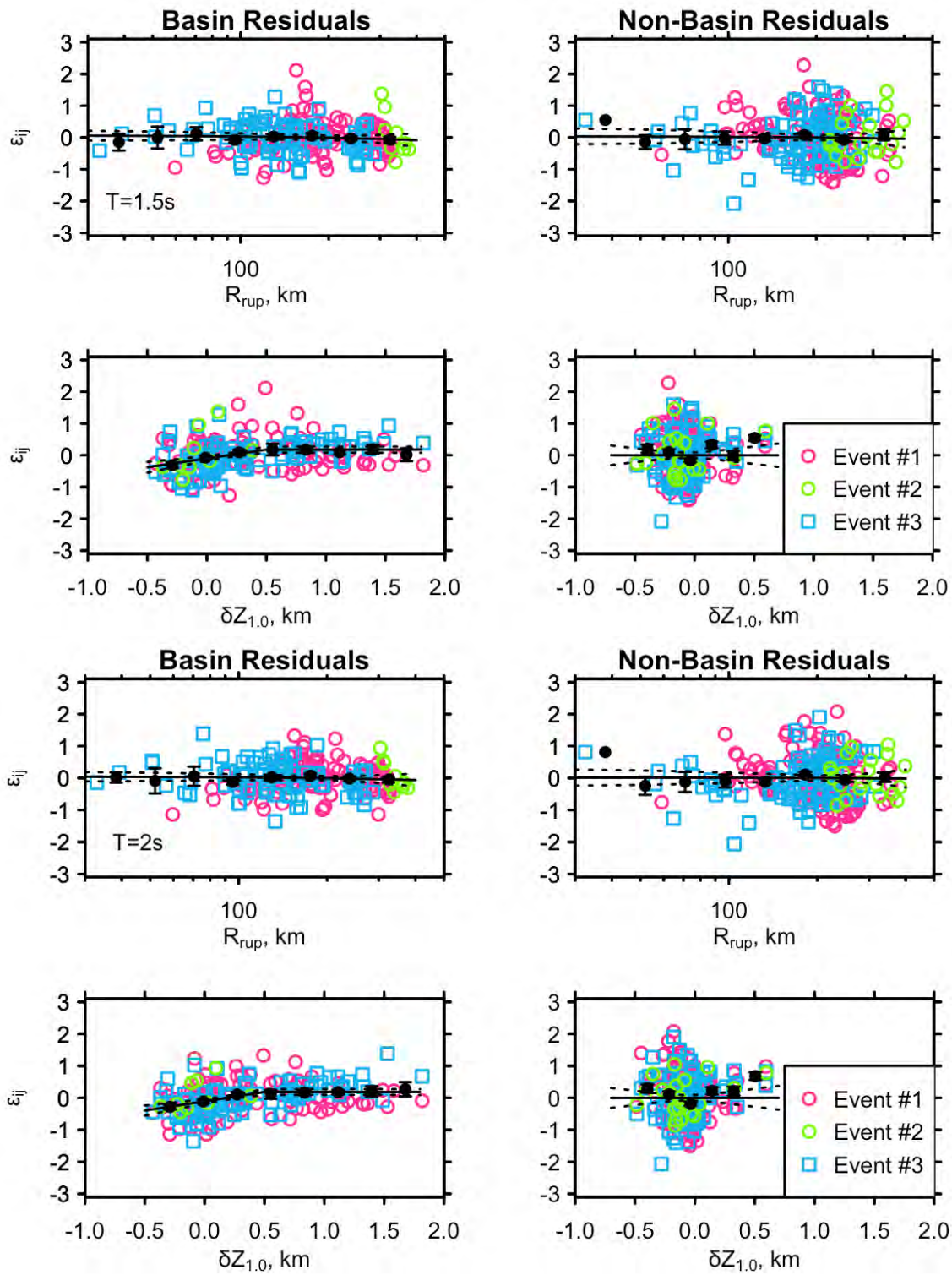


**Figure 16**. Continued.

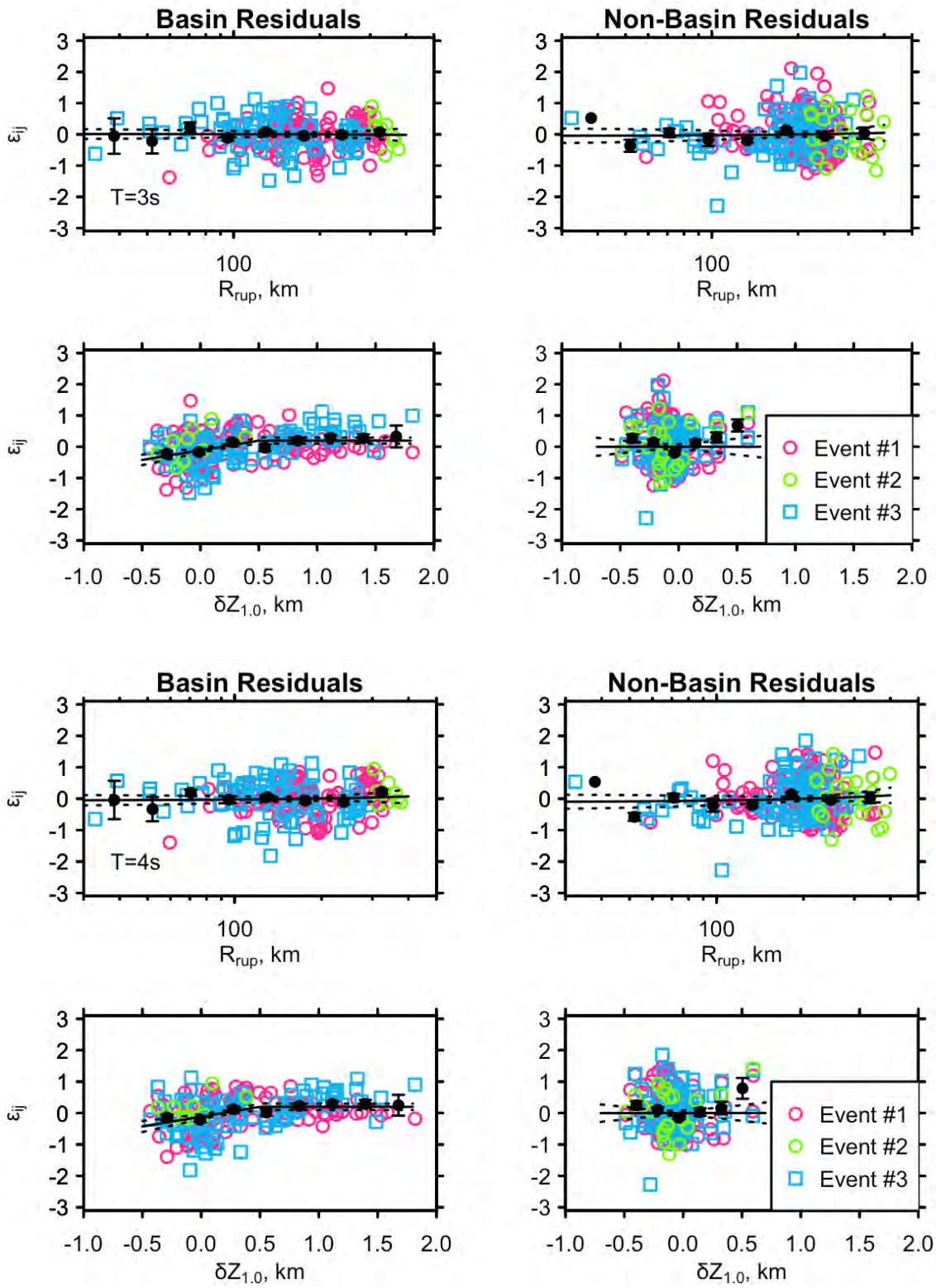


**Figure 16**. Continued.

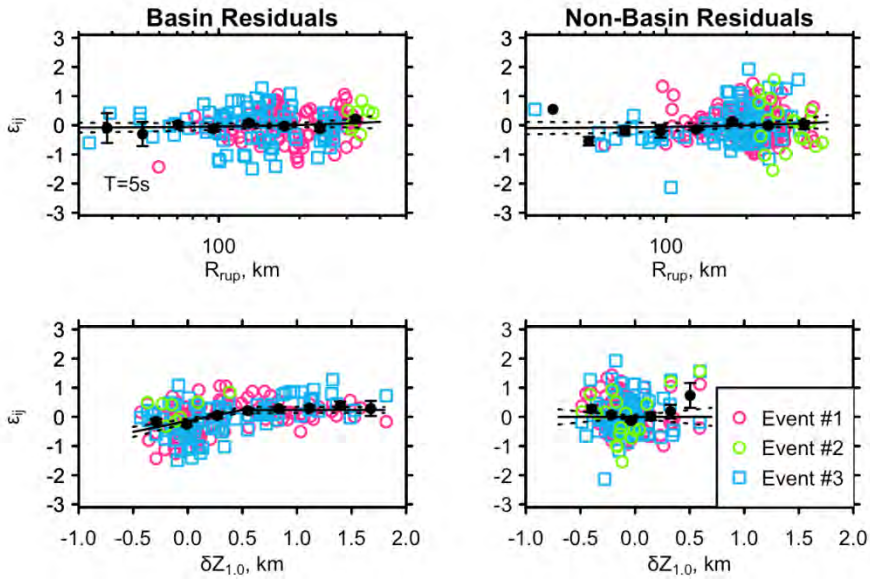


**Figure 16**. Continued.

**Table 4.** Slope and intercept values of the basin effects fit for Abrahamson et al. (2012) GMPE.

| Period (s) | Intercept (b) | Slope (a) |
|---|---|---|
| **0.02** | 0.0137 | 0.0434 |
| **1.00** | 0.1034 | 0.3268 |
| **1.50** | 0.1596 | 0.5045 |
| **2.00** | 0.1718 | 0.5431 |
| **2.50** | 0.1751 | 0.5533 |
| **3.00** | 0.1856 | 0.5866 |
| **4.00** | 0.1950 | 0.6163 |
| **5.00** | 0.2421 | 0.7670 |
| **7.50** | 0.2912 | 0.9361 |
| **10.00** | 0.2148 | 0.7718 |

**Table 5.** Slope and intercept values of the basin effects fit for Zhao et al. (2006) GMPE.

| Period (s) | Intercept (b) | Slope (a) |
|---|---|---|
| **0.01** | 0.0464 | 0.1466 |
| **1.00** | 0.1488 | 0.4703 |
| **1.50** | 0.1759 | 0.5560 |
| **2.00** | 0.1837 | 0.5805 |
| **2.50** | 0.1827 | 0.5774 |
| **3.00** | 0.1959 | 0.6193 |
| **4.00** | 0.1972 | 0.6231 |
| **5.00** | 0.2378 | 0.7534 |

**Spatial distribution of basin amplification**

In Figures 17 and 18 we show the spatial distribution of the basin amplification for the two GMPEs used. The boundaries of the two basins studied, as defined in a previous section, are shown with the dashed lines. The earthquake epicenters are shown with the colored stars. Basin amplification is defined as the exponent of the residual $\varepsilon_{ij}$, after the adjustments based on our residual analysis.

The basin amplification is more prominent for the Kanto basin given its size and depth, compared to the Niigata basin. The amplifications are larger for longer spectral periods, for both basins studied. Larger amplifications are observed in the deeper parts of the basins. Some small, localized, exceptions for the Kanto basin are observed which could be attributed to strong local site effects, since we have not performed a site effect adjustment per se in the residuals. The maximum amplifications observed are of the order of 1.6-1.8, which is in agreement with what other researchers have found using empirical data (e.g. Somerville et al., 2004; Choi et al., 2005) and simulations (Frankel et al., 2015; Delorey et al., 2014; Day et al., 2008).

The differences between the two GMPEs used are small, which shows that our analysis is quite robust. It could also suggest that basin amplifications could be insensitive to the reference ground motion model that we select, and are mostly controlled by the general characteristics of the basin, the location of the seismic source with respect to the basin (Choi et al, 2005) and the type of the earthquake. These last conclusions are not strongly supported given the limited number of earthquakes included in our database. A larger number of different types of events and basins are needed to perform a more robust statistical analysis and support these preliminary findings.

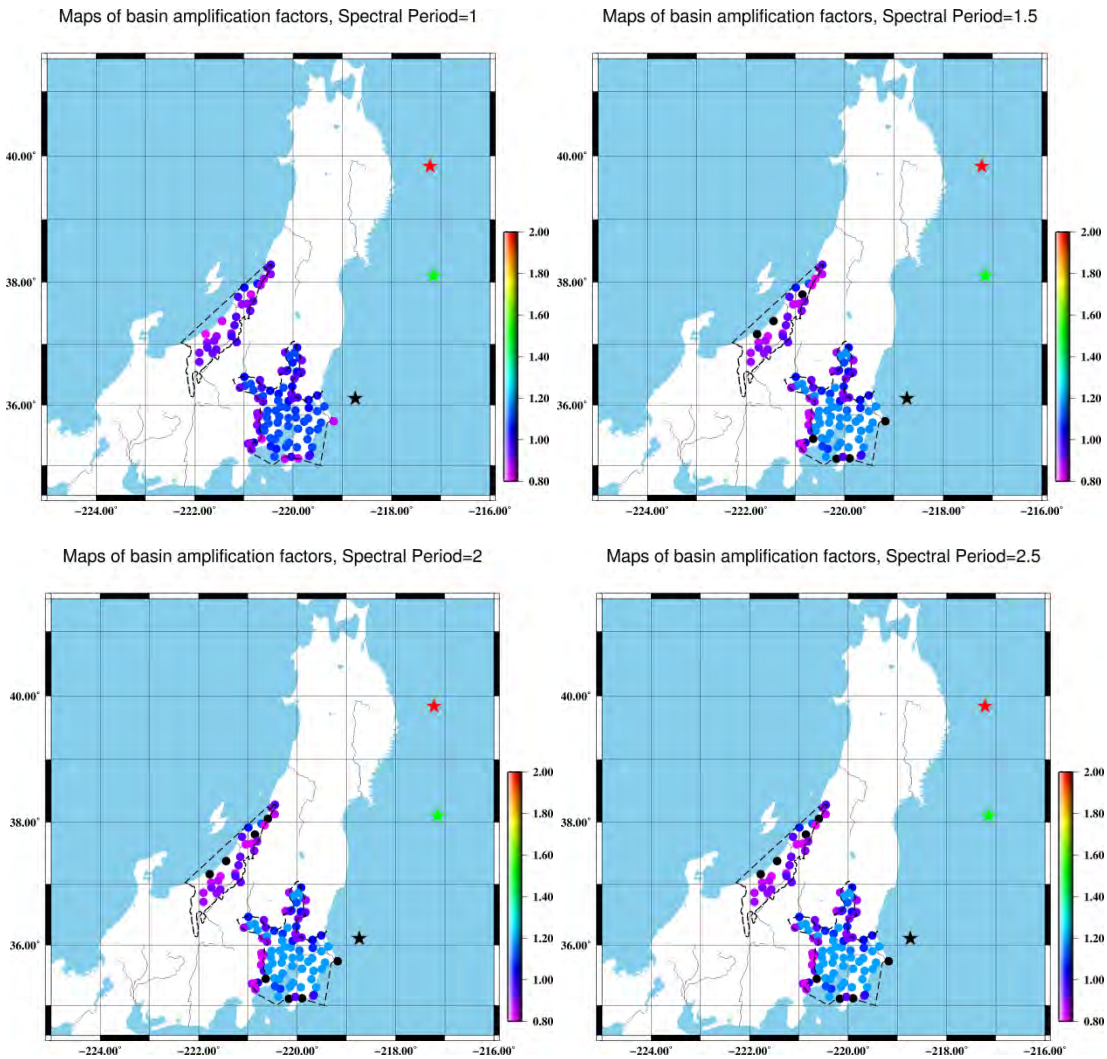


**Figure 17**. Basin amplification maps for the Kanto and Niigata basins for the Abrahamson et al. (2012) GMPE. The earthquakes used in the analysis are shown with the colored stars.

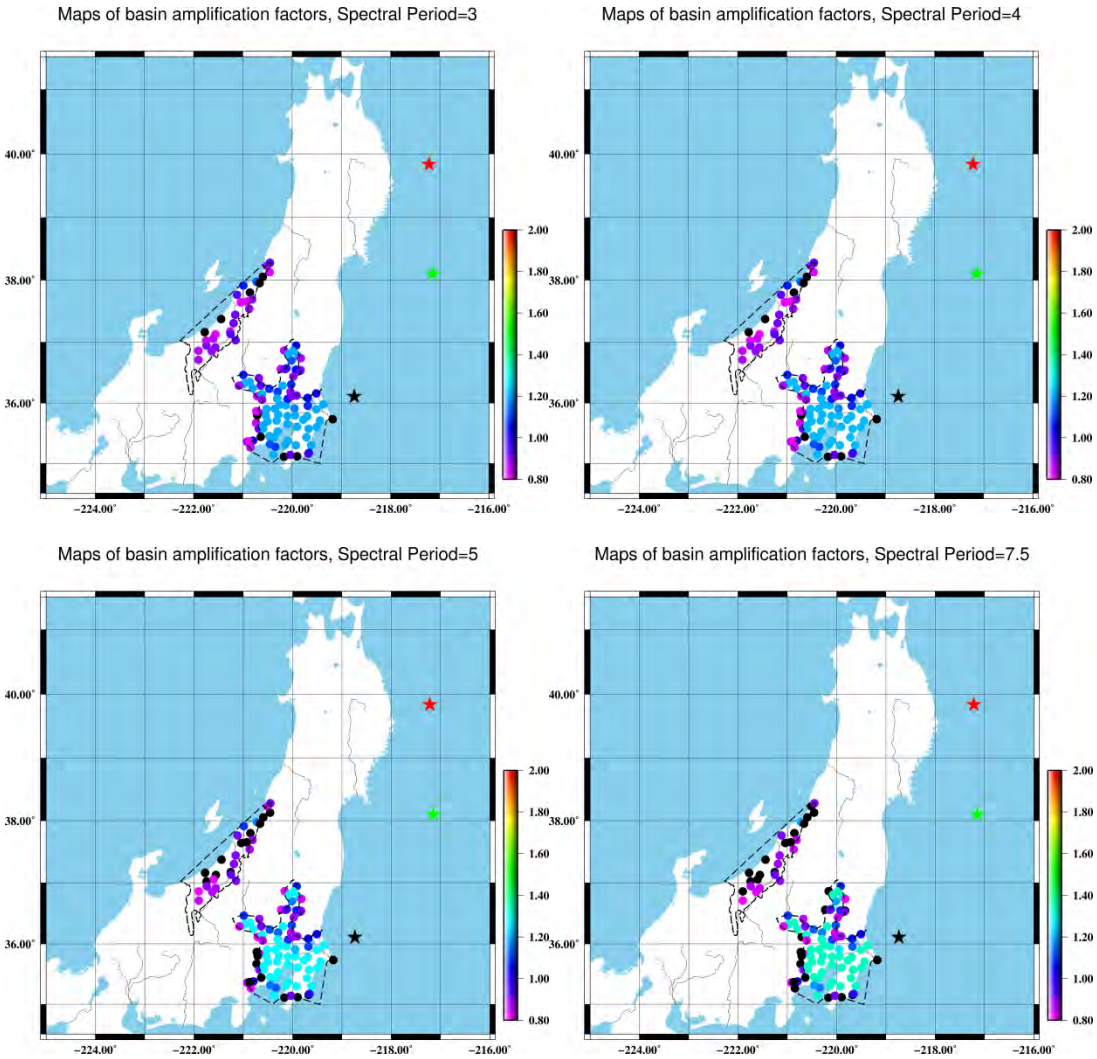


**Figure 17**. Continued.

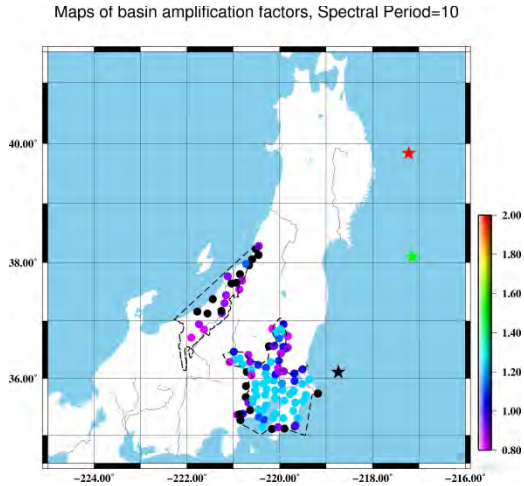


**Figure 17**. Continued.

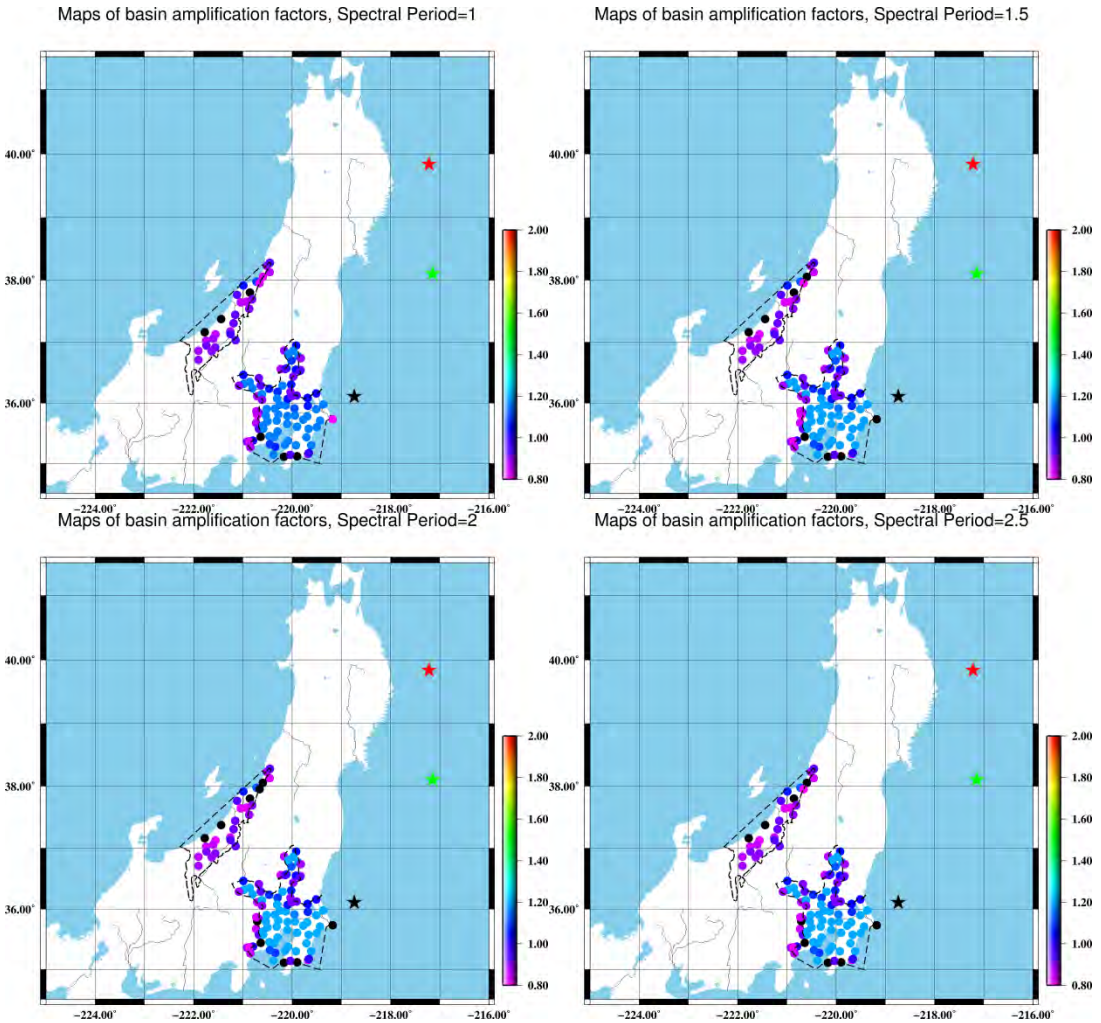


**Figure 18**. Basin amplification maps for the Kanto and Niigata basins for the Zhao et al. (2006) GMPE. The earthquakes used in the analysis are shown with the colored stars.

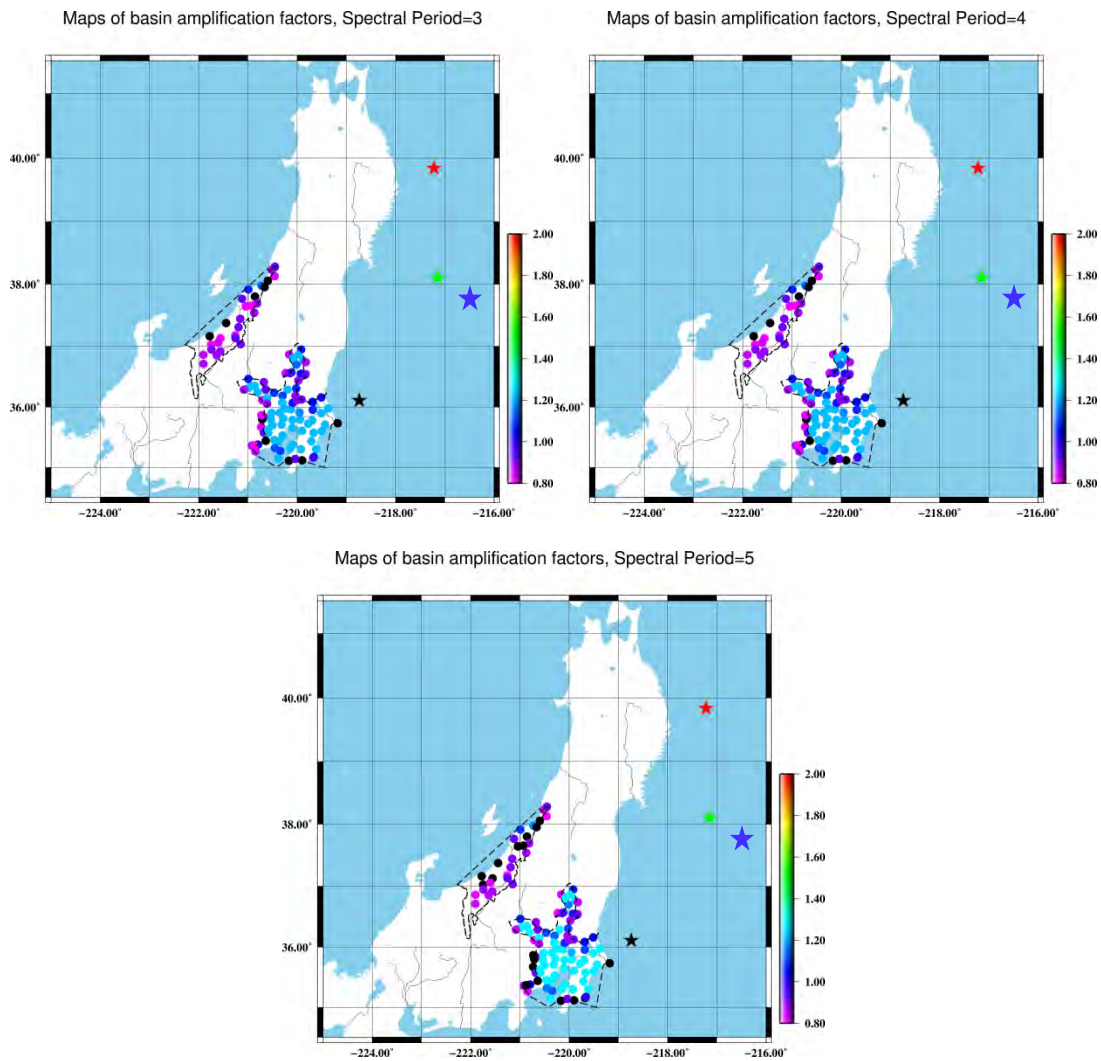


**Figure 18**. Continued.

## Amplification Factors from Long Period 3D simulations

### Computational Method for 3D Simulations

We selected a finite difference code (Graves, 1996; Graves and Pitarka 2010) to simulate 3D wave propagation. This code uses a uniform, structured, cubic mesh with staggered locations of the velocity and stress components, and a differencing scheme that is fourth-order accurate in space and second-order accurate in time. Seismic attenuation is incorporated by implementing anelastic losses using the coarse memory variables representation (Day et al. 2008, Graves and Day 2003). Anelastic attenuation is introduced in the form of frequency-independent quality factors (Q). This method was used in Wei et al. (2012) to control the accuracy of the Tohoku M9.0 rupture model. Wei et al. (2012) show that the current finite difference code is able to successfully simulate the long period Tohoku M9.0 recordings.

**Earth Structure Model**

A 3D velocity model was interpolated from the Koketsu et al. (2008) model to the required spatial resolution. This 3D representation of the earth model including basins was used to synthesize time series possessing basin effects. The Koketsu et al. (2008) Japan Integrated Velocity Structure Model (JIVSM) includes the 3D structure of the entire crust and upper mantle (including the Moho and plate interfaces) with a horizontal resolution of about 1 km, and consists of 23 isovelocity layers with $V_S$ in the range of 0.35 – 4.6 km/s. Interpolated velocity models intended for 3D simulations cover different areas for different events to make the most efficient use of time and available resources.

The basin computations required large computational resources. In order to speed up the computations as well as to lower their memory requirements, we created three velocity sub-models, with smaller dimensions than the original one, which are assigned to the three different events in Table 1. Two cross sections of an interpolated model from Koketsu et al. (2008) are shown in Figures 20 and 21.

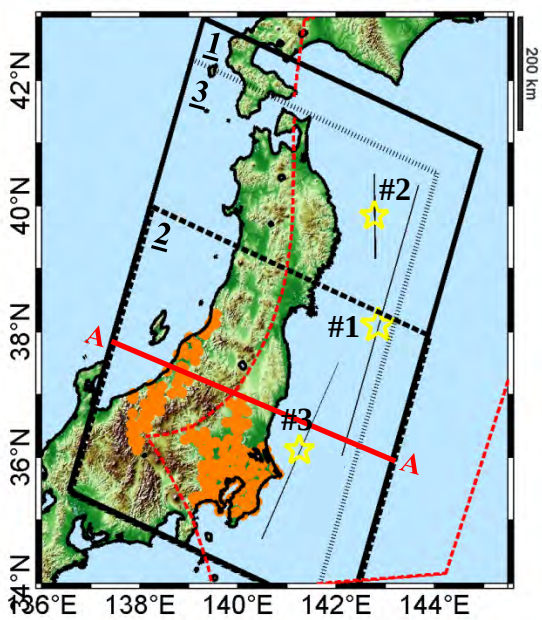


**Figure 19**. Events and velocity models initially developed for the 3D simulations. Earthquake event numbers refer to the event ID in Table 1. Velocity models are shown with underlined numbers. Table 1 shows the velocity models associated with each earthquake simulation. Orange dots show recording sites within and on the boundaries of the basins. Cross section AA is shown in Figure 20.

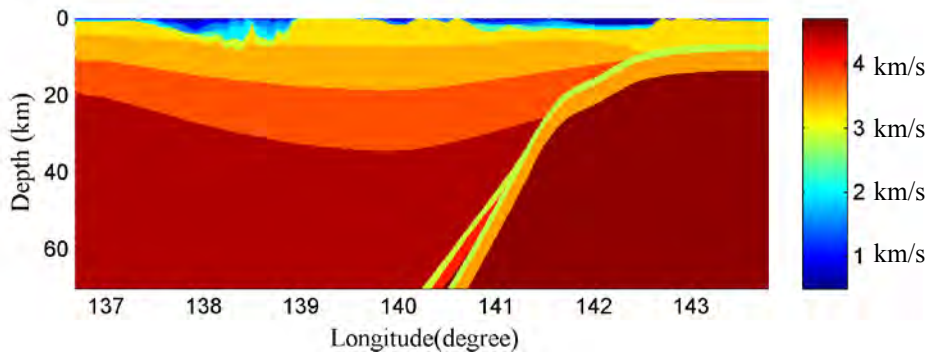


**Figure 20**. The vertical cross section AA (as shown in Figure 19) showing the shear-wave velocity structure and subduction zone.

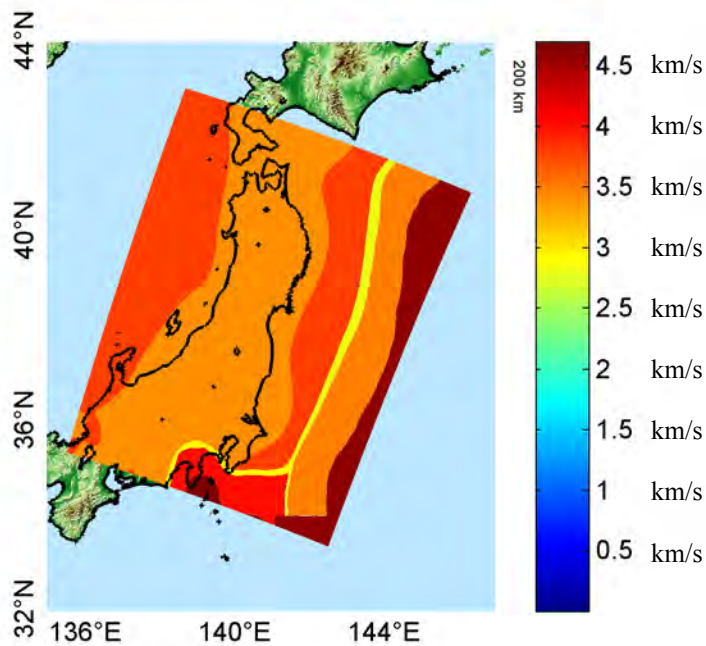


**Figure 21**. A horizontal slice of the shear-wave velocity model 1 at depth 14 km, showing the subduction zone east of Honshu.

**Depth to Shear-wave Velocity of 1.0 km/s ($z_{1.0}$)**

The depth to $V_S$=1.0 km/s ($z_{1.0}$) is the parameter used to define the basin boundaries and sediment thickness. Figure 22 shows the $z_{1.0}$ values as acquired from three different sources, the Koketsu et al. (2008) 3D velocity model, the Ancheta et al. (2014) data base, and estimates from $V_{S30}$ at

each recording stations using equation (5) (Boore et al. 2014). As observed in the right panel, the $z_{1.0}$ values derived from $V_{S30}$ do not reflect the existence of the basins.

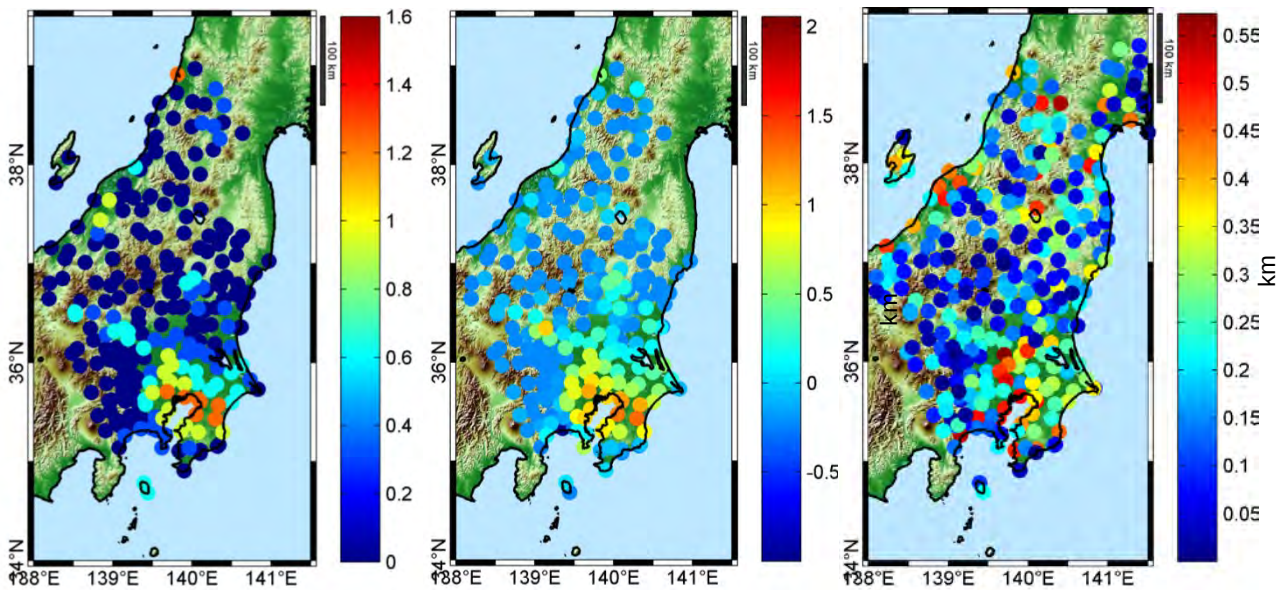


**Figure 22**. Depth to the shear-wave velocity of 1.0 km acquired from realistic 3D velocity model (left), reported by Ancheta et al. (2014) (middle) and calculated from $V_{S30}$ using relations in Boore et al. (2014) (right) at the locations of KiK-net and K-NET stations in the vicinity of the Kanto and Niigata Basins.

**Extended 1D Velocity Model**

To investigate the amplification effects of basins in Japan, we compared simulations from a structural model containing basins with one that does not contain basins. We used a representative 1D velocity model and extended it horizontally to generate a pseudo-3D velocity model whose mechanical properties change in the vertical direction only. Figure 23 shows the 1D velocity model expanded to a pseudo-3D velocity model. We constructed this velocity model in a way that has a $V_{S30}$ close to that of non-basin sites equal to 500 m/s. The deeper layers are defined based on a representative model for Iwate station.

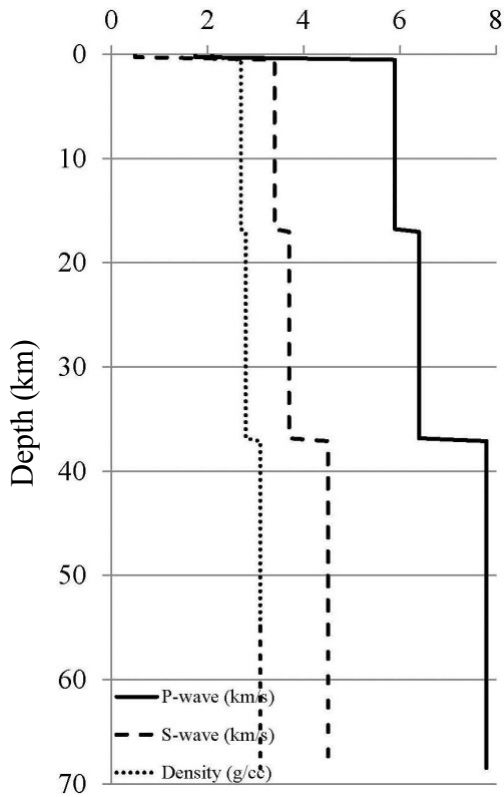


**Figure 23**. 1D velocity model used to construct the pseudo-3D model used in the simulations.

**Accuracy of Simulations at High Frequency**

The maximum frequency and time step at which the simulated time series can be considered accurate depends on the spatial resolution of the 3D velocity model and the minimum shear wave velocity of the model. The following equations are used to estimate maximum reliable time step and frequency:

$$\Delta t_{\max} = \frac{6h}{7\sqrt{3}V_{P,\max}} \tag{7}$$

$$f_{\max} = \frac{V_{S,\min}}{5h} \tag{8}$$

Interpolation of the velocity model to smaller spatial resolution for a higher maximum frequency would be meaningless considering that high resolution velocity information is not available, and impractical considering the large resources that would be necessary to accomplish the simulations. We used a spatial resolution of 275 meters with a time step of 0.015 seconds. These values ensure that response calculations are reliable down to 2.75 seconds.

**Tohoku M9.0 Simulation**

The kinematic rupture model used for this event is from Wei et al. (2012) as shown in Figure 24. Graves et al. (2012) used the rupture model of Wei et al. (2012) to simulate the recorded ground motions of the Tohoku mainshock using the Koketsu et al. (2008) 3D velocity model. This source model is characterized by very large, very long period (>20 s) displacement on the shallow part of the plate interface, which generated the tsunami. Relatively smaller, shorter period (<20 s) displacement on the deeper part of the fault generated the strong ground motions.

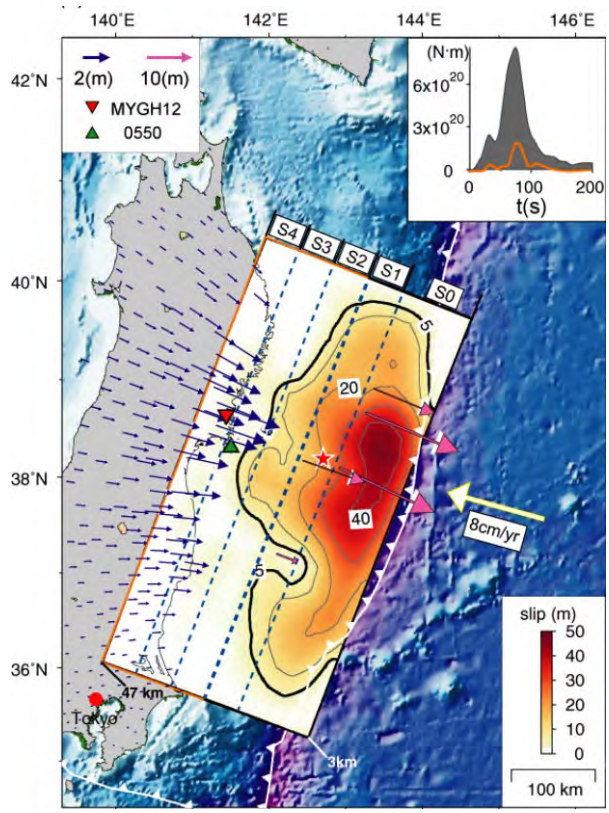


**Figure 24.** Rupture model of the 2011 Tohoku mainshock by Wei et al. (2012).

**Tohoku Aftershock M7.4 Simulation**

A kinematic rupture model is generated using the technique developed and explained by Graves and Pitarka (2010) where the stochastic slip history on the fault is modeled using three key parameters including rise time, rake, and slip at each grid point on the fault plane. Figure 25 shows these three parameters for the aftershock (ID #2 in Table 1) used in the simulations.

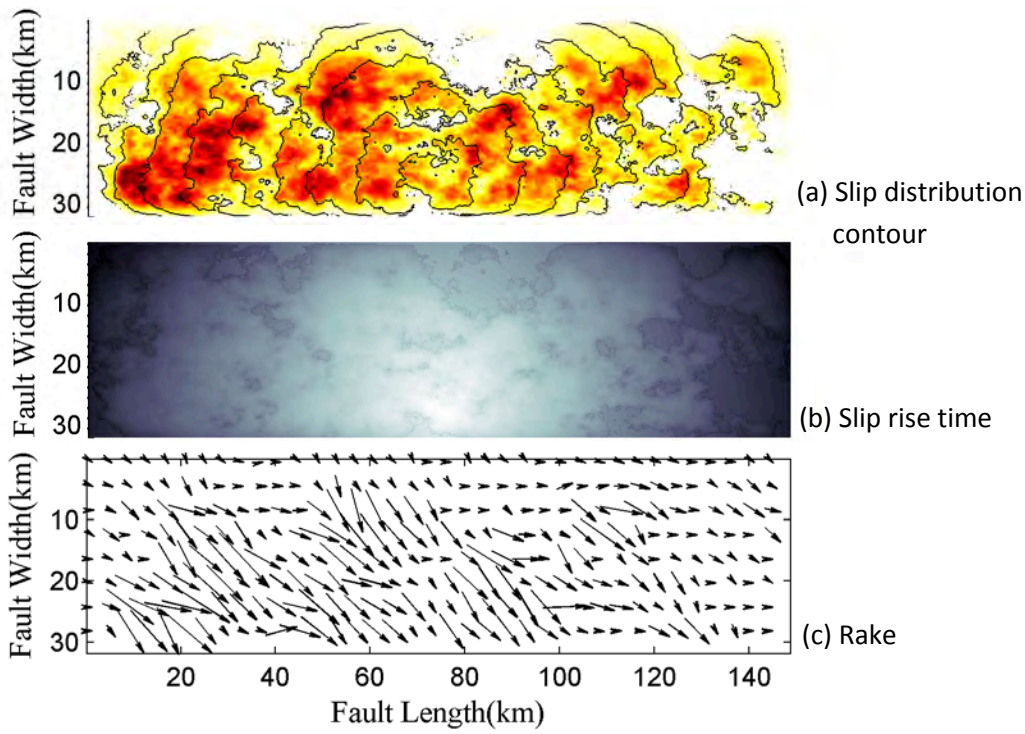


**Figure 25**. Kinematic rupture model developed for the Tohoku aftershock M7.4 (a) Panel shows slip distribution with rupture front contours at 1 s intervals superimposed, (b) panel shows distribution of slip rise time, and (c) panel shows distribution of rake.

The generated slip for each grid point on the fault is propagated through the 3D velocity model using a fourth order finite difference technique, similar to that in the Tohoku M9.0 mainshock simulation.

**Amplification from 3D Simulations**

Finite difference simulations were used to determine amplification in the Kanto and Niigata basins. Amplification is calculated as the spectral ratio of response spectra of the simulations from the realistic 3D model and the pseudo-3D model. Figure 26 shows two examples of simulated time series and their spectral ratio for station CHB002 for the mainshock and aftershock of the Tohoku M9.0 earthquake. Figure 27 and Figure 28 present the amplification maps for the Tohoku M9.0 mainshock and its aftershock.

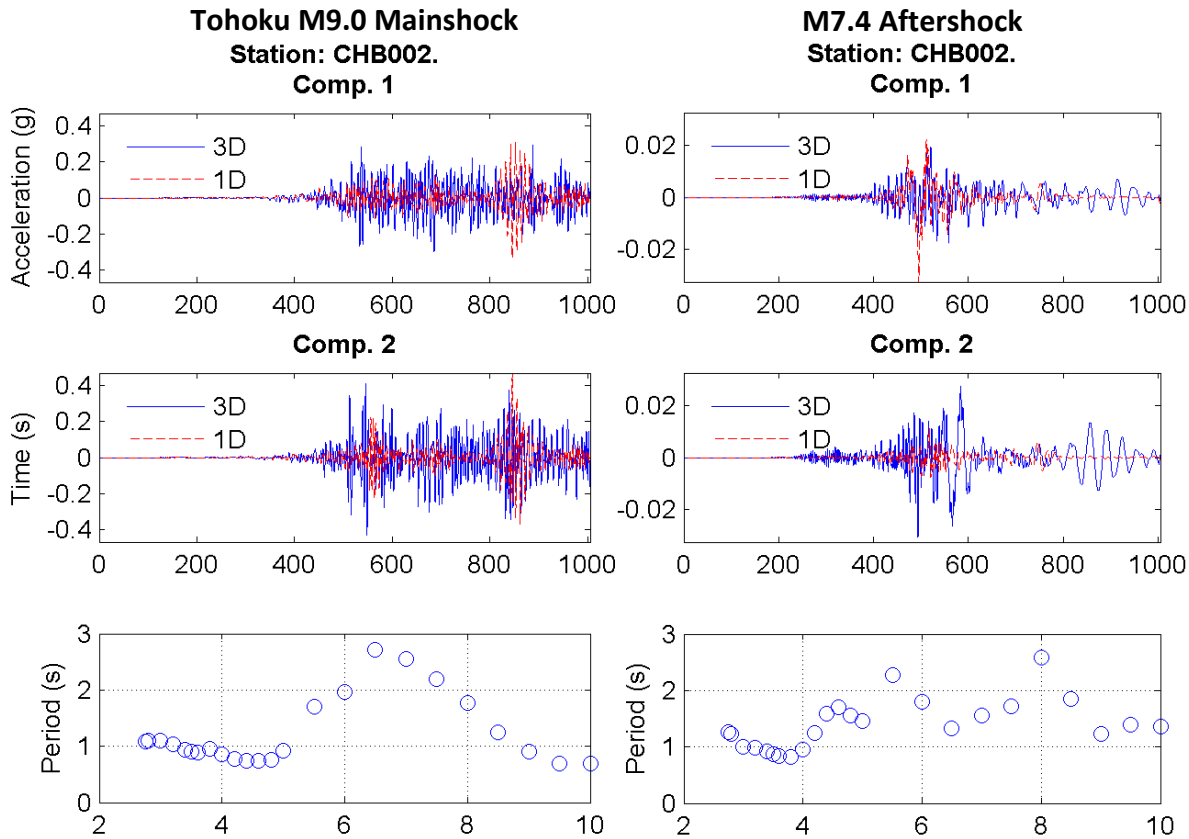


**Figure 26.** Two horizontal components of the simulated time series using the realistic 3D and pseudo-3D models simulated at station CHB002 for the mainshock (left) and aftershock (right). The 3D/1D spectral ratios are plotted in the bottom panels.

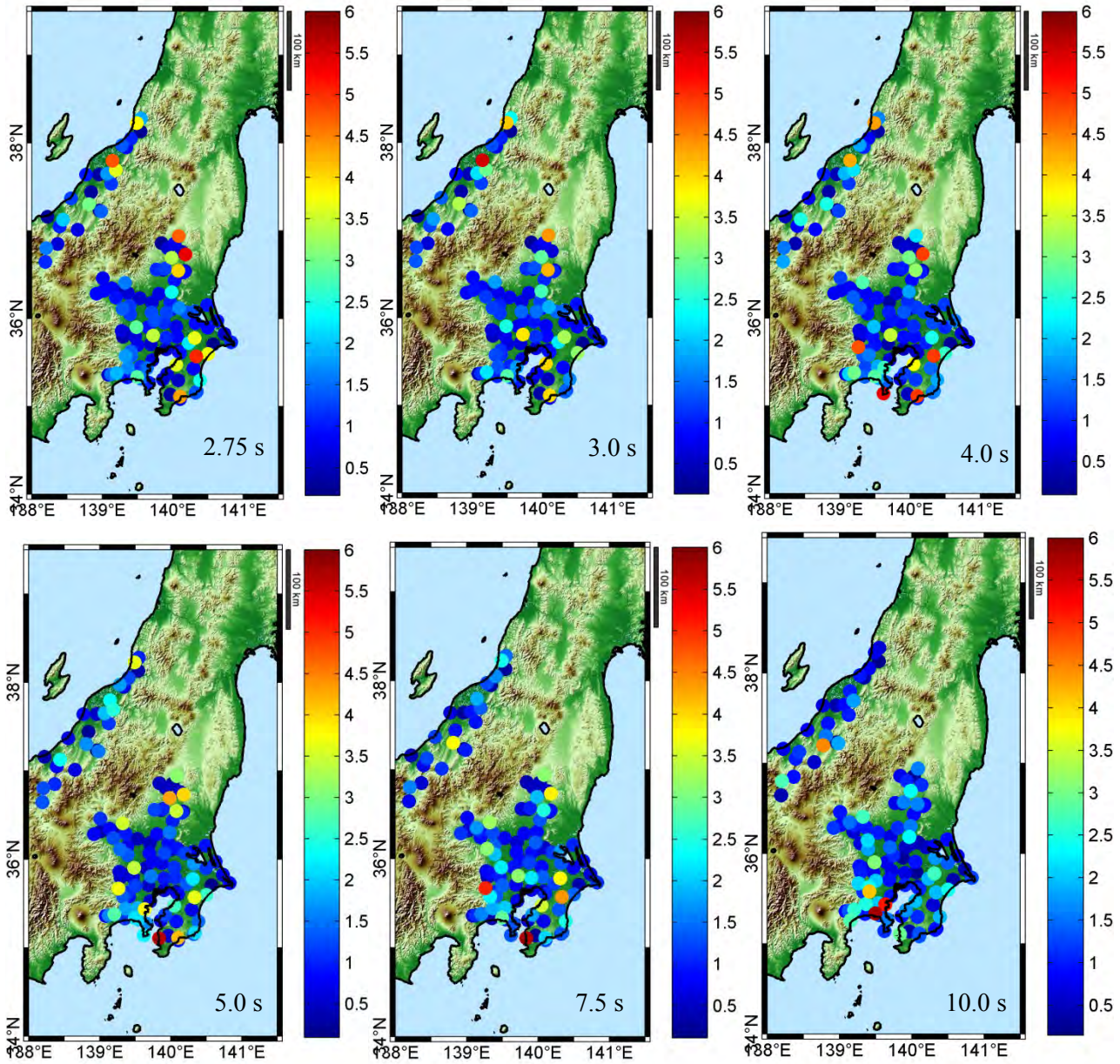


**Figure 27.** Maps of basin amplification factors in Japan from the Tohoku M9.0 earthquake 3D simulations at different periods.

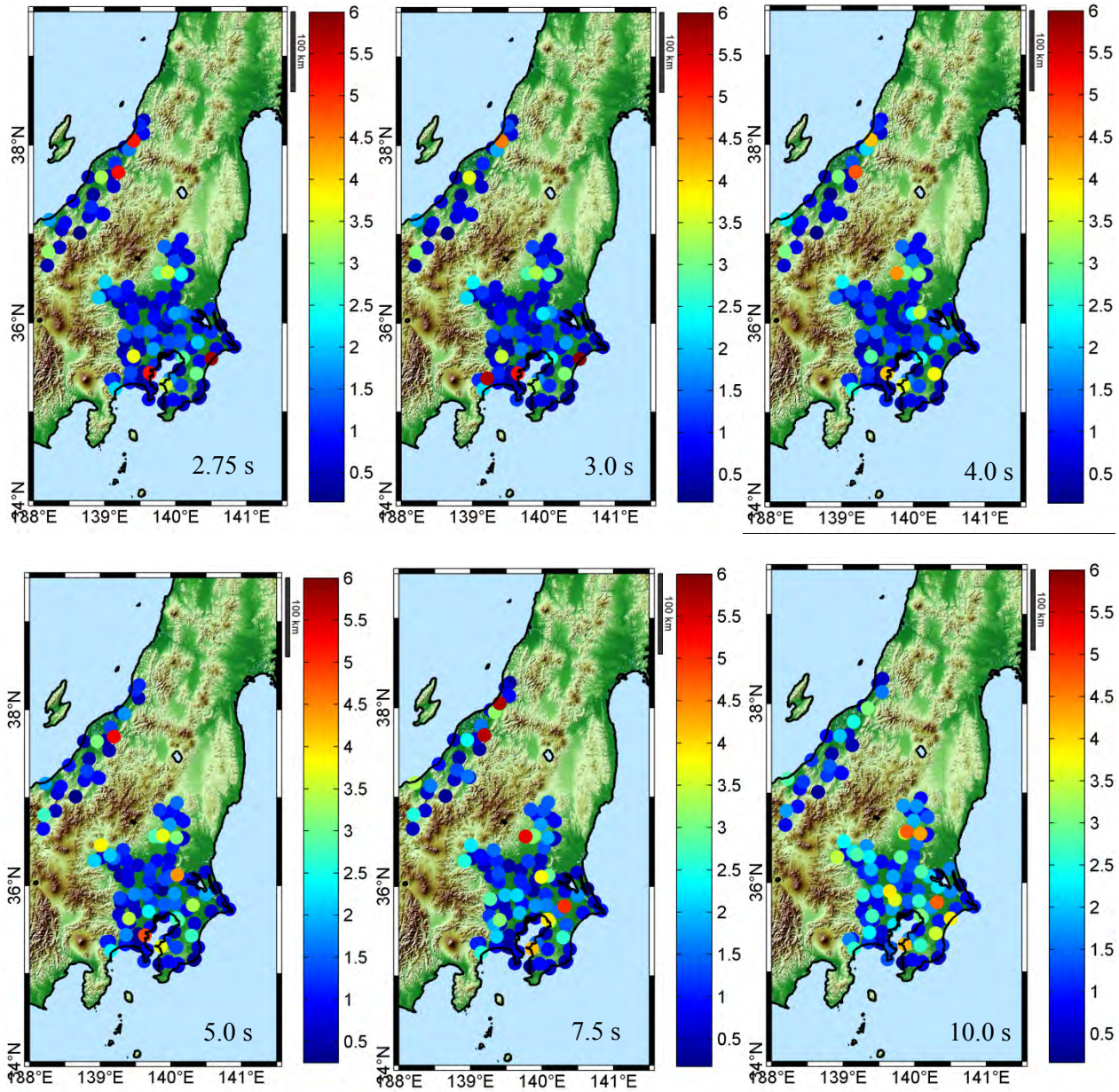


**Figure 28.** Maps of basin amplification factors in Japan from the Tohoku aftershock 3D simulations at different periods.

Figure 29 shows the amplification from 3D simulations for each site location versus depth differential (Equation 6) at different spectral periods. For the spectral periods studied the amplifications do not show a strong dependence with respect to the depth differential. Therefore, we estimate the amplification factor at each spectral period by computing the average amplification across all depth differentials. The estimated amplification factors are listed in Table 6.

Another way of presenting the amplification data is by studying the trend of residuals versus basin depth ($z_{1.0}$). Figure 30 presents the basin-depth dependence of amplification for different periods following Day et al. (2008). Amplification factors for different periods are plotted together in Figure 31. It is observed that amplification increases as basin depth increases similar to Day et al. (2008).

Figure 32 compares the amplification factors obtained from the analysis of observations in the previous section (Table 5) with those obtained from the 3D simulation in this section (Table 6). The amplifications obtained from 3D simulations are systematically higher than those obtained from the data.

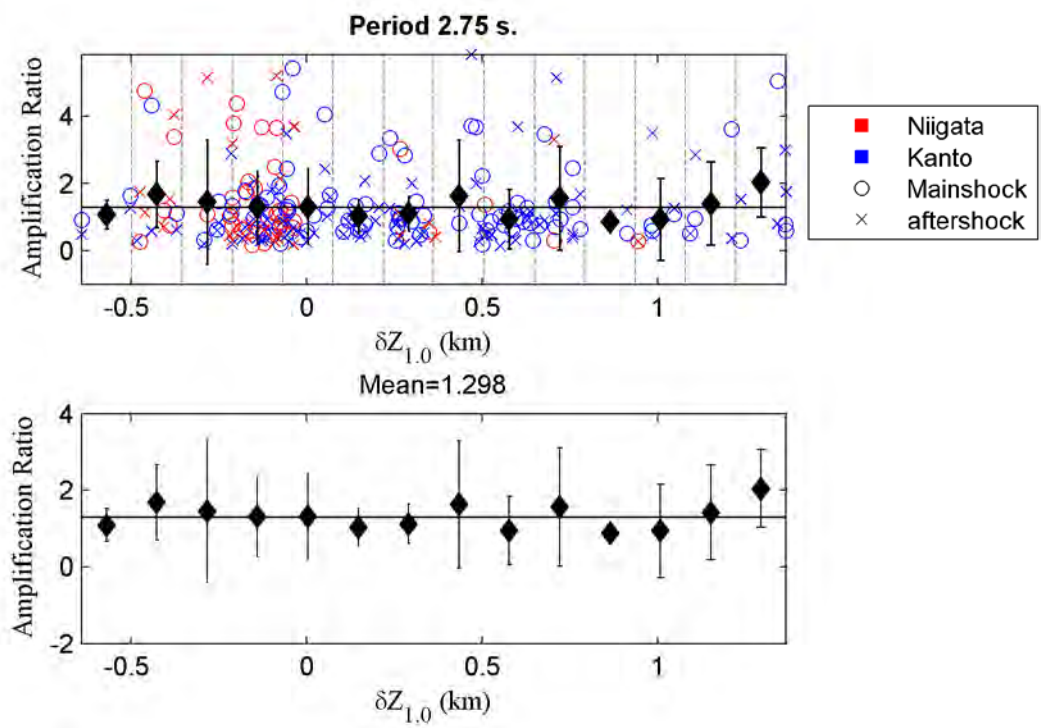


**Figure 29.** (Top) Amplification factor at 2.75 second is plotted as a function of depth differential. Data are divided into multiple bins where the average value at each bin is shown with diamonds. The black line corresponds to the average amplification factor. (Bottom) Average values at each bin (diamonds) and the average amplification factor (solid straight line) .

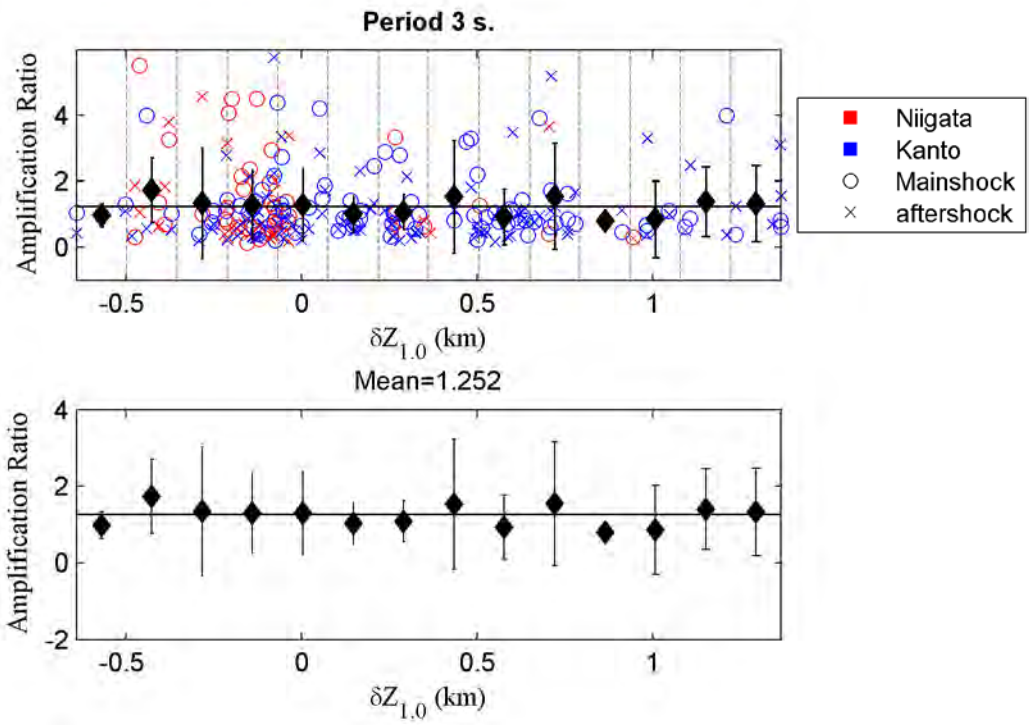


**Figure 29.** Continued, for 3.0 seconds.

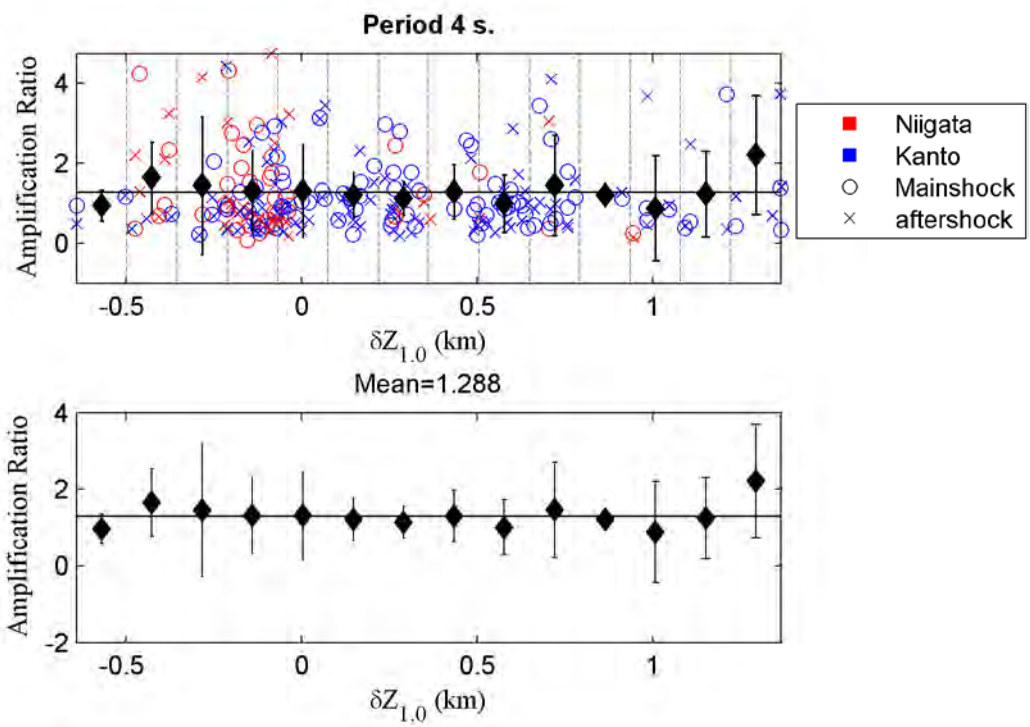


**Figure 29.** Continued, for 4.0 seconds.

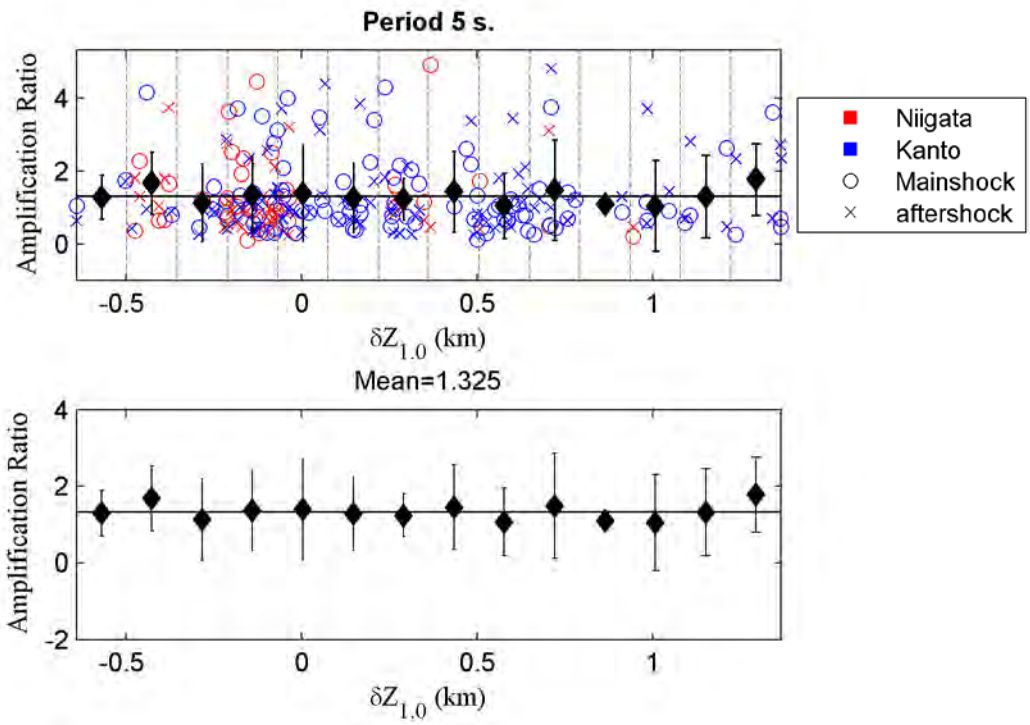


**Figure 29.** Continued, for 5.0 seconds.

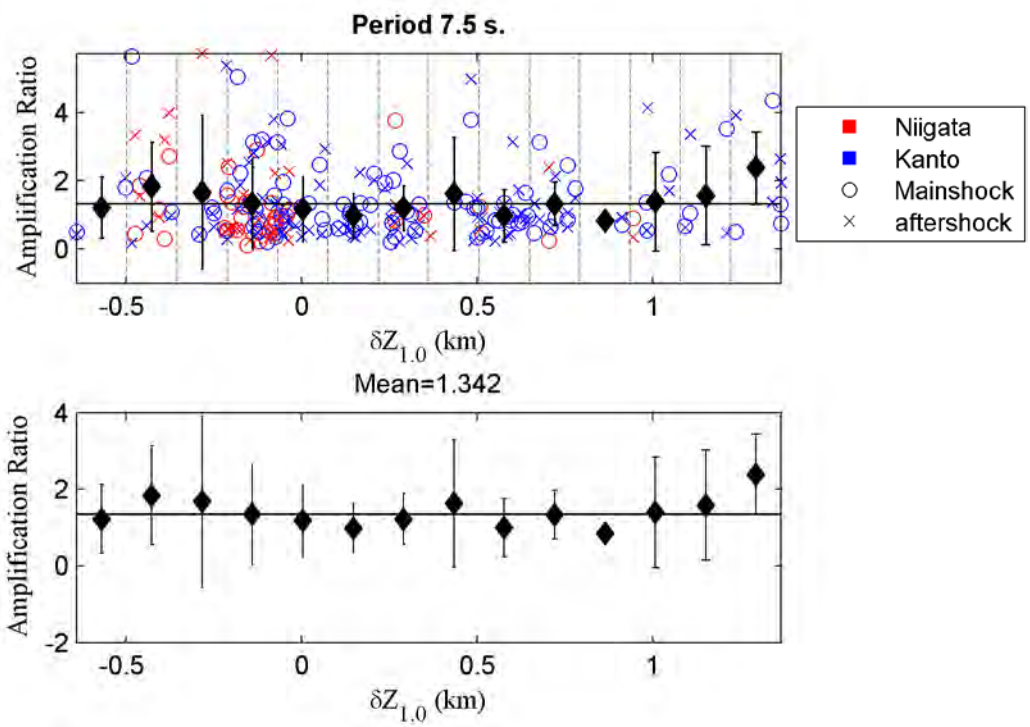


**Figure 29.** Continued, for 7.5 seconds.

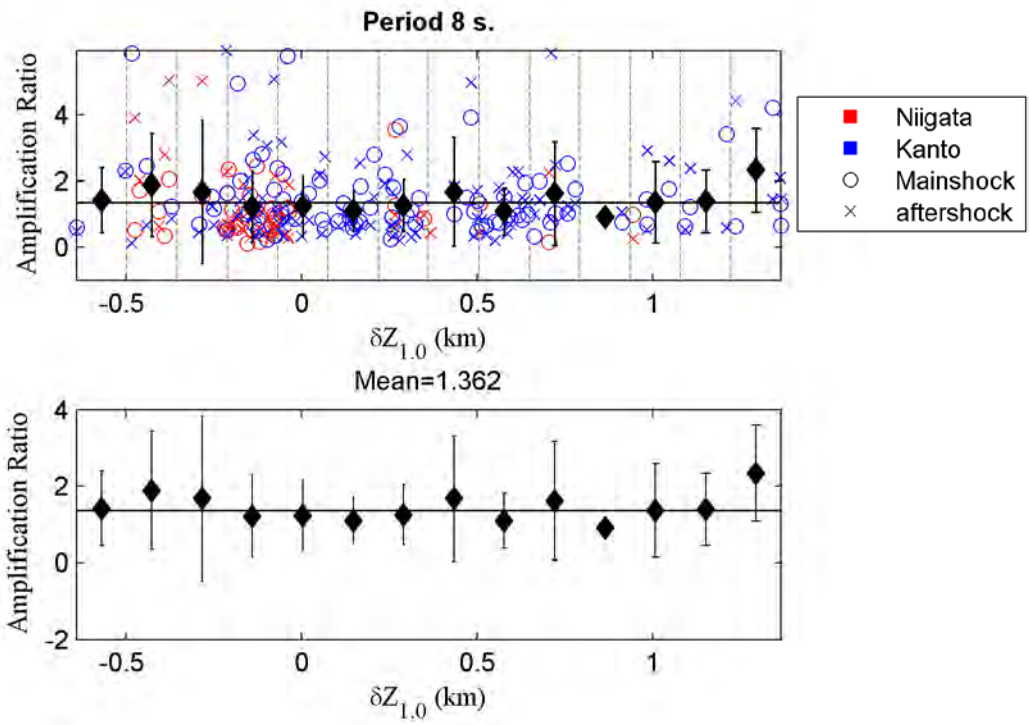


**Figure 29.** Continued, for 8.0 seconds.

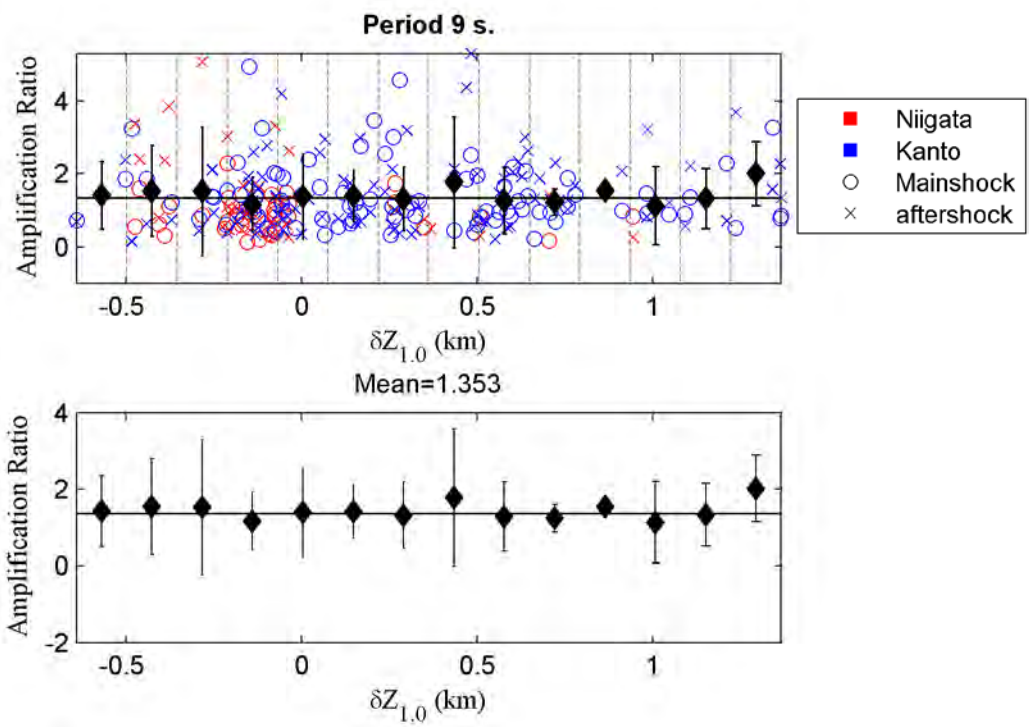


**Figure 29.** Continued, for 9.0 seconds.

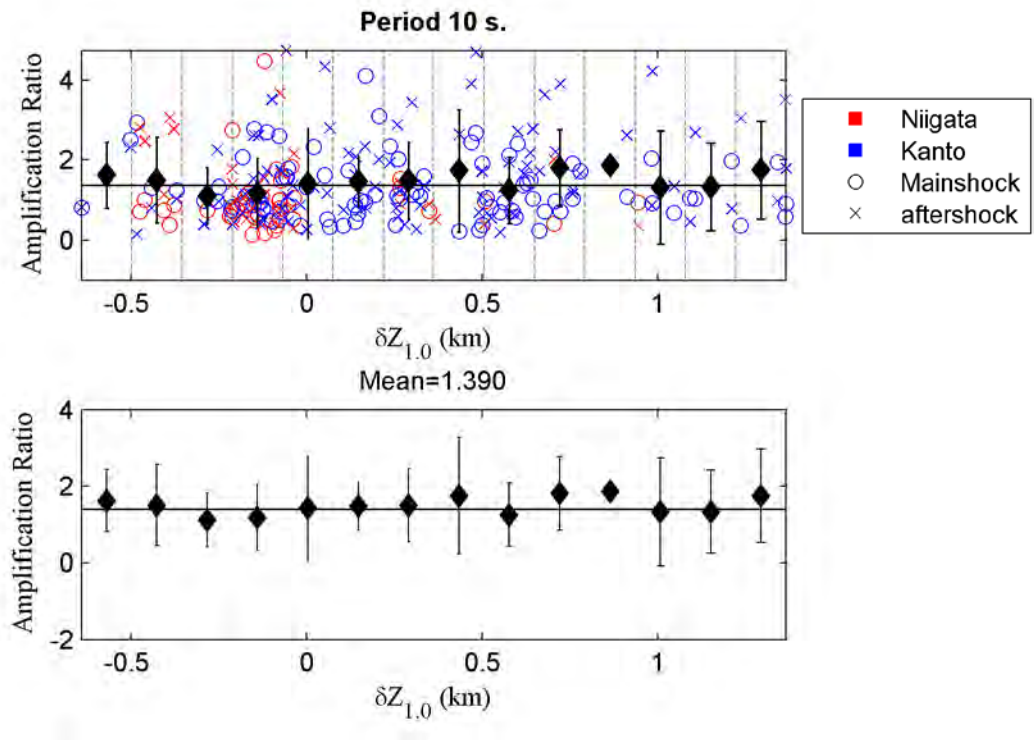


**Figure 29.** Continued, for 10.0 seconds.

**Table 6.** Mean values of the basin amplification from 3D simulations.

| Period (s) | Mean Amplification |
|---|---|
| **2.7** | 1.298 |
| **3** | 1.252 |
| **4** | 1.288 |
| **5** | 1.325 |
| **7.5** | 1.342 |
| **8** | 1.362 |
| **9** | 1.353 |
| **10** | 1.390 |

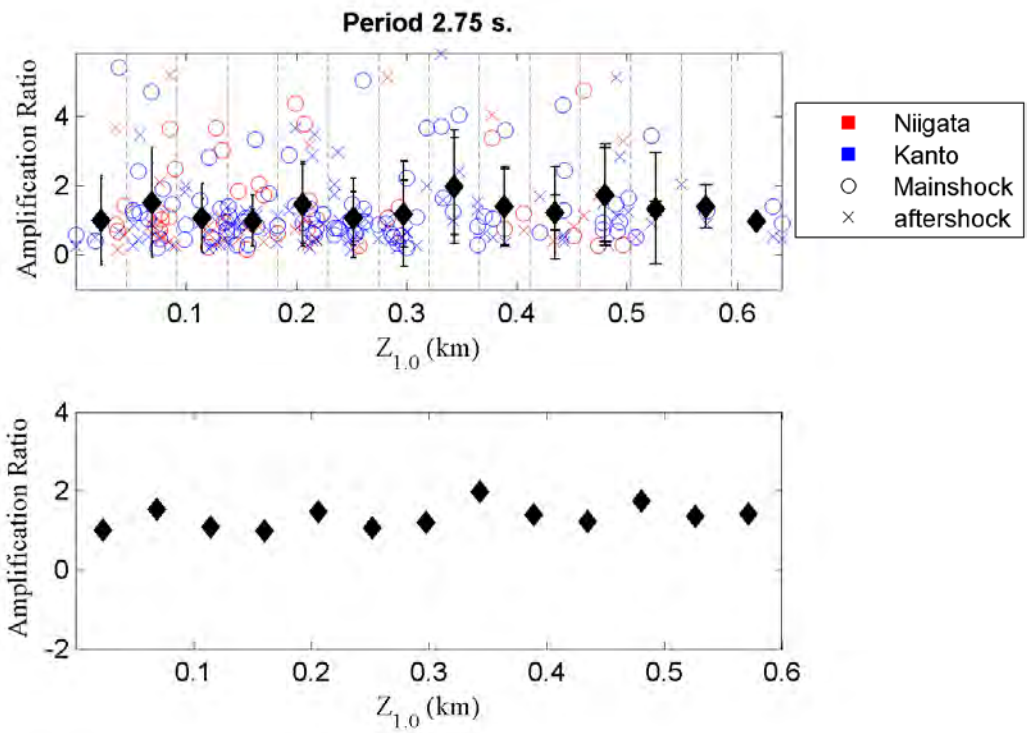


**Figure 30.** Amplification versus basin depth to S-wave velocity of 1.0 km/s for spectral period 2.75 second.

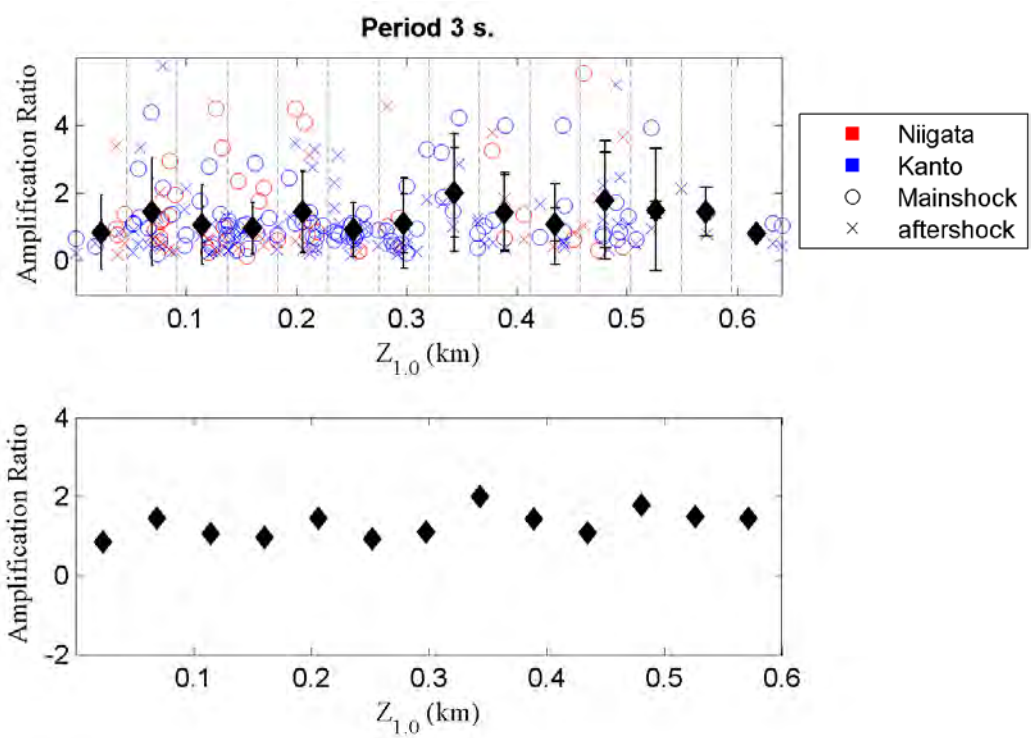


**Figure 30.** Continued, for spectral period 3.0 second.

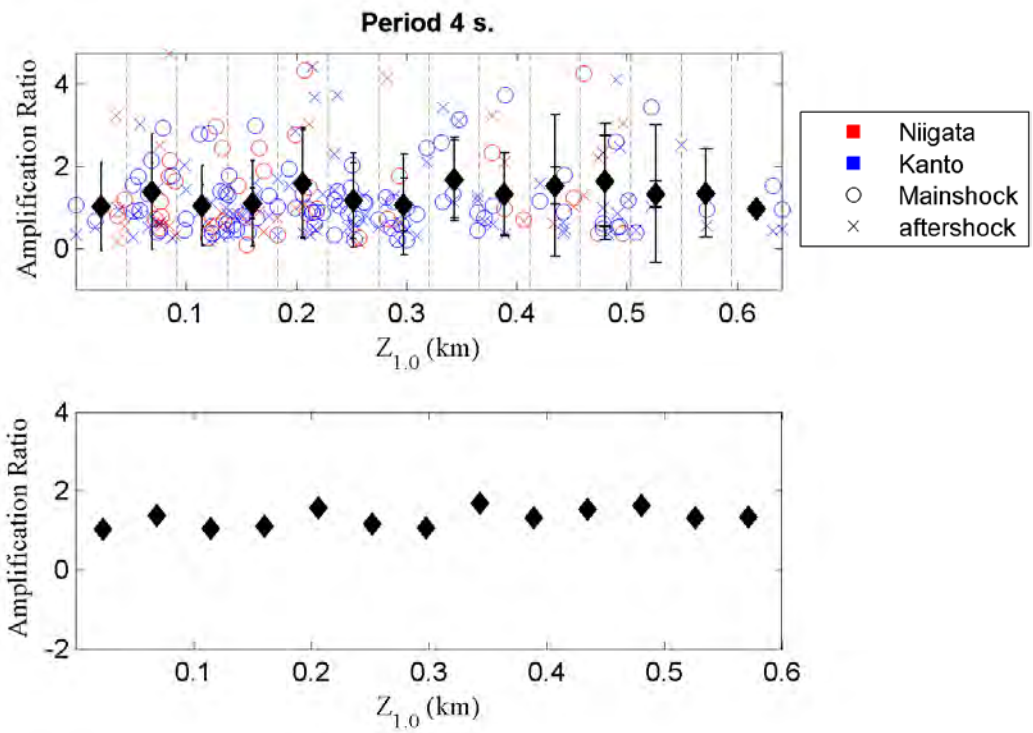


**Figure 30.** Continued, for spectral period 4.0 second.

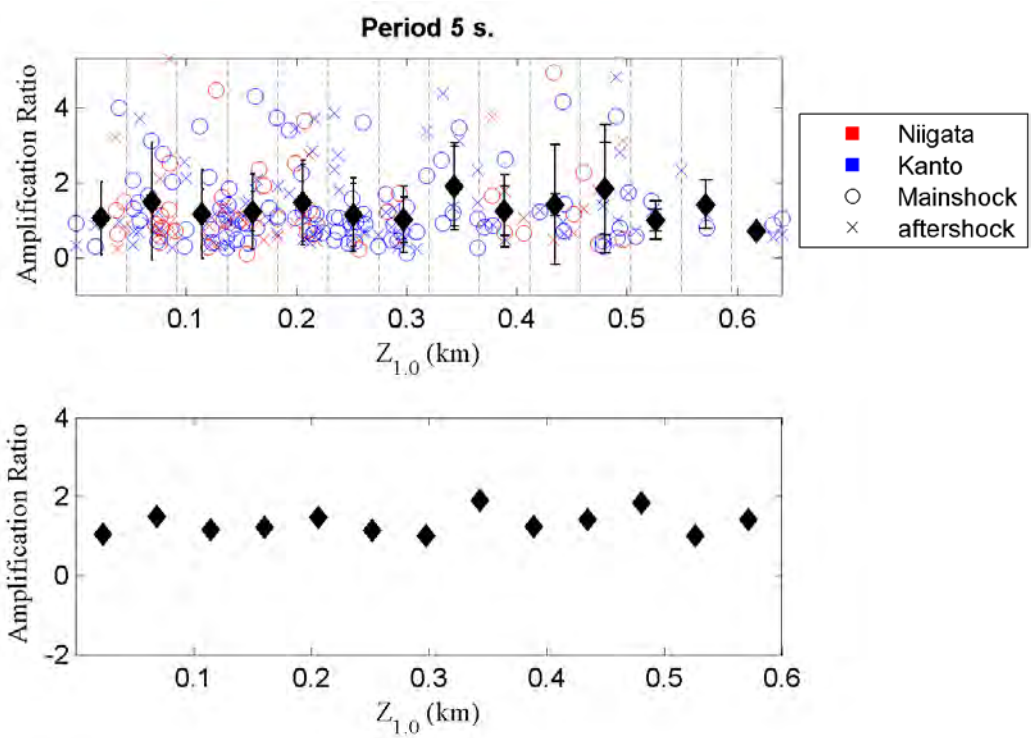


**Figure 30.** Continued, for spectral period 5.0 second.

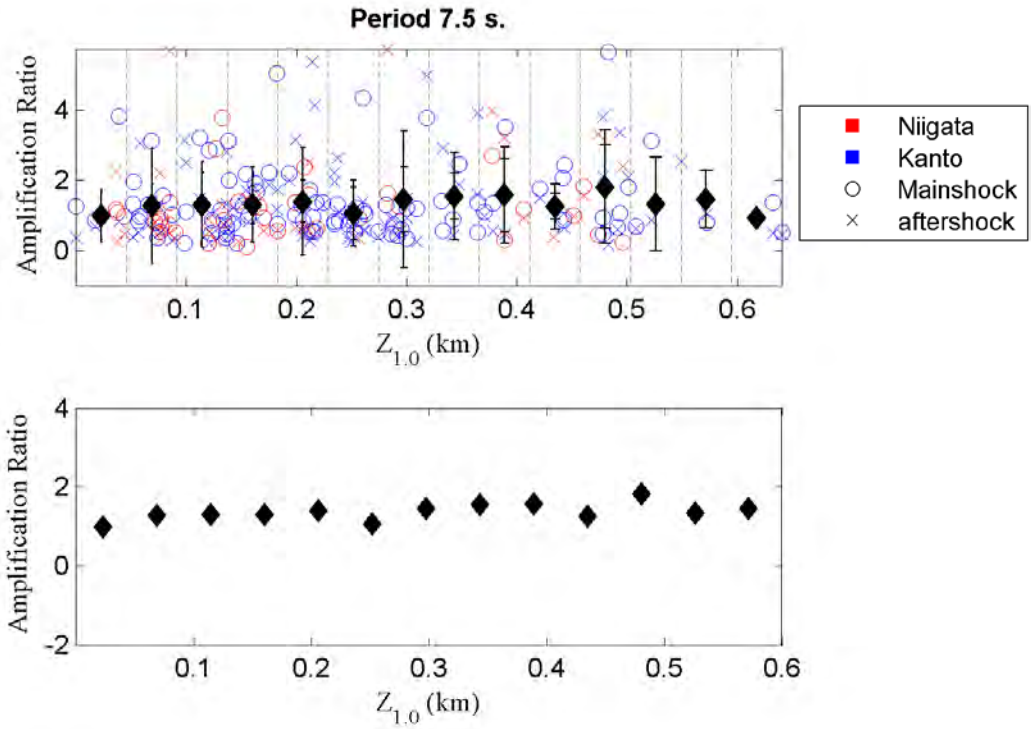


**Figure 30.** Continued, for spectral period 7.5 second.

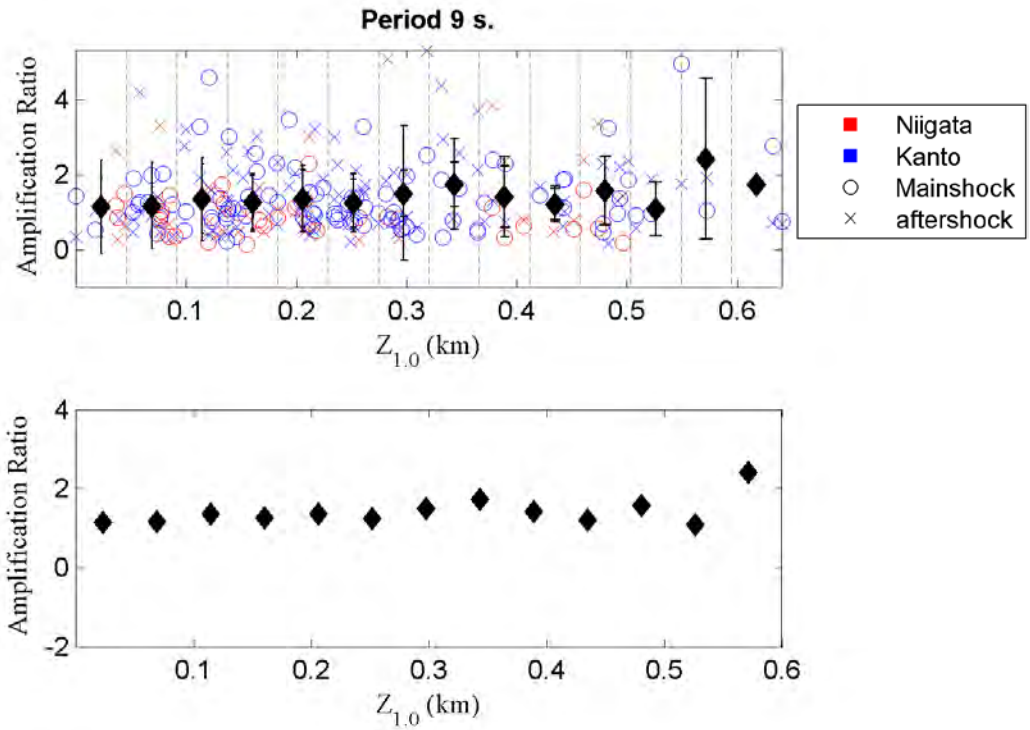


**Figure 30.** Continued, for spectral period 9.0 second.

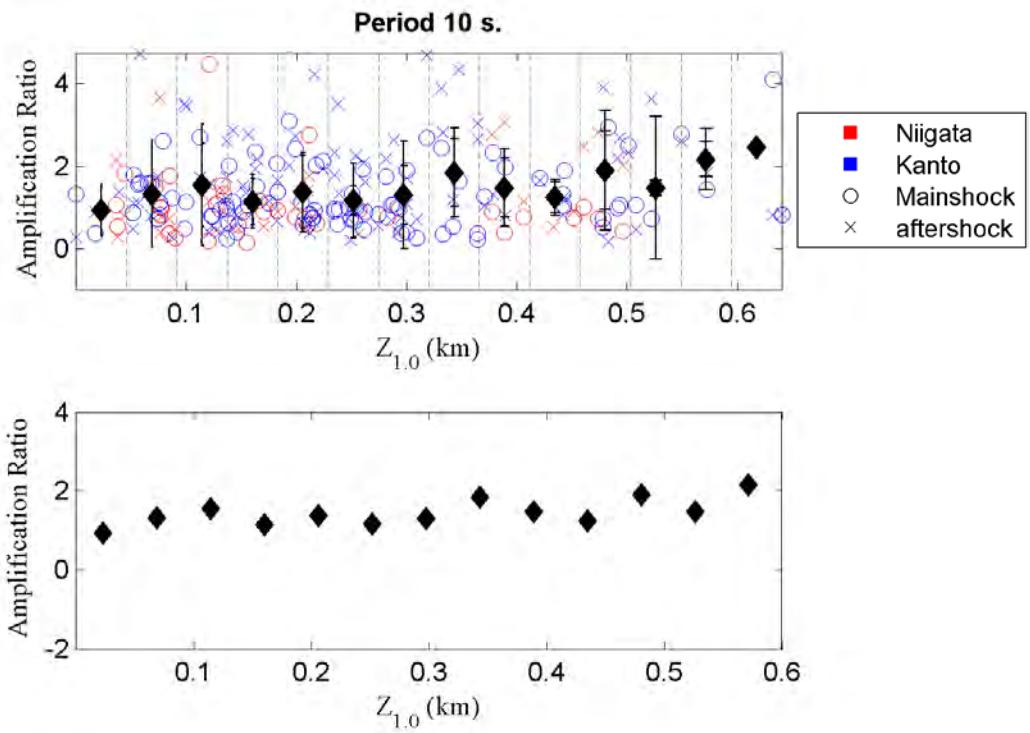


**Figure 30.** Continued, for spectral period 10.0 second.

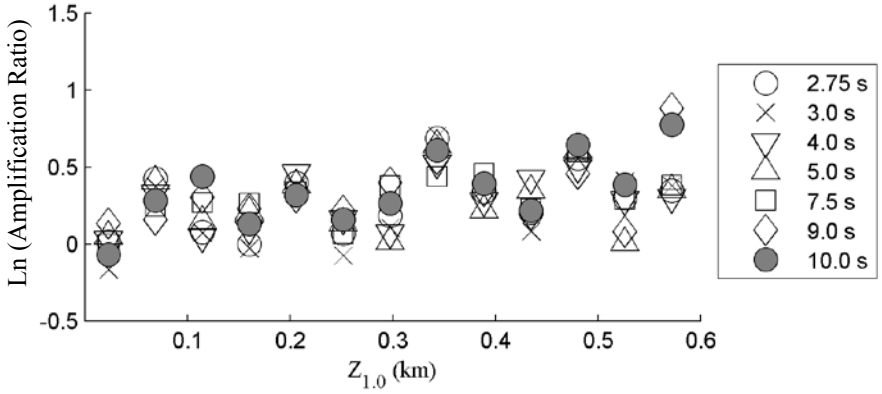


**Figure 31.** Natural logarithm of the amplification factor as a function of depth to the 1.0 km/s S-wave velocity. Symbols represent the mean amplification factor for various response spectral periods.

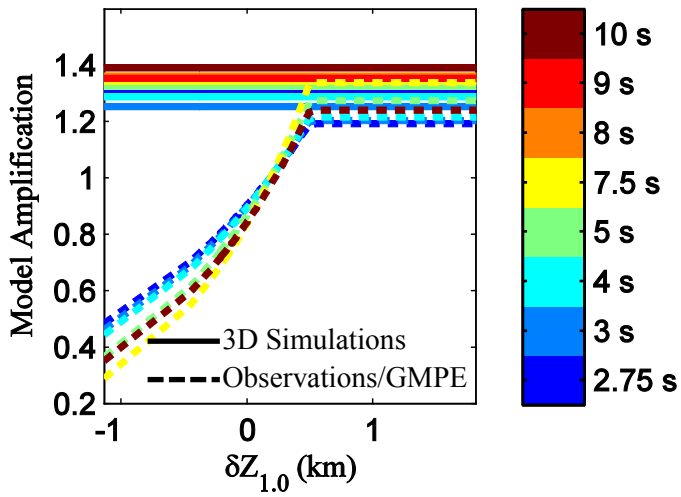


**Figure 32.** Amplification models obtained from 3D simulations as presented in Table 6 (solid lines) and from our empirical analysis for the Abrahamson et al. (2012) GMPE as presented in Table 4 (dashed lines).

## Application to the Seattle Basin

Maps of the Kanto, Niigata, and Seattle basins are provided in Figures 33 to 35, which have the same scale (2.5° x 2.5°) for ease of comparison. Figure 36 compares the sample 1D velocity models at the location of the red dot in Figures 33 to 35. The near-surface S-wave velocity profiles of the three basins are fairly similar down to 2 km depth, and the velocity profile of the Seattle basin is very close to that of the Niigata basin at depths of 2 to 4 km at the selected locations (Figure 36).

The amplification in the Seattle basin for two events was studied by Frankel and Stephenson (2015). The ratio of spectral response between basin recordings and a reference site with thin soil over firm rock is presented in Figure 37 for the Mw 6.8 Nisqually, and Mw 6.4 Vancouver Island earthquakes. It is observed from Figure 37 that the spectral amplification ratio in Cascadia can be as high as 4, comparable to the results from the finite difference simulations for the Kanto and Niigata basins performed in this study.

In addition, Frankel and Stephenson (2015) performed 3D finite difference simulations and calculated spectral response at basin, non-basin and rock sites for Mw 9 megathrust earthquakes on the Cascadia subduction zone. We used the response spectra from the Frankel and Stephenson (2015) simulations shown in Figure 38 to estimate the amplification factors which are presented in Figure 39. Maximum and mean amplifications estimated from observations and 3D simulations in this study of the Kanto and Niigata basins as presented in Table 4 are compared against seismic station QAW in the Seattle basin in Table 7 (Figure 40). The amplification at QAW is estimated from spectral accelerations acquired from 3D simulations by Frankel and Stephenson (2015). It is observed from Figure 40 t hat the amplifications obtained from

observations and 3D simulations in the Kanto and Niigata basins follow the trend of lower bound amplification for station QAW as estimated by Frankel and Stephenson (2015). The amplifications obtained from our Tohoku 3D simulations are similar to those obtained from the Tohoku data, and both are systematically lower than the lower bound amplification for station QAW for periods longer than 5 seconds.

## Conclusions

The amplifications that we obtained from observations and 3D simulations in the Kanto and Niigata basins follow the trend of the lower bound amplification for station QAW located in the Seattle basin as estimated by Frankel and Stephenson (2015). The fairly good agreement between our measured and simulation-based amplifications in the Kanto and Niigata basins demonstrates the viability of Frankel and Stephenson's (2015) use of simulation methods to estimate amplification in the Seattle Basin from large subduction earthquakes in the absence of recorded data. The measured amplifications in the Kanto and Niigata basins for periods up to 5 seconds are similar to the lower bound amplification for station QAW located in the Seattle basin as estimated by Frankel and Stephenson (2015), but are smaller at longer periods.

The adoption of amplification models from this study for application to the Seattle basin should be done with care considering the variation of amplification with respect to the direction from which seismic wave front approaches the Seattle basin (Frankel et al. 2007). In addition, Frankel et al. (2002) observed nonlinear behavior of soft-soil sites in the Seattle basin which should also be considered in the simulation but which lies outside the scope of this study.

**Figure 33.** (left) Aerial view of Kanto basin, (right) $z_{2.5}$ (in meters) for the Kanto basin.

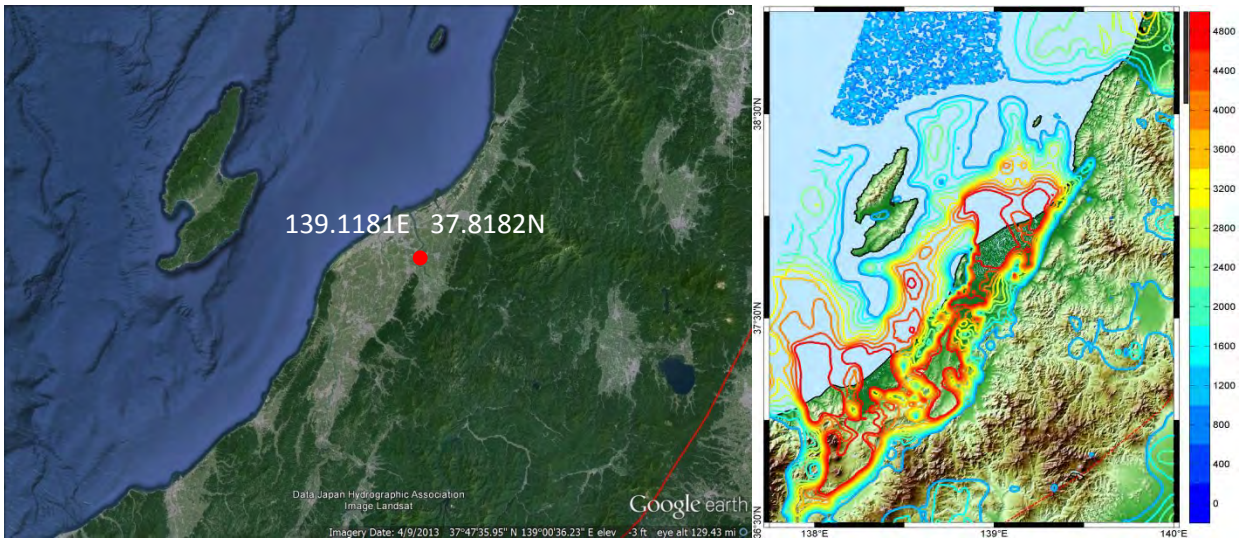


**Figure 34.** (left) Aerial view of Niigata basin, (right) $z_{2.5}$ (in meters) for the Niigata basin.

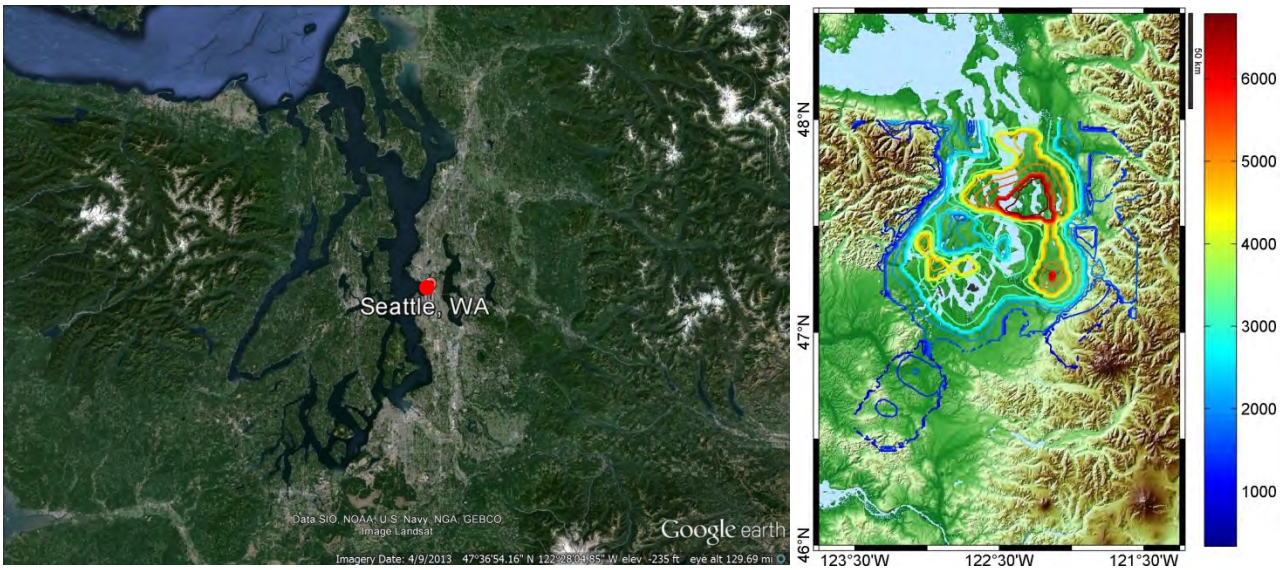


**Figure 35.** (left) Aerial view of Seattle basin, (right) $z_{2.5}$ (in meters) for the Seattle basin.

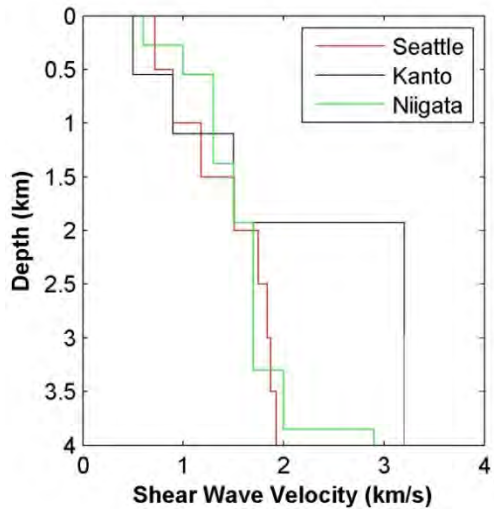


**Figure 36**. 1D velocity model for the Seattle, Kanto and Niigata basins. The velocity model of the Seattle basin is estimated at the approximate location of Seattle (located 17.5 km north, 40.0 east of the reference point in the 3D velocity model of Delorey and Vidale, 2010). The geographical locations of 1D velocity profiles are marked with red dots in Figures 33, 34, and 35.

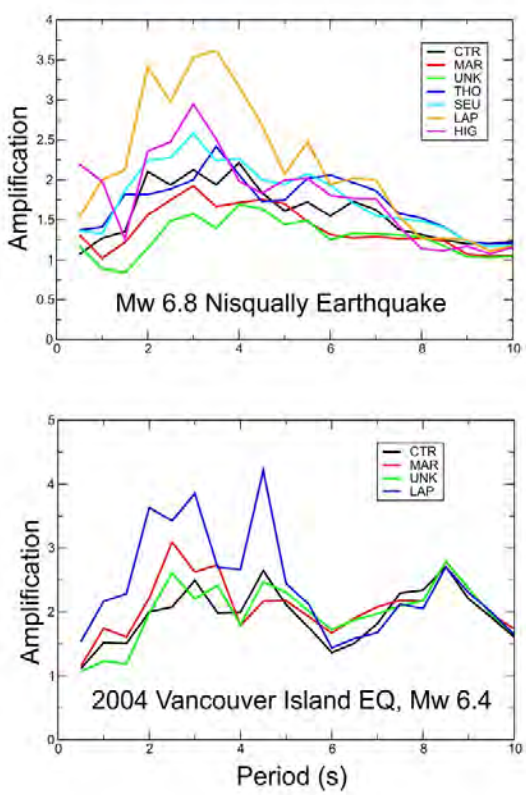


**Figure 37.** Observed spectral amplification in Seattle basin from two events (Source: Frankel and Stephenson, 2015).

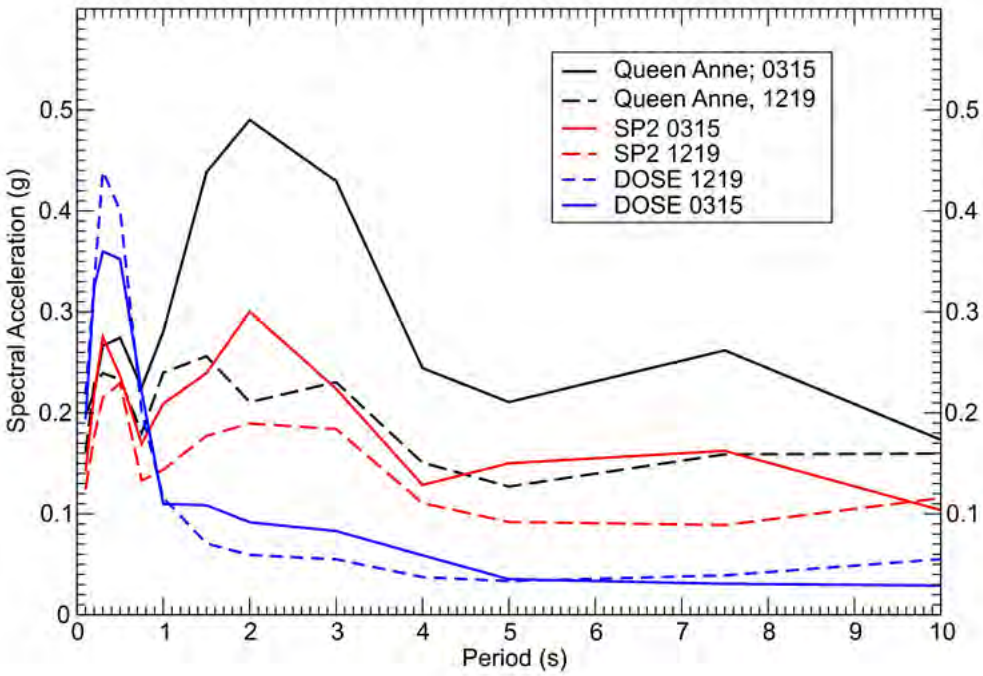


**Figure 38**. Spectral response from 3D simulations (Frankel and Stephenson, 2015) at stations representative of various local geology; QAW: site on Queen Anne Hill in Seattle basin, SP2: Seward Park site outside of Seattle basin, DOSE: rock site in eastern Olympics. Source: Frankel and Stephenson (2015).

**Table 7.** Sample amplification ranges calculated from Figure 38 from Frankel and Stephenson (2015).

| Period (s) | Amplification of basin site with respect to non-basin site | | Amplification of basin site with respect to rock site | |
|---|---|---|---|---|
| | Low | High | Low | High |
| 2 | 1.1 | 1.6 | 3.5 | 5.4 |
| 3 | 1.3 | 2.0 | 2.4 | 4.3 |
| 4 | 1.4 | 1.9 | 4.1 | 4.3 |
| 5 | 1.4 | 1.4 | 3.7 | 6.0 |
| 7.5 | 1.7 | 1.8 | 4.1 | 8.8 |
| 10 | 1.4 | 1.7 | 2.9 | 5.8 |

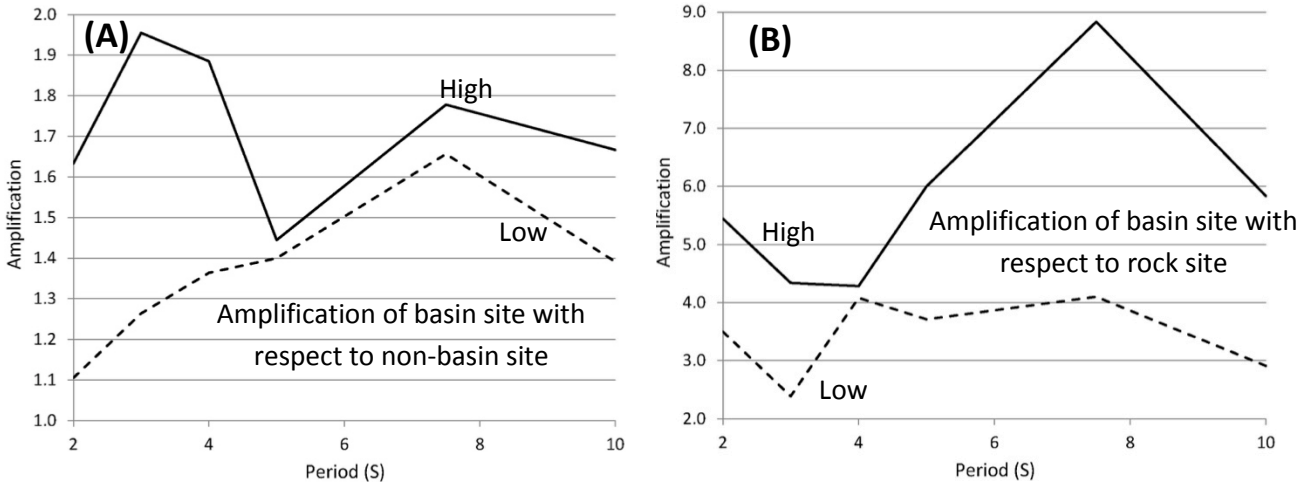


**Figure 39.** Amplification from 3D simulations for one station, and two events (produced from Frankel and Stephenson, 2015); amplification of basin site with respect to (A) non-basin site, (B) rock site.

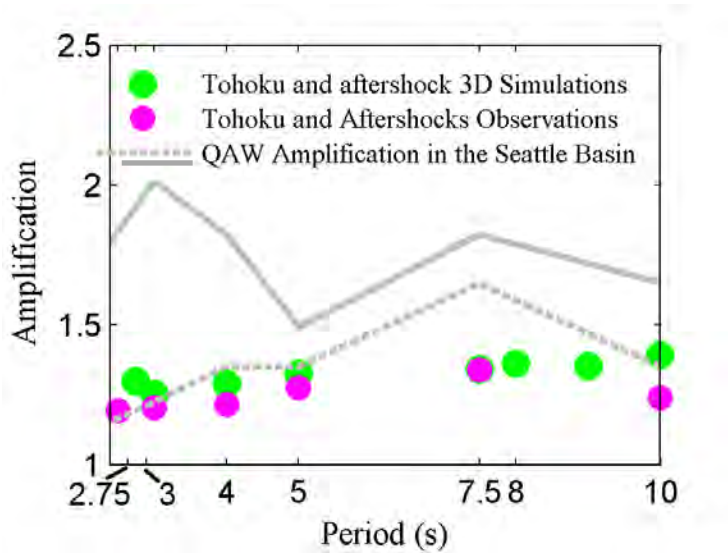


**Figure 40.** Average amplification factor from 3D Tohoku simulations (from Table 6, green circles) and maximum value (intercept) from the empirical analysis of Tohoku data using the Abrahamson et al. (2012) GMPE as reference (Table 4, magenta circles). Maximum and minimum boundaries of amplification for QAW station in the Seattle basin (grey lines) are reproduced from Frankel and Stephenson (2015).

## Data and Resources

Seismic data were downloaded from website of National Research Institute for Earth Science and Disaster Prevention (NEID) Strong-motion Seismograph Network (K-NET and KiK-net). Fault plane solutions for the selected events are from NEID Broadband Seismic Network (F-NET).

## Acknowledgments

We would like to thank Robert Graves for providing codes, information, and guidance in the finite difference simulation process. In addition we thank Arthur Frankel of the USGS for providing iso-surface data of the Seattle basin and research results. We also wish to thank C.B. Crouse for his comments, suggestions, and helpful criticisms that greatly improved the report.

## References

Abrahamson, N. A., and R. R. Youngs (1992). A stable algorithm for regression analyses using the random effects model, *Bull. Seismol. Soc. Am.* 82, 505–510.

Abrahamson, N., N. Gregor and K. Addo (2012). BC Hydro Ground Motion Prediction Equations for Subduction Earthquakes. *Earthquake Spectra, submitted*.

Ancheta, T. D., Darragh, R. B., Stewart, J. P., Seyhan, E., Silva, W. J., Chiou, B. S. J., Wooddell, K. E., Graves, R. W., Kottke, A. R., Boore, D. M., Kishida, T., Donohue, J. L. (2014), PEER NGA-West2 Database. *Earthquake Spectra*, EERI.

Boore, D. M. (2010). Orientation-independent, non geometric-mean measures of seismic intensity from two horizontal components of motion, *Bull. Seismol. Soc. Am.* 100, 1830–1835.

Boore, D. M., Stewart, J. P., Seyhan, E., and Atkinson, G. A. (2014). NGA-West2 equations for predicting PGA, PGV, and 5% damped PSA for shallow crustal earthquakes, *Earthquake Spectra* 30, 1057–1085.

Chiou, B. S.-J., and Youngs, R. R. (2014). Update of the Chiou and Youngs NGA model for the average horizontal component of peak ground motion and response spectra, *Earthquake Spectra* 30, 1117–1153.

Choi Y., J. P. Stewart, and R. W. Graves, (2005). Empirical Model for Basin Effects Accounts for Basin Depth and Source Location, *Bull. Seism. Soc. Am.* 95, 1412–1427.

Cox, B. R., R. W. Boulanger, K. Tokimatsu, C. M. Wood, A. Abe, S. Ashford, J. Donahue, K. Ishihara, R. Kayen, K. Katsumata, T. Kishida, T. Kokusho, H. B. Mason, R. Moss, J. P. Stewart, K. Tohyama, D. Zekkosl (2013). Liquefaction at Strong Motion Stations and in Urayasu City during the 2011 Tohoku-Oki Earthquake, *Earthquake Spectra* 29(S1), S55-S80.

Crouse, C.B., E.V. Leyendecker, P. Somerville, and M. Power (2006). Development of seismic ground-motion criteria for the ASCE 7 standard. *Proceedings of the 8th National Conference on Earthquake Engineering*, San Francisco, CA.

Day, S. M., Bielak, J., Dreger, D., Graves, R. W., Larsen, S., Olsen, K. B., and Pitarka, A., 2003. *Tests of 3-D Elastodynamic codes: Final report for Lifelines Project 1A02*, Pacific Earthquake Engineering Research Center.

Day, S.M., Graves, Robert, Bielek, Jacobo, Dreger, Douglas, Larsen, Shawn, Olsen, K.B., Pitarka, Arben, and Ramirez-Guzman, Leonardo (2008). Model for basin effects on long-period response spectra in southern California: *Earthquake Spectra* 24, 257–277.

Delorey, A. A., and J. E. Vidale (2010). Basin Shear-Wave Velocities beneath Seattle, Washington, from Noise-Correlation Rayleigh Waves, Bull. Seism. Soc. Am.101 (5), 2162-2175.

Delorey A.A., A.D. Frankel, P. Liu, and W. J. Stephenson (2014). Modeling the Effects of Source and Path Heterogeneity on Ground Motions of Great Earthquakes on the Cascadia Subduction Zone Using 3D Simulations, *Bull. Seism. Soc. Am.* 96, 1670- 1689.

Frankel, A. D., and W. J. Stephenson (2000). Three-dimensional simulations of ground motions in the Seattle region for earthquakes in the Seattle fault zone, Bull. Seismol. Soc. Am. 90, 1251–1267.

Frankel, D., D. L. Carver, R. A. Williams (2002). Nonlinear and Linear Site Response and Basin Effects in Seattle for the M 6.8 Nisqually, Washington, Earthquake, *Bull. Seism. Soc. Am.* 92(6), 2090-2109.

Frankel, A., W. J. Stephenson, D. L. Carver, R. A. Williams, J. K. Odum, and S. Rhea (2007). Seismic Hazard Maps for Seattle, Washington, Incorporating 3D Sedimentary Basin Effects, Nonlinear Site Response, and Rupture Directivity, *USGS Report*, Open-File Report 2007–1175.

Frankel, A., W. Stephenson and D. Carver (2009). Sedimentary Basin Effects in Seattle, Washington: Ground-Motion Observations and 3D Simulations. Bulletin of the Seismological Society of America, Vol. 99, No. 3, pp. 1579 –1611, June 2009, doi: 10.1785/0120080203.

Frankel, A. D., and W. J. Stephenson (2015). 3D Simulations of M9 Cascadia Earthquakes: Sedimentary-Basin Amplification and Ground-Motion Variability, *2015 SSA Annual Meeting*, Pasadena, California, USA, 21-23 April, 2015.

Ghofrani, H. and G. Atkinson (2013). Interface Ground-Motion Prediction Equations for Large Events based on Empirical Data from the 2011 M9.0 Tohoku and other Major Events. *Submitted to Bulletin of Earthquake Engineering*.

Graves, R. W. (1996). Simulating seismic wave propagation in 3D elastic media using staggered grid finite differences, *Bull. Seismol. Soc. Am.* 86, 1091–1106.

Graves, R. W., and S. M. Day (2003), Stability and accuracy of coarse-grain viscoelastic simulations, *Bull Seism. Soc. Am.* 93(1) 283-300.

Graves, R. A. Pitarka (2010). Broadband ground motion simulation using hybrid approach, *Bull. Seism. Soc. Am.,* 100, 2095-2123; DOI: 10.1785/0120100057

Graves, R., S. Wei and D. Helmberger (2012). Modeling Long Period (T > 4 sec) Strong Ground Motions for the 2011 M w 9 T ohoku-Oki Earthquake using an Enhanced Source Representation and 3D Seismic Velocity Models. *Annual Meeting of American Geophysical Union*.

Koketsu, K., H. Miyake, H. Fujiwara, and T. Hashimoto (2008), Progress towards a Japan integrated velocity structure model and long-period ground motion hazard map, paper S10-038 presented at *14th World Conference on Earthquake Engineering*, Beijing, China.

Somerville P., N. Collins, R. Graves and A. Pitarka (2004). An Engineering Ground Motion Model For Basin Generated Surface Waves, *13th World Conference On Earthquake Engineering Vancouver*, B.C., Canada, August 1-6, 2004, Paper No. 515.

Wei, S., R. Graves, D. Helmberger, J.-P. Avouac, and J. Jiang (2012). Sources of shaking and flooding during the Tohoku-Oki earthquake: a mixture of rupture styles. *Earth and Planetary Science Letters* 333-334 (2012), 91-100.

Wong, I. (2010). Geotechnical Characterization and Evaluation of Site Amplification at Selected PNSN Strong Motion Sites, Seattle, Washington, *U.S. Geological Survey*, USGS Report 03HQGR0012,

Zhao, J.X., J. Zhang, A. Asano, Y. Ohno, T. Oouchi, T. Takahashi, H. Ogawa, K. Irikura, H.K. Thio, P. Somerville, Y. Fukushima, and Y. Fukushima (2006). Attenuation Relations of Strong Motion in Japan using Site Classification based on Predominant Period. *Bull. Seism. Soc. Am.* 96, 898-913.